

AD-A266 625



(2)

MECHANISM OF INTERMITTENT ATOMIZATION  
FINAL REPORT

DTIC  
ELECTE  
JUL 09 1993  
S A D

S. P. Lin

June 1993

U.S. ARMY RESEARCH OFFICE

DAAL03-89-0179

CLARKSON UNIVERSITY

APPROVED FOR PUBLIC RELEASE

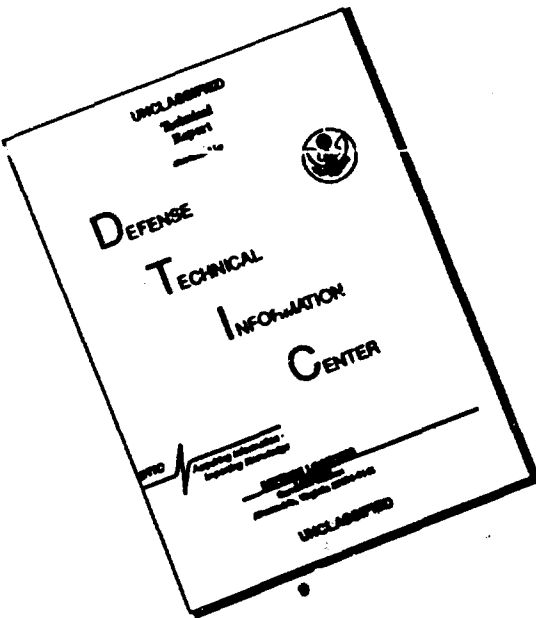
DISTRIBUTION UNLIMITED

83 7 08 14 9

93-15567



# DISCLAIMER NOTICE



THIS DOCUMENT IS BEST  
QUALITY AVAILABLE. THE COPY  
FURNISHED TO DTIC CONTAINED  
A SIGNIFICANT NUMBER OF  
PAGES WHICH DO NOT  
REPRODUCE LEGIBLY.

# REPORT DOCUMENTATION PAGE

Form Approved  
OMB No. 0704-0188

Public reporting burden for this collection of information is estimated to average 1 hour per response, including the time for reviewing instructions, searching existing data sources, gathering and maintaining the data needed, and completing and reviewing the collection of information. Send comments regarding this burden estimate or any other aspect of this collection of information, including suggestions for reducing this burden, to Washington Headquarters Services, Directorate for Information Operations and Reports, 1215 Jefferson Davis Highway, Suite 1204, Arlington, VA 22202-4302, and to the Office of Management and Budget, Paperwork Reduction Project (0704-0188), Washington, DC 20503.

1. AGENCY USE ONLY (Leave blank)			2. REPORT DATE June 15, 1993	3. REPORT TYPE AND DATES COVERED Final Report, 10/1/89 - 6/30/93
4. TITLE AND SUBTITLE  Mechanism of Intermittent Atomization			5. FUNDING NUMBERS  DAAL03-89-K-0179	
6. AUTHOR(S)  S.P. Lin				
7. PERFORMING ORGANIZATION NAME(S) AND ADDRESS(ES)  Clarkson University Potsdam, NY 13699			8. PERFORMING ORGANIZATION REPORT NUMBER  370350F	
9. SPONSORING/MONITORING AGENCY NAME(S) AND ADDRESS(ES)  U. S. Army Research Office P. O. Box 12211 Research Triangle Park, NC 27709-2211			10. SPONSORING/MONITORING AGENCY REPORT NUMBER  ARO 26797.10-EG	
11. SUPPLEMENTARY NOTES  The view, opinions and/or findings contained in this report are those of the author(s) and should not be construed as an official Department of the Army position, policy, or decision, unless so designated by other documentation.				
12a. DISTRIBUTION/AVAILABILITY STATEMENT  Approved for public release; distribution unlimited.			12b. DISTRIBUTION CODE	
13. ABSTRACT (Maximum 200 words)  A theory is developed for the purpose of enhancing the efficiency of internal combustion engines, and to reduce the air pollution caused by inefficient combustion. The theoretical results show that the droplet formation from the leading edge of the liquid fuel jet is caused by the Taylor-Lamb instability during the deceleration phase of the intermittent spray. The mechanism of droplet formation from the rest of the liquid-gas interface is caused by the interfacial stress fluctuation. The deceleration of the liquid jet tends to reduce the droplet diameter at the same pressure. However, finer sprays can be produced with a more sudden reduction in the nozzle inlet pressure after its peak during the injection period. An increase in the compressibility of the liquid jet is shown to promote the generation of smaller droplets, although at a slower rate. The compressibility of the ambient gas, as well as the surface tension, tends to promote absolute instability. The precise physical meaning remains unclear. The absolute instability can be reduced to convective instability by reducing the surface tension and/or increasing the compressibility of the jet fluid. The convective instability is responsible for the formation of sprays.				
14. SUBJECT TERMS  Intermittent fuel sprays, atomization			15. NUMBER OF PAGES 88	
			16. PRICE CODE	
17. SECURITY CLASSIFICATION OF REPORT  UNCLASSIFIED	18. SECURITY CLASSIFICATION OF THIS PAGE  UNCLASSIFIED	19. SECURITY CLASSIFICATION OF ABSTRACT  UNCLASSIFIED	20. LIMITATION OF ABSTRACT  UL	

## GENERAL INSTRUCTIONS FOR COMPLETING SF 298

The Report Documentation Page (RDP) is used in announcing and cataloging reports. It is important that this information be consistent with the rest of the report, particularly the cover and title page. Instructions for filling in each block of the form follow. It is important to stay within the lines to meet optical scanning requirements.

### Block 1. Agency Use Only (Leave blank).

**Block 2. Report Date.** Full publication date including day, month, and year, if available (e.g. 1 Jan 88). Must cite at least the year.

### Block 3. Type of Report and Dates Covered.

State whether report is interim, final, etc. If applicable, enter inclusive report dates (e.g. 10 Jun 87 - 30 Jun 88).

**Block 4. Title and Subtitle.** A title is taken from the part of the report that provides the most meaningful and complete information. When a report is prepared in more than one volume, repeat the primary title, add volume number, and include subtitle for the specific volume. On classified documents enter the title classification in parentheses.

**Block 5. Funding Numbers.** To include contract and grant numbers; may include program element number(s), project number(s), task number(s), and work unit number(s). Use the following labels:

C - Contract	PR - Project
G - Grant	TA - Task
PE - Program Element	WU - Work Unit
	Accession No.

**Block 6. Author(s).** Name(s) of person(s) responsible for writing the report, performing the research, or credited with the content of the report. If editor or compiler, this should follow the name(s).

**Block 7. Performing Organization Name(s) and Address(es).** Self-explanatory.

**Block 8. Performing Organization Report Number.** Enter the unique alphanumeric report number(s) assigned by the organization performing the report.

**Block 9. Sponsoring/Monitoring Agency Name(s) and Address(es).** Self-explanatory.

**Block 10. Sponsoring/Monitoring Agency Report Number.** (If known)

**Block 11. Supplementary Notes.** Enter information not included elsewhere such as: Prepared in cooperation with...; Trans. of...; To be published in.... When a report is revised, include a statement whether the new report supersedes or supplements the older report.

### Block 12a. Distribution/Availability Statement.

Denotes public availability or limitations. Cite any availability to the public. Enter additional limitations or special markings in all capitals (e.g. NOFORN, REL, ITAR).

DOD - See DoDD 5230.24, "Distribution Statements on Technical Documents."

DOE - See authorities.

NASA - See Handbook NHB 2200.2.

NTIS - Leave blank.

### Block 12b. Distribution Code.

DOD - Leave blank.

DOE - Enter DOE distribution categories from the Standard Distribution for Unclassified Scientific and Technical Reports.

NASA - Leave blank.

NTIS - Leave blank.

**Block 13. Abstract.** Include a brief (Maximum 200 words) factual summary of the most significant information contained in the report.

**Block 14. Subject Terms.** Keywords or phrases identifying major subjects in the report.

**Block 15. Number of Pages.** Enter the total number of pages.

**Block 16. Price Code.** Enter appropriate price code (NTIS only).

**Blocks 17. - 19. Security Classifications.** Self-explanatory. Enter U.S. Security Classification in accordance with U.S. Security Regulations (i.e., UNCLASSIFIED). If form contains classified information, stamp classification on the top and bottom of the page.

**Block 20. Limitation of Abstract.** This block must be completed to assign a limitation to the abstract. Enter either UL (unlimited) or SAR (same as report). An entry in this block is necessary if the abstract is to be limited. If blank, the abstract is assumed to be unlimited.

**MECHANISM OF INTERMITTENT ATOMIZATION  
FINAL REPORT**

**S. P. Lin**

**June 1993**

**U.S. ARMY RESEARCH OFFICE**

**DAAL03-89-0179**

**CLARKSON UNIVERSITY**

**APPROVED FOR PUBLIC RELEASE**

**DISTRIBUTION UNLIMITED**

<b>Accession For</b>	
NTIS	CRA&I <input checked="" type="checkbox"/>
DTIC	TAB <input type="checkbox"/>
U. Enclosed	<input type="checkbox"/>
Justification	
By	
Distribution	
Availability Copies	
Dist	Aveil. Date/Or Special
A-1	

**DTIC QUALITY INSPECTED 8**

## FOREWORD

The project 26797-EG "Mechanism of Intermittent Atomization" was under the directorship of Dr. David Mann of the Engineering and Environmental Sciences Division of the Army Research Office. The period of this project is from 1 October 1989 to 30 June 1993. The grant number of this project is DAAL03-89-K-0179. During the project period, the writer also received an instrumentation grant from the Department of Defense-University Research Instrumentation Program for FY91.

## TABLE OF CONTENTS

	Page
1. Problem Statement . . . . .	1
2. Summary of Research Results . . . . .	1
3. List of Publications . . . . .	3
4. Participating Personnel . . . . .	3
5. Bibliography . . . . .	3
6. Appendices . . . . .	4
A. Weakly nonlinear instability of a liquid jet in a viscous gas	
B. Effects of compressibility on the atomization of liquid jets	
C. Absolute and convective instability of a compressible jet	
D. Absolute and convective instability of a viscous liquid jet surrounded by a viscous gas in a vertical pipe	
E. Experimental study of an intermittent spray	
F. Mechanism of intermittent atomization	

## **1. Problem Statement**

The fundamental mechanism of the formation of intermittent sprays, which are encountered for example in diesel engines, is analyzed theoretically. The effects of the variation of the pressure wave form, which causes the intermittency, on the characteristics of sprays is investigated. The compressibility of the ambient gas as well as that of the jet liquid are taken into account. The speed of the jet ranges from subsonic to supersonic.

## **2. Summary of Research Results**

It is shown that the droplet formation from the leading edge of the liquid fuel jet is caused by the Taylor-Lamb instability associated with the apparent body force during the deceleration phase of the intermittent spray. The mechanism of droplet formation from the rest of the liquid-gas interface remains the same as that for the case of stationary atomization, i.e. the interfacial stress fluctuation. It is found that finer sprays can be produced with a more sudden reduction in the nozzle inlet pressure after its peak during the injection period. An increase in the compressibility of the liquid jet is shown to promote the generation of smaller droplets, although at a slower rate. The compressibility of the ambient fluid, as well as the surface tension are shown to promote absolute instability. The absolute instability can be reduced to the convective instability by increasing the compressibility of the jet liquid. The convective instability is the manifestation of spatially growing disturbances. The physical significance of the theoretically predicted absolute instability remains poorly understood. An effort by the present P.I. to understand this significance is currently supported by a NASA grant. The viscosity of the ambient gas is demonstrated to increase the droplet diameter in a spray. These results are

published in journal papers given in Appendices A-D. Appendix E "Experimental Study of an Intermittent Spray Using Several Nozzle Pressure Waveforms" is excerpted from the M.S. thesis of Vincent F. Cook. He is expected to write up his thesis for journal publication in the near future. The theoretical counter part of his thesis, the excerpt of which is given in Appendix F, is being prepared for publication.

### **3. List of Publications**

Four journal publications have resulted from this research project.

- a. Ibrahim, E.I. and Lin, S.P., "Weakly nonlinear instability of a liquid jet in a viscous gas," *J. Appl. Mech.* **59**, 291-296, 1992.
- b. Zhou, Z.W. and Lin, S.P., "Effects of compressibility on the atomization of liquid jets," *AIAA J. of Propulsion and Power*, **8**, 736-740, 1992.
- c. Zhou, Z.W. and Lin, S.P., "Absolute and convective instability of a compressible jet," *Physics of Fluids A*, **4**, 277-282, 1993.
- d. Lin, S.P. and Lian, Z.W., "Absolute and instability of a viscous liquid jet surrounded by a viscous gas in a vertical pipe," *Physics of Fluids A*, **5**, 771-773, 1993.

### **4. Participating Personnel**

The following individuals have participated in the undertaking of this project.

- a. Dr. S.P. Lin, Professor, Principal Investigator
- b. Mr. R.D. Webb, Graduate Research Assistant. Completed M.S. degree, November 1992. Thesis title: "Stability of a viscous jet".
- c. Mr. V.F. Cook, Graduate Research Assistant. Completed M.S. degree, 18 January 1993. Thesis title: "Experimental study of an intermittent spray using several nozzle pressure waveforms".
- d. Mr. D. Woods, Graduate Research Assistant, Ph.D. Candidate.
- e. Dr. Z.W. Zhou, Research Associate.

### **5. Bibliographies**

Relevant bibliographies are cited in the references sections of the articles included in the appendices.

## **6. Appendices**

## (APPENDIX A)

**E. A. Ibrahim**

Mechanical Engineering Department,  
Tuskegee University,  
Tuskegee, AL  
Mem. ASME

**S. P. Lin**

Department of Mechanical and  
Aeronautical Engineering,  
Clarkson University,  
Potsdam, NY  
Mem. ASME

# Weakly Nonlinear Instability of a Liquid Jet in a Viscous Gas

*The weakly nonlinear instability of a viscous liquid jet emanated into a viscous gas contained in a coaxial vertical circular pipe is investigated as an initial-value problem. The linear stability theory predicted that the jet may become unstable either due to capillary pinching or due to interfacial stress fluctuation. The results of nonlinear stability analysis shows no tendency of supercritical stability for both of the linearly unstable modes. In fact, the nonlinear growth rate of the disturbance is faster than the exponential growth rate of the linear normal mode disturbance for the same flow parameters. Moreover, the most amplified linear normal mode disturbance evolves nonlinearly into a nonsinusoidal wave of shorter wavelength. No nonlinear instability is found for the linearly stable disturbances. Thus, while the linear theory is adequate for the prediction of the onset of jet breakup, nonlinear theory is required to describe the outcome of the jet breakup.*

### Introduction

A computational investigation of the stability of cylindrical jets is undertaken as an attempt to understand the atomization phenomena of liquid jets. These phenomena occur in many applications such as the liquid fuel injection in internal combustion engines, spray coatings of surfaces, forming submicron solid particles, and in various printing devices.

For many purposes, the linear theory adequately describes the salient features of the jet instability; for example, it accurately predicts the small amplitude growth rate of a sinusoidal disturbance. However, it is a common observation that the wave form of an initially sinusoidal perturbation becomes nonsinusoidal close to the point of drop formation, i.e., the point at which the surface wave amplitude equals the radius of the jet (in capillary instability). In order to explain this phenomena, much work has been done on the nonlinear capillary instability of liquid jets. Wang (1968) investigated the effect of a finite amplitude on a circular column of inviscid liquid with a third-order perturbation approach but points out that this solution is not uniformly valid for all wave numbers. Yuen (1968) also used the perturbation approach to third order, but his choice for the third-order term gives rise to a secular term whose elimination leads to a small amplitude-dependent shift in the cutoff wave number. Yuen (1968) concluded that the asymmetrical development of an initially sinusoidal wave is a nonlinear effect with generation of higher harmonics as well as feedback into the fundamental. Nayfeh (1970) pointed

out that Yuen's analysis is valid to second order, but that his third-order term is incorrect for wave numbers close to the cutoff wave number. A comparison between an experimental wave profile and one calculated using Yuen's formulation was made by Rutland and Jameson (1970); however, it was for relatively large displacements and showed only qualitative agreement. Lafrance (1975) used a drop spectrometer to measure the size of the main and satellite drops as a function of the perturbation frequency. He compared these to sizes calculated from a modified version of Yuen's analysis and found good agreement which is surprising since, in principle, the theory is invalid in the region where drops are being formed. Chaudhary (1977) indicated that Lafrance's analysis couldn't satisfy its own initial conditions, and Lafrance's multiple-time scale failed in the third-order problem. Consequently, Chaudhary and Redekopp (1980a) and Chaudhary and Maxworthy (1980b) used a comparable model and performed experiments on the jet behaviors and satellite drop formation. With a third-order component in the disturbance, Chaudhary et al. (1977, 1980a, 1980b) were able to control experimentally the satellite behaviors, but his theory didn't agree with his experiment. Lee (1974) derived a pair of nonlinear one-dimensional equations for the jet radius and its axial velocity. He further solved his one-dimensional equations numerically for the infinite jet problem and obtained main drops and satellite drops. Bogy (1978a, 1978b, 1979) expanded the Cosserat theory of Green (1976) to develop a new analytical model for higher harmonics based on spatial and temporal instability. The theory is capable of describing the satellite drop behavior. The numerical investigation of Shokoohi and Elrod (1987) by using the vorticity-stream function method shows that the nonlinear terms are responsible for the nonuniformity of the size of drops produced in jet disintegration. The computations were limited to a low Reynolds number by numerical stability considerations and a computational time requirement. Phinney (1972) carried out experiments that lead him to support the conjecture that the

Contributed by the Applied Mechanics Division of THE AMERICAN SOCIETY OF MECHANICAL ENGINEERS for presentation at the Winter Annual Meeting, Atlanta, Ga., Dec. 1-6, 1991.

Discussion on this paper should be addressed to the Technical Editor, Prof. Leon M. Keer, The Technological Institute, Northwestern University, Evanston, IL 60208, and will be accepted until two months after final publication of the paper itself in the JOURNAL OF APPLIED MECHANICS. Manuscript received by the ASME Applied Mechanics Division, July 26, 1990; final revision, Mar. 15, 1991. Paper No. 91-W-A/AM-15.

theory and understanding that were developed in connection with the breakup of laminar jets can be used as a guide for turbulent jets as well.

The nonlinear studies cited in the previous paragraph are relevant to the ink jet breakup. By use of linear theory of convective instability Lin and Lian (1990) showed that there are two physically distinctive modes of jet breakup. The first is the Rayleigh mode which produces drops of diameters comparable with the jet diameter. The second is the Taylor mode which atomizes the jet into droplets of diameters much smaller than the jet diameter. Lin and Creighton (1990) showed that the former mode is caused by capillary pinching, but the latter mode is caused by the interfacial pressure fluctuation.

To the best knowledge of the present authors, this investigation is the first nonlinear analysis of the jet breakup in the atomization regime taking into account the viscosities of the liquid jet and the ambient gas as well as the gravitational force.

## Analysis

We shall resort to the application of the nonlinear theory of hydrodynamic stability in which disturbances are superimposed upon a stationary flow field. These disturbances are time dependent, and it is the aim of the theory to look for disturbances whose amplitude increases, decreases, or does not vary with time. Disturbances of the first type we shall call unstable, whereas those of the second or third type will be called stable. We shall focus our attention on disturbances of wave form that repeats itself every wavelength. Such an analysis is called a temporal stability analysis, as opposed to a spatial stability analysis where wave forms repeat themselves periodically in time. Temporal stability analysis is adequate for an infinitely long jet compared to the jet radius, while a spatial stability analysis is adequate for a finite jet. Keller et al. (1973) have shown, in a linear analysis, that the growth rate for these two cases coincide when the jet velocity is much greater than the characteristic velocity  $\sigma/(\rho_1 R)$ . The approach we follow is similar to that of Lin and Ibrahim (1990).

Consider the circular liquid jet of radius  $R$  that is issued into a viscous gas bounded by a cylindrical wall at a distance  $S$  from the jet axis as shown in Fig. 1. Both the liquid and gas are assumed to be incompressible and Newtonian. The onset of ligament formation and its subsequent breakup into droplets are governed by the continuity and Navier-Stokes equations of the two-dimensional disturbed flow which can be written in dimensionless form as

$$(U + u)_{,r} + (U + u)_{,z} + (W + w) = 0 \quad (i=1,2) \quad (1)$$

$$\begin{aligned} (U + u)_{,r} + (U + u)_{,z} + (W + w)_{,r} + (W + w)_{,z} \\ = -(\rho_1/\rho_2)(P + p)_{,r} + \nu_1/(\nu_1 \text{Re})[(U + u)_{,rr} \\ + (U + u)_{,zz} + (U + u)_{,rz} - (U + u)_{,rr}^2] \quad (2) \\ (W + w)_{,r} + (U + u)_{,z} + (W + w)_{,z} + (W + w)_{,rr} \\ = -(\rho_1/\rho_2)(P + p)_{,z} - Fr^{-1} + (\nu_1/\nu_2 \text{Re})[(W + w)_{,rr} \\ + (W + w)_{,zz} + (W + w)_{,rz}] \quad (3) \end{aligned}$$

where  $U$  and  $W$  are, respectively, the radial and axial velocities of the undisturbed flow,  $u$  and  $w$  are, respectively, the radial and axial velocities of the disturbance, and  $P$  and  $p$  are, respectively, the undisturbed flow and the disturbance pressures. Subscript 1 is for liquid and 2 is for gas. Subscripts  $t$ ,  $r$ , and  $z$  stand for partial differentiations with respect to time, radial distance, and axial distance, respectively.  $\text{Re}$  is the Reynolds number based on the liquid properties,  $\text{Re} = W_0 R / \nu_1$ , where  $W_0$  is the axial velocity along the jet axis,  $R$  is the jet radius, and  $\nu_1$  is the liquid kinematic viscosity.  $Fr$  is the Froude number,  $Fr = W_0^2 / (gR)$ , where  $g$  is the gravitational acceleration. All lengths are made nondimensional by the jet radius  $R$ . Velocities are made dimensionless by dividing by  $W_0$ . Time is

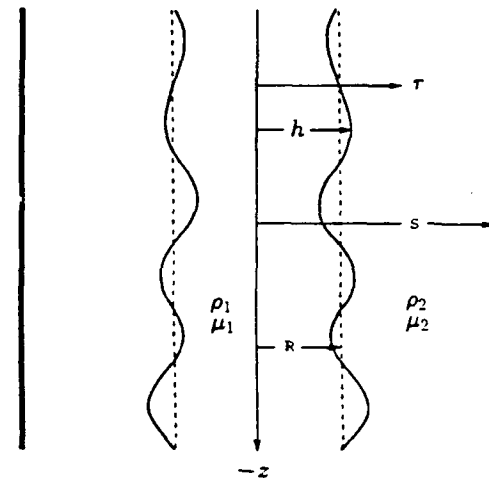


Fig. 1 Definition sketch

made dimensionless by  $R/W_0$ . The pressure is made dimensionless by dividing by  $\rho_1 W_0^2$ , where  $\rho_1$  is the liquid density.

The continuity and Navier-Stokes equations of the undisturbed (basic) flow are given by

$$W_{,z} = 0 \quad (4)$$

$$U_{,r} = 0, \quad P_{,r} = 0 \quad (5)$$

$$0 = -(\rho_1/\rho_2)P_{,z} - Fr^{-1} + \nu_1/(\nu_1 \text{Re})(W_{,rr} + W_{,zz}/r). \quad (6)$$

Note that  $W_{,r} = 0$  because the basic flow is steady.  $W_{,z}$  and  $W_{,rr}$  both vanish by virtue of the continuity equation which also leads to the conclusion that  $W$  is a function of radial distance alone.

Substitution from the governing equations of the basic flow into the equations, which govern the disturbed flow, and eliminating the pressure by cross differentiation yield;

$$\begin{aligned} \{\partial_r - \nu_1/(\nu_1 \text{Re})E^2\}E^2\psi_{,z} + W_{,z}E^2\psi_{,r} - \nu_1\psi_{,z}(W_{,r}/r), \\ = r[\psi_{,r}r^{-2}E^2\psi_{,z} - \psi_{,z}(r^{-2}E^2\psi_{,r})] \quad (7) \end{aligned}$$

where  $\psi$  is the dimensionless disturbance stream function defined as,

$$u_i = \psi_{,r}/r, \quad w_i = -\psi_{,z}/r \quad \text{and} \quad E^2 = \partial_{rr} - (1/r)\partial_r + \partial_{zz}.$$

The solution of the basic state equations subject to the boundary conditions,

$$W_1(0) = -1 \quad (\text{finite velocity along the jet axis})$$

$$W_1(3) = 0 \quad (\text{no-slip velocity at the wall})$$

$$W_1(1) = W_2(1) \quad (\text{velocity continuity at the interface})$$

$$W_1(1) = NW_2(1) \quad (\text{tangential force balance at the interface})$$

$$(P_1 - P_2) = We \quad (\text{normal force balance at the interface})$$

is given by Ibrahim (1989) as

$$\begin{aligned} W_1 = -1 + N\beta^2/[N - (1 - \beta^2)] \{1 - [(1 - Q)/(4N)] \\ \times (\text{Re}/Fr)[2 \ln \beta + (1 - \beta^2)]\} \quad (8) \end{aligned}$$

$$\begin{aligned} W_2 = -(\beta^2 - \beta^4)/[N - (1 - \beta^2)] \{1 \\ - [(1 - Q)/(4N)](\text{Re}/Fr)[2 \ln \beta + (1 - \beta^2)]\} \\ + [(1 - Q)/(4N)](\text{Re}/Fr)[\beta^2 - \beta^4 - 2 \ln (\beta/r)] \quad (9) \end{aligned}$$

where  $\beta$  is the aspect ratio,  $\beta = S/R$ , with  $S$  being the distance from the jet axis to the wall and  $We$  is the Weber number,  $We = \sigma/(\rho_1 W_0^2 R)$ ,  $\sigma$  is the surface tension.  $N$  is the gas to liquid dynamic viscosity ratio and  $Q$  is the gas to liquid density ratio.

The solution to Eq. (7) is sought in the form of the Fourier-Bessel series;

**Table 1 Demonstration of convergence of the eigenvectors,  $Re = 400$ ,  $Re/Fr = 0$ ,  $We = 0.0025$ ,  $Q = 0.0013$ ,  $N = 0.018$ ,  $\beta = 10$ ,  $k = 0.3$**

$L$	$N_1$	$N_2$	$\eta(-1, 1)$
1	3	15	0.001704
2	3	15	0.001818
3	3	15	0.001834
2	2	8	0.001797

$$\psi_1(r, z, t) = r \sum_{n=1}^N F(\lambda_{1n}r) \sum_{l=0}^L [a_{1nl}(t) \cos(lkz) + b_{1nl}(t) \sin(lkz)] \quad (10)$$

where, following Lin and Ibrahim (1990),

$$F(\lambda_{1n}r) = J_1(\lambda_{1n}r) \quad (11)$$

$$F(\lambda_{2n}r) = J_1(\lambda_{2n}r) Y_1(\lambda_{2n}\beta) - J_1(\lambda_{2n}\beta) Y_1(\lambda_{2n}r) \quad (12)$$

where  $J_1$  and  $Y_1$  are the first-order Bessel functions of the first and second kind, respectively,  $k$  is the wave number, and  $\lambda_{1n}$  are obtainable from the orthogonality conditions of  $F(\lambda_{1n}r)$  given by

$$\lambda_{1n} J_0(\lambda_{1n}) - J_1(\lambda_{1n}) = 0 \quad (13)$$

$$\lambda_{2n} F'(\lambda_{2n}) - F(\lambda_{2n}) = 0 \quad (14)$$

where  $J_0$  is the Bessel function of the zero order of the first kind, and

$$F'(\lambda_{2n}) = J_0(\lambda_{2n}) Y_1(\lambda_{2n}\beta) - J_1(\lambda_{2n}\beta) Y_0(\lambda_{2n}) \quad (15)$$

where  $Y_0$  is the Bessel function of the zero order of the second kind.

To obtain the even mode of the governing equations we multiply Eq. (7) by  $F(\lambda_{1n}r) \cos(lkz)$  and integrate with respect to  $r$  between the limits  $e_1$  and  $q_1$  for the liquid and the limits  $e_2$  and  $q_2$  for the gas where,  $e_1 = 0$ ,  $q_1 = e_2 = (1 + \eta)$ ,  $q_2 = \beta$ , and integrate with respect to  $z$  between the limits 0 and  $2\pi/k$ , where

$$\eta(z, t) = [h(z, t) - 1]$$

is the dimensionless free surface displacement with  $h$  being the distance from jet free surface to jet axis. Using a Taylor series expansion about  $r = 1$  we can express integrations between the limits 1 and  $(1 + \eta)$  as,

$$\int \Lambda_{1m} dr = \sum_{n=0}^K [\eta^{n+1}/(n+1)!] (d^n \Lambda_{1m}/dr^n)_{r=1}$$

where  $\Lambda_{1m}$  is any function of  $r$ , and  $K$  is the number of terms in the Taylor series expansion required for convergence of the series within a specific tolerance. The solution of  $\eta(z, t)$  is sought in a Fourier series of the form

$$\eta(z, t) = \sum_{l=0}^L [c_l(t) \cos(lkz) + d_l(t) \sin(lkz)]. \quad (16)$$

The odd mode of the governing equations is obtained by multiplying Eq. (7) by  $F(\lambda_{1n}r) \sin(lkz)$  and integrating with respect to  $r$  between the limits  $e_1$  and  $q_1$  for the liquid and the limits  $e_2$  and  $q_2$  for the gas and integrating with respect to  $z$  between the limits 0 and  $2\pi/k$ . Here,  $j = 0, 1, 2, \dots, L$  and  $m = 1, 2, \dots, N_1$  for liquid and  $m = 1, 2, \dots, N_2$  for gas, where  $N_1$ ,  $N_2$ , and  $L$  are the number of terms in Eq. (10) required to yield a sufficiently accurate representation of  $\psi_1(r, z, t)$ . The reason behind including only  $(N_2 - 5)$  equations of the governing equations of the gas is that only five of the eight boundary conditions are not readily satisfied by the series representation in Eq. (10) and that we are adopting the Lanczos (1956) tau method in our solution by the Spectral method. The three boundary conditions that are readily satisfied by Eq. (10) are those which require finite radial and axial components of disturbance velocity along the jet axis and the vanishing of the

radial component of velocity at the wall. The remaining five boundary conditions are those which require zero axial velocity at the wall, continuous radial and axial velocity, tangential stresses and normal stresses at the liquid-gas interface, which can be written in equation form as,

$$w_2(\beta, z) = 0 \quad (17)$$

$$u_1(h, z) = u_2(h, z) \quad (18)$$

$$W_1(h) + w_1(h) = W_2(h) + w_2(h) \quad (19)$$

$$[u_{1z}(h, z) + W_{1z}(h) + w_{1z}(h, z)] = N[u_{2z}(h, z) + W_{2z}(h) + w_{2z}(h, z)] \quad (20)$$

$$- \{ -[P_1(h) + p_1(h, z)] + (2/Re)u_{1z}(h, z) \} + \{ -[P_2(h) + p_2(h, z)] + (2N/Re)u_{2z}(h, z) \} - We(1 - \eta + \eta^2 - \eta_{zz} - \eta_z^2/2) = 0, \quad (21)$$

respectively. Note that the last term in Eq. (21), which represents the surface tension stresses, is simplified to its second-order form in disturbance components (Ibrahim, 1989). We are going to adopt only second-order analysis in the present work due to the complexity of the equations. The boundary conditions in Eq. (18) through Eq. (21) apply at the liquid-gas interface which is not known *a priori*. These boundary conditions are expanded in the Taylor series of second order. Carrying out this expansion and using the basic state boundary conditions, Eq. (17) through Eq. (21) become, in terms of the disturbance stream function,

$$\psi_{2z}(\beta, z) = 0 \quad (22)$$

$$\psi_{2z}(1, z) - \psi_{1z}(1, z) = \eta \{ [\psi_{1rz}(1, z) - \psi_{1z}(1, z)] - [\psi_{2rz}(1, z) - \psi_{2z}(1, z)] \} \quad (23)$$

$$\eta[W_{2z}(1) - W_{1z}(1)] + (\eta^2/2)[W_{2zz}(1) - W_{1zz}(1)] = [-\psi_z(1, z) - \eta(\psi_{zz}(1, z) - \psi_z(1, z))] \quad (24)$$

$$[(\rho/\rho_1)(\psi_{zz} - (\psi_z - \psi_{zz})) + \eta(\psi_{rz} - \psi_{zz}) + \eta(-(\partial_z^2 \psi_z)_{z=1} + (\psi_{zz} - \psi_{zz}))] = (1 - Q)(Re/Fr)(\eta^2 - \eta) \quad (25)$$

$$[(\rho/\rho_1)Re(\psi_{zz} - \eta\psi_{zzz} - \eta_z\psi_{zz}) - W_z(1)\psi_z - \psi_z(\psi_z - \psi_{zz}) + (W_z(1) - \psi_z)\psi_{zz} - W_z(1)\eta\psi_{zzz} - W_z(1)\eta_z\psi_{zz}] + (\mu/\mu_1)[-(\partial_z^2 \psi_z)_{z=1} - (3\psi_{zzz} - 2\psi_{zz}) + \eta[(3\psi_{zzz} - \psi_{zzz} - 4\psi_{zz}) + \psi_{zzzz}] + \eta_z[(3\psi_{zzz} - \psi_{zzz} - 4\psi_{zz}) + \psi_{zzzz}]] + Re We(\eta_z + \eta_{zzz} - 2\eta\eta_z + \eta_z^2) = 0, \quad (26)$$

where  $\mu$  is the dynamic viscosity. An additional equation is needed to account for the unknown  $\eta$ . This equation is obtained from the relation between the radial component of velocity of the liquid at the liquid-gas interface  $u_z(h, z)$  and  $\eta$ :

$$u_z(h, z) = D\eta/Dt. \quad (27)$$

The boundary conditions corresponding to the even and odd modes are obtained by multiplying Eq. (22) through Eq. (27) by  $\cos(lkz)$  and  $\sin(lkz)$ , respectively, and integrating with respect to  $z$  between the limits 0 and  $2\pi/k$ .

The number of unknowns is equal to the number of equations is equal to  $2(L + 1)(N_1 + N_2) + 2(L + 1)$ . The problem is solved as an initial-value problem with the initial conditions given by the solution of the corresponding linear problem as obtained by Lin and Ibrahim (1990). A fourth-order multistep predictor corrector scheme described in Burden and Faires (1985) is used. The values of  $N_1$ ,  $N_2$ , and  $L$  are chosen to be 3, 15, and 2, respectively, as justified by the results of the convergence test shown in Table 1. More details on the solution procedure can be found in Ibrahim (1989).

## Results and Discussion

Figure 2 depicts a comparison between the linear and nonlinear predictions of temporal evolution of the free surface displacement in the atomization mode. The linear solution is

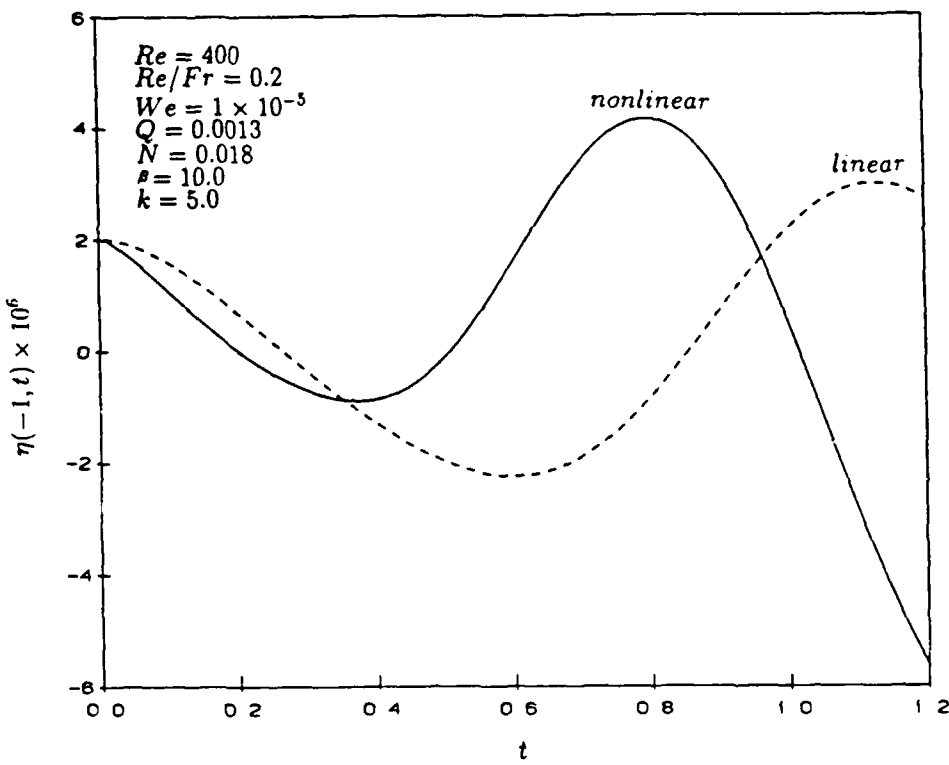


Fig. 2 Comparison of the linear and nonlinear predictions of the temporal evolution of the interface displacement in the atomization mode

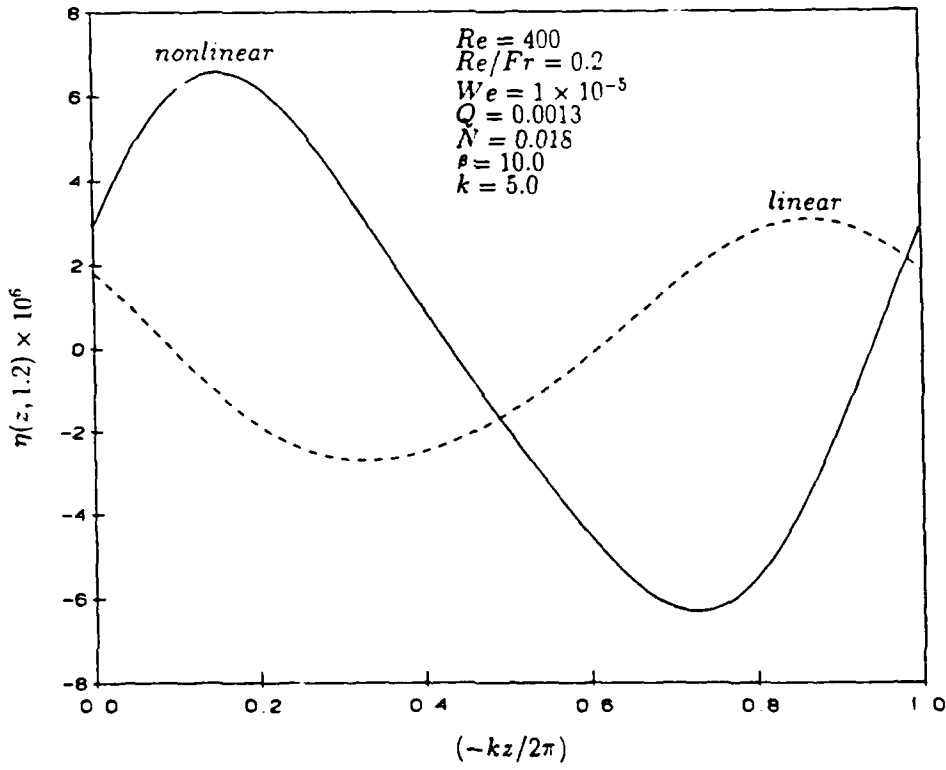


Fig. 3 Comparison of the linear and nonlinear predictions of the interfacial profile in the atomization mode

being that of Lin and Ibrahim (1990). It is seen that the nonlinear analysis predicts a peak that occurs sooner and reaches a higher magnitude than that of the linear analysis. In other words, the initial temporal evolution of finite disturbances occurs at a higher growth rate and frequency than those as-

sociated with infinitesimal disturbances. This means that finite disturbances are more unstable than infinitesimal disturbances which leads to the conclusion that if linear theory predicts that a jet is unstable to infinitesimally small disturbances, then nonlinear theory further predicts that the disturbances will

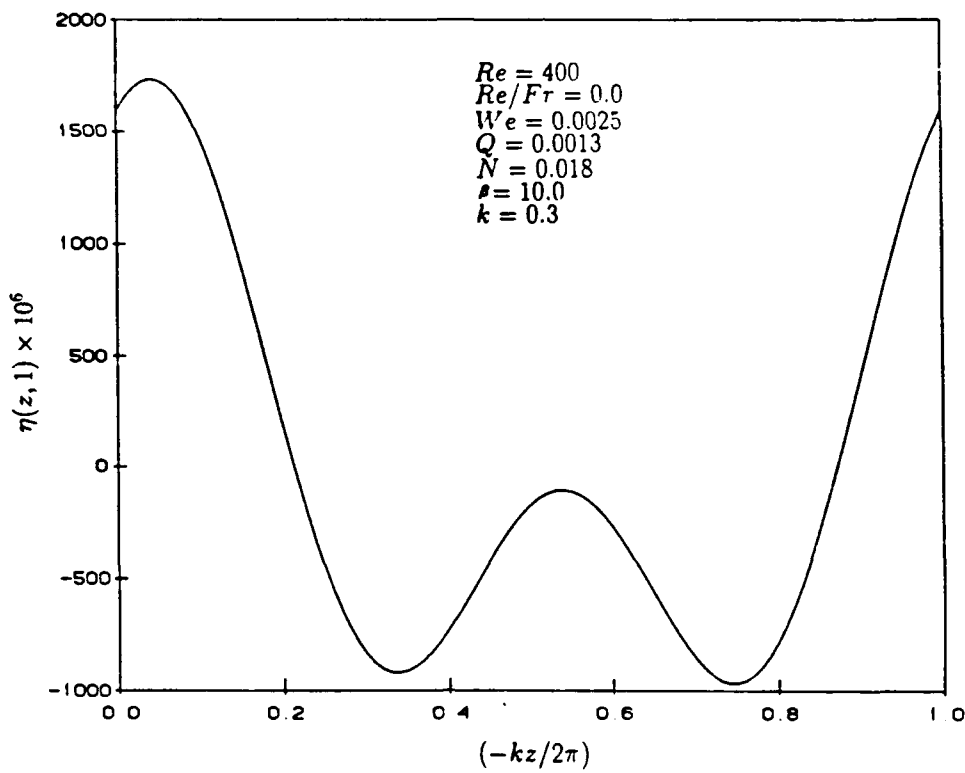


Fig. 4 Nonlinear interfacial profile in the capillary mode.  $\psi(-1, 0) = 0.00148$

continue to grow after they become finite and ultimately the jet will be atomized.

Figure 3 describes the interfacial profile of the jet surface in the atomization mode as predicted by both the linear and nonlinear analyses. The horizontal axis is normalized with  $(-k/2\pi)$  so that the interfacial profile is depicted for one wavelength  $2\pi/k$ . Since the present analysis is temporal, this profile repeats itself every wavelength  $2\pi/k$ . The negative sign in the normalization  $(-k/2\pi)$  is to make the horizontal coordinate increase in the flow direction since the axial coordinate  $z$  is chosen to be negative downward as shown in Fig. 1. Figure 3 shows that the nonlinear analysis produces larger deformation of the jet surface than the linear instability analysis. This would eventually result in larger droplet size, after disintegration of the jet, than those that would be predicted by the linear analysis.

Figure 4 shows the configuration of the liquid-gas interface in the capillary mode of instability as predicted by the nonlinear analysis. It is seen that the initially sinusoidal wave develops into an asymmetric wave with a higher harmonic. This higher harmonic was discovered in the analysis of Yuen (1968) and the experiments conducted by Rutland and Jameson (1970), Lafrance (1975), and Taub (1976) among others. The asymmetry is due to the higher harmonics as well as feedback into the fundamental. Since the present analysis is only of second order, we don't expect to see more than one swelling between the crests of the primary disturbance waves. As a matter of fact, this is exactly what Rutland and Jameson (1970) and Lafrance (1975) observed up to the point of jet breakup. After breakup, of course, the ligaments between large drops can often disintegrate further, in which case many undulations per primary wavelength could be observed as reported by Rutland and Jameson (1970). However, Taub (1976) reported up to three undulations before jet breakup. It should be noted that, our results are obtained at a much smaller time than those of other authors and hence the amplitude of the interface displacement in Fig. 4 is much smaller. Unfortunately, the CPU

time required to advance the solution one dimensionless time unit was too large to attempt to obtain results at a larger time.

The occurrence of higher harmonics explains the common observation that once the jet breakup it disintegrates into droplets of various sizes. This is in contrast to the predictions of the linear theory of jet disintegration into droplets of uniform size.

Referring back to Fig. 3, it is obvious that, unlike Rayleigh mode, the results don't indicate any higher harmonics for the atomization mode. This could be explained by observing that the amplitude of the interface displacement in the capillary mode is two order of magnitudes larger than in the atomization mode so it is easier for internodal undulation of finite amplitude to take place in the capillary mode. Also, the higher growth rates and frequencies associated with the atomization mode could be the reason why it is improbable for asymmetry to set in. However, it is possible that if the nonlinear solution is carried out for a larger time, we will see higher harmonics for the atomization mode. Such an investigation was not carried out because of the enormous CPU time required.

### Conclusions

While no nonlinear stability was found for unstable linear disturbances, stable linear disturbances were found to be also stable with respect to weakly nonlinear disturbances in a wide range of flow parameters. The nonlinear instability of the atomization mode indicated that finite disturbances are more unstable than infinitesimally small disturbances. No higher harmonics are observed for the atomization mode for the time range investigated.

Asymmetry of the interfacial profile is revealed in the nonlinear analysis of capillary instability. This explains the observed satellite formation in ink jets. The amplitude of the interfacial disturbances are two order of magnitude larger than those associated with the atomization mode of instability. Lin-

ear theories are adequate for predicting the onset of either the Rayleigh or the Taylor mode instability. The outcome of atomization process requires fully nonlinear treatment.

### Acknowledgments

This work was funded in part by Grant No. DAAL 03-89-K-0179 of ARO, Grant No. MSM-8817372 of NSF and a New York State Science and Technology Foundation Grant. The computations were carried out with the computer facility at Clarkson University and with the Cornell National Supercomputer Facility, which is founded by the NSF, the State of New York, and IBM Corporation.

### References

Bogy, D. B., 1978a, "Use of One-Dimensional Cosserat Theory to Study Instability in a Viscous Liquid Jet," *Physics Fluids*, Vol. 21, pp. 190-197.

Bogy, D. B., 1978b, "Wave Propagation and Instability in a Circular Semi-Infinite Liquid Jet Harmonically Forced at the Nozzle," *ASME JOURNAL OF APPLIED MECHANICS*, Vol. 45, pp. 469-474.

Bogy, D. B., 1979, "Breakup of a Liquid Jet: Third Perturbation Cosserat Solution," *Physics Fluids*, Vol. 22, pp. 224-230.

Burden, R. L., and Faires, J. D., 1985, *Numerical Analysis*, 3rd ed., Prindle, Weber and Schmidt.

Chaudhary, K. C., 1977, "The Nonlinear Capillary Instability of a Jet," Ph.D. Thesis, University of Southern California, Los Angeles, Calif.

Chaudhary, K. C., and Redekopp, L. C., 1980a, "The Nonlinear Capillary Instability of a Liquid Jet, Part I Theory," *J. Fluid Mech.*, Vol. 96, pp. 257-274.

Chaudhary, K. C., and Maxworthy, T., 1980b, "The Nonlinear Capillary Instability of a Liquid Jet, Part 2: Experiments on the Jet Behaviors before Droplet Formation," *J. Fluid Mech.*, Vol. 96, pp. 275-284.

Green, A. E., 1976, "On the Nonlinear Behavior of Fluid Jets," *Int. J. Engng. Sci.*, Vol. 14, pp. 49-63.

Ibrahim, E. A., 1989, "Linear and Nonlinear Instability of a Liquid Jet in a Viscous Gas," Ph.D. Dissertation, Clarkson University, Potsdam, N.Y.

Keller, J. B., Rubinow, S. I., and Tu, Y. O., 1973, "Spatial Instability of a Jet," *Physics Fluids*, Vol. 16, pp. 2052-2055.

Lafrance, P., 1975, "Nonlinear Break-up of a Liquid Jet," *Physics Fluids*, Vol. 18, pp. 428-432.

Lanczos, C., 1956, *Applied Analysis*, Prentice-Hall, Englewood Cliffs, N.J.

Lee, H. C., 1974, "Drop Formation in a Liquid Jet," *IBM J. Res. Dev.*, Vol. 18, pp. 364-369.

Lin, S. P., and Creighton, B., 1990, "Energy Budget in Atomization," *Aerosol Sci. Tech.*, Vol. 12, No. 3, pp. 630-636.

Lin, S. P., and Ibrahim, E. A., 1990, "Instability of a Viscous Liquid Jet Surrounded by a Viscous Gas in a Vertical Pipe," *J. Fluid Mech.*, Vol. 218, pp. 641-658.

Lin, S. P., and Lian, Z. W., 1990, "Mechanisms of the Breakup of Liquid Jets," *AIAA J.*, Vol. 28, pp. 120-126.

Neyfeh, A. H., 1970, "Nonlinear Stability of a Liquid Jet," *Physics Fluids*, Vol. 13, pp. 841-847.

Phinney, R. E., 1972, "The Breakup of a Turbulent Liquid Jet in a Gaseous Atmosphere," *J. Fluid Mech.*, Vol. 60, pp. 689-701.

Rutland, D. F., and Jameson, G. J., 1970, "A Nonlinear Effect in the Capillary Instability of Liquid Jets," *J. Fluid Mech.*, Vol. 46, pp. 267-271.

Shokohi, F., and Elrod, H. G., 1987, "Numerical Investigation of the Disintegration of Liquid Jets," *J. Comp. Physics*, Vol. 71, pp. 324-342.

Taub, H. H., 1976, "Investigation of Nonlinear Waves on Liquid Jets," *Physics Fluids*, Vol. 19, pp. 1124-1129.

Wang, D. P., 1968, "Finite Amplitude Effect on the Stability of a Jet of Circular Cross-Section," *J. Fluid Mech.*, Vol. 34, pp. 299-313.

Yuen, M. C., 1968, "Nonlinear Capillary Instability of a Liquid Jet," *J. Fluid Mech.*, Vol. 33, pp. 151-163.

(APPENDIX B )

## **Effects of Compressibility on the Atomization of Liquid Jets**

**Z. W. Zhou and S .P. Lin**

Reprinted from

## **Journal of Propulsion and Power**

Volume 8, Number 4, July-August 1992, Pages 736-740

**AIAA**

*A publication of the*

American Institute of Aeronautics and Astronautics, Inc  
The Aerospace Center, 370 L'Enfant Promenade, SW  
Washington, DC 20024-2518

# Effects of Compressibility on the Atomization of Liquid Jets

Z. W. Zhou\* and S. P. Lint  
Clarkson University, Potsdam, New York 13699

The effect of compressibility of fluids on the atomization of a liquid jet emanating from a nozzle into the ambient gas is investigated by use of linear stability analysis. An increase in the compressibility of the liquid gas is shown to promote the generation of smaller droplets, although at a slower rate. It is shown that in some parameter ranges, a small change in compressibility may result in a qualitative change of the mechanism of atomization.

## Introduction

**A**TOMIZATION is a process of breaking up a liquid jet into droplets of diameter much smaller than the jet diameter. This process is widely used in industrial applications including fuel injections in internal combustion engines. A good knowledge of the fundamental mechanism of atomization is essential for raising the combustion efficiency and reducing the environmental pollution. Our understanding of atomization is not yet complete.

A concise review of experimental and theoretical work on atomization was given by Reitz and Bracco.<sup>1,2</sup> A more extensive exposition of the subject can be found in the work of Lefebvre.<sup>3</sup> The atomization process as the consequence of the aerodynamic instability of a jet emanated into ambient gas was investigated by Taylor,<sup>4</sup> Levich,<sup>5</sup> and others. They considered instability with respect to temporally growing disturbances. Atomization as the consequence of convective instability caused by spatially growing disturbances was studied by Lin and Kang,<sup>6</sup> Lin and Lian,<sup>7</sup> and Lin and Creighton.<sup>8</sup> In all of the theoretical works mentioned above, the fluids are assumed to be incompressible. On the other hand in many applications, the jet speed is such that the Mach number of the ambient gas relative to the jet may reach transonic. For future applications it may even reach supersonic. Therefore, the compressibility of the fluids must be taken into account.

Here, we investigate the effects of compressibility on atomization. The problem of instability of an inviscid compressible jet emanating into an inviscid compressible gas is formulated in the next section. The disturbance is allowed to grow both temporally and spatially. The results of the solution to the formulated problem are used to demonstrate that the compressibility brings about not only quantitative but also qualitative differences in the mechanism of atomization at its onset.

## Formulation of Problem

Consider the onset of instability of a jet of inviscid compressible fluid emanating from a circular cylindrical nozzle of radius  $a$  into an unbounded inviscid compressible fluid. The governing equations of motions are

$$\rho_i(\partial_t + \mathbf{V} \cdot \nabla) \mathbf{V}_i = -\nabla P_i \quad (1)$$

Received May 31, 1991; revision received Sept. 9, 1991; accepted for publication Oct. 4, 1991; presented as Paper 92-0459 at the AIAA 30th Aerospace Sciences Meeting, Reno, NV, Jan. 6-9, 1992. Copyright © 1991 by the American Institute of Aeronautics and Astronautics, Inc. All rights reserved.

\*Postdoctoral Fellow, Department of Mechanical and Aeronautical Engineering.

†Professor, Department of Mechanical and Aeronautical Engineering, Member AIAA.

$$\partial_t \rho_i + \nabla \cdot (\rho_i \mathbf{V}_i) = 0 \quad (i = 1, 2) \quad (2)$$

where the subscripts  $i = 1, 2$  denote respectively the jet fluid and the ambient field,  $\rho$  is density,  $t$  is time,  $\mathbf{V}$  is the velocity vector, and  $P$  is the dynamic pressure. The basic state that satisfies Eqs. (1) and (2) exactly in the absence of gravity is given by

$$\mathbf{V}_1 = (\bar{U}_1, \bar{V}_1, \bar{W}_1) = (0, 0, W_0), \quad \bar{\rho}_1 = \text{constant}$$

$$\bar{P}_1 = \text{constant}, \quad (0 \leq R \leq a)$$

$$\mathbf{V}_2 = (\bar{U}_2, \bar{V}_2, \bar{W}_2) = (0, 0, 0), \quad \bar{\rho}_2 = \text{constant}$$

$$\bar{P}_2 = \bar{P}_1 - S/a, \quad (a < R < \infty)$$

where the overbar denotes the basic state quantities.  $U$ ,  $V$ , and  $W$  are respectively, the radial, azimuthal and axial components of velocity in the cylindrical coordinate system ( $R$ ,  $\theta$ ,  $Z$ ).  $W_0$  is the constant jet speed, and  $S$  is the surface tension.  $Z$  is positive in the flow direction. The basic state liquid jet is of constant radius with smooth surface. Thus neither shock waves nor Mach waves exist in the gas and the liquid jet, and the densities in both fluids are constant in the basic state.

We investigate the stability of this basic state with respect to the disturbance defined by

$$\mathbf{V}_i = \bar{\mathbf{V}}_i + \mathbf{V}'_i, \quad \rho_i = \bar{\rho}_i + \rho'_i, \quad P_i = \bar{P}_i + P'_i \quad (3)$$

where primes are used to designate the perturbations of the variables. Substituting Eq. (3) into Eqs. (1) and (2), retaining only linear terms, we have

$$(\partial_t + \delta_1 W_0 \partial_Z) \mathbf{V}'_1 = -\nabla P'_1 \quad (4)$$

$$(\partial_t + \delta_1 W_0 \partial_Z) \rho'_1 = -\bar{\rho}_1 \nabla \cdot \mathbf{V}'_1 \quad (5)$$

where  $\delta_1$  is 1 or 0 depending on if  $i = 1$  or  $i \neq 1$ . Taking the divergence of Eq. (4) and then using Eq. (5), we have

$$(\partial_t + \delta_1 W_0 \partial_Z)^2 \rho'_1 = \nabla^2 P'_1 \quad (6)$$

$P'_1$  and  $\rho'_1$  are related locally by the speed of sound  $c_s^2 = dP'_1/d\rho'_1$ . Thus Eq. (6) can be written as

$$(\partial_t + \delta_1 W_0 \partial_Z)^2 P'_1 = c_s^2 \nabla^2 P'_1 \quad (7)$$

The corresponding linearized boundary conditions for Eq. (7) at the interface  $R = a + d$  are the dynamic force balance

$$P'_1 - P'_2 = S(a^2 - a^2 \partial_{rr} - \partial_{zz})d \quad (8)$$

and the kinematic conditions

$$(\partial_r + \delta_r W_r)^2 d = -\rho_r^{-1} \partial_r P' \quad (9)$$

where  $d$  is the displacement of the interface from the basic state cylindrical surface. Note that  $P'$  in Eqs. (8) and (9) are to be applied at  $R = a$ .

The normal mode solution of the differential system Eqs. (7), (8), and (9) will be sought in the form

$$\begin{bmatrix} P'_1 \\ P'_2 \\ d \end{bmatrix} = \begin{bmatrix} \rho_1 W_r^2 p_1(r) \\ \rho_1 W_r^2 p_2(r) \\ af \end{bmatrix} \exp[i(kz + n\theta - \omega\tau)] \quad (10)$$

where  $(r, z, f)$ , and  $\tau$  are dimensionless variables defined by  $(r, z, f) = (R, Z, d)a^{-1}$ , and  $\tau = t(W_r/a)$ ; and  $(k, n)$  and  $\omega$  are the dimensionless wavenumber vector and wave-frequency, respectively.

Substitution of Eq. (10) into Eqs. (7), (8), and (9) yields the governing equation for the dimensionless perturbation pressure amplitudes

$$\{D^2 + r^{-1}D - [n^2 r^{-2} + k^2 - M_1^2(k - \omega)^2]\}p_1 = 0 \quad (11)$$

$$\{D^2 + r^{-1}D - [n^2 r^{-2} + k^2 - M^2 \omega^2]\}p_2 = 0 \quad (12)$$

and the corresponding boundary conditions at  $r = 1$

$$p_2 - p_1 + W_r(k^2 + n^2 - 1)f = 0 \quad (13)$$

$$(k - \omega)^2 f - p'_1 = 0 \quad (14)$$

$$Q\omega^2 f - p'_2 = 0 \quad (15)$$

where

$$W_r = S/\bar{\rho}_1 W_r^2 a, \quad Q = \bar{\rho}_2/\bar{\rho}_1, \quad M_1 = W_r/c_1,$$

$$M = W_r/c_2, \quad D = \partial/\partial r$$

Note that  $W_r$  is the Weber number,  $M_1$  is the Mach number of the jet, and  $M$  is the Mach number of the ambient fluid with respect to a frame of reference moving with the jet at a speed  $W_r$ . The bounded solution of Eqs. (11) and (12) are

$$p_1 = AI_n(\lambda_1 r), \quad \lambda_1 = [k^2 - M_1^2(k - \omega)^2]^{1/2}$$

$$p_2 = BK_n(\lambda_2 r), \quad \lambda_2 = [k^2 - M^2 \omega^2]^{1/2}$$

where  $A$  and  $B$  are the integration constants and  $I_n$  and  $K_n$  are respectively the modified Bessel function of the first and second kinds. Substitution of these solutions into Eqs. (14) and (15) yields

$$A = (k - \omega)^2 f / I'_n(\lambda_1) \lambda_1$$

$$B = Q\omega^2 f / K'_n(\lambda_2) \lambda_2$$

where primes now denote the differentiation  $d/d(\lambda, r)$ . It follows from Eq. (13) that

$$D_n = \frac{(k - \omega)^2 I_n(\lambda_1)}{\lambda_1 I'_n(\lambda_1)} - \frac{Q\omega^2 K_n(\lambda_2)}{\lambda_2 K'_n(\lambda_2)} - W_r(k^2 + n^2 - 1) = 0 \quad (16)$$

For a given set of four flow parameters  $W_r$ ,  $Q$ ,  $M_1$ , and  $M$ , this is the secular equation the solution of which gives the characteristic wave frequency  $\omega$  and the wavenumber  $k$ .

For the special case of an incompressible jet in a vacuum,  $Q = 0$ ,  $c_1 \rightarrow \infty$ ,  $c_2 \rightarrow 0$ , thus  $\lambda_1 \rightarrow k$ ,  $\lambda_2 \rightarrow \infty$  and Eq. (16) is reduced to, if  $\omega$  remains finite

$$\frac{I_n(k)(k - \omega)^2}{I'_n(k)} + k(1 - k^2 - n^2)W_r = 0 \quad (17)$$

This is the characteristic equation used by Keller et al.<sup>9</sup> and Leib and Golstein<sup>10</sup> in their studies of the spatial instability of the Rayleigh jet. For the special case of an incompressible jet emanating into an incompressible fluid,  $M$ ,  $M_1 \rightarrow 0$ , thus  $\lambda_1 = \lambda_2 = k$ , and Eq. (16) is reduced to, if  $\omega$  remains finite:

$$\frac{(k - \omega)^2 I_n(k)}{I'_n(k)} - \frac{Q\omega^2 K_n(k)}{K'_n(k)} - k(k^2 + n^2 - 1)W_r = 0 \quad (18)$$

This equation agrees with Eq. (1) of Lin and Lian<sup>7</sup> when the Reynolds number of their equation is let to approach infinity and their  $\omega$  and  $k$  are respectively replaced by  $-i\omega$  and  $-k$ . This change of variable is necessary because of the different positive axial directions and the different definitions of the wave-frequency which are used in these two papers. When the surface tension is put to zero, Eq. (16) reduces to the characteristic equation corresponding to that of Tam et al.<sup>11</sup> except their equation is in terms of the Hankel function and the Bessel function of the first kind. It is known that the axisymmetric disturbance grows the fastest in an incompressible jet in the absence<sup>9</sup> or presence<sup>12</sup> of the ambient field. Here we assume that the same is true for a compressible jet. Hence we treat the case of  $n = 0$  in Eq. (16). Here both  $\omega = \omega_r + i\omega_i$  and  $k = k_r + ik_i$  are complex. Their imaginary parts  $\omega_i$  and  $k_i$  give respectively the temporal and the spatial growth rates. Their real parts are the wave frequency and the wave number respectively.

## Results

In order to demonstrate the significant effect of compressibility on the atomization of liquid jets, we present first the results obtained with the assumption that the fluids involved are incompressible. Figure 1 shows the dependence of the spatial amplification rate  $k_r$  on the wave number  $k$ , for the flow parameters shown in the figure caption.  $M_1 = M = 0$  implies that both the liquid jet and the ambient gas are incompressible. The values of  $W_r = 10^{-5}$  and  $Q = 0.0013$  correspond to the case of a water jet emanated at a speed of 201 m/s from a nozzle of radius 0.18 mm into room temperature air under 1 atmospheric pressure. These values are en-

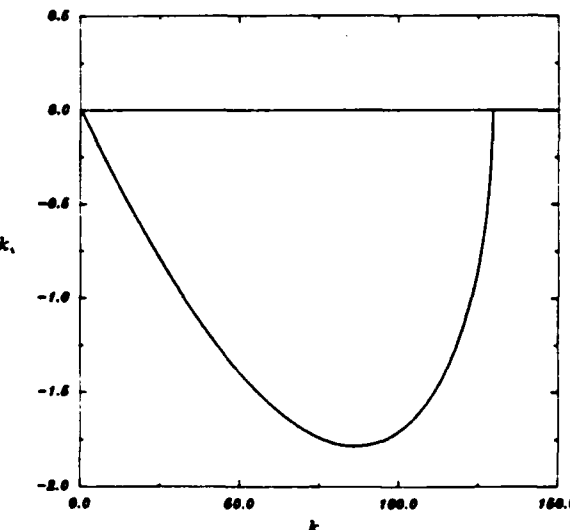


Fig. 1 Convective instability of incompressible jet  $Q = 0.0013$ ,  $W_r = 0.00001$ ,  $M_1 = 0.0$ ,  $M = 0.0$ .

countered in many common applications. Along the curve in this figure,  $\omega_r = 0$ . It is seen from Eq. (10) that the negative value of  $k_r$  signifies spatial growth of the disturbance amplitude in the flow direction, and  $\omega_r = 0$  signifies zero temporal growth of the disturbance. Thus the jet under the specified parameter condition exhibits convective instability.<sup>13,14</sup> However, these results were obtained with the assumption that both the liquid jet and the ambient gas are incompressible. Actually both fluids are compressible, and the Mach number of the above water jet flowing at a speed of 201 m/s is 0.135. The corresponding convective Mach number of the ambient air, i.e., the Mach number of the air relative to a reference frame moving with the jet, is 0.59. With these values of Mach numbers and the rest of the flow parameters remaining the same as that in Fig. 1, we obtained the solution curves of the dispersion equation (16). The results are presented in Fig. 2. There are three branches of the spatial growth curve  $\omega_r = 0$ . The constant frequency curves  $\omega_r = 2.845$  and  $\omega_r = 2.866$  being initiated from the upper half plane approach the left and right branches respectively as the values of  $\omega_r$  are decreased from some positive values toward zero. Along the left and right branches,  $\omega_r$  decreases and increases respectively with  $k_r$ . The group velocities of disturbances, being given by the derivation of  $\omega_r$  with respect to  $k_r$ , are in the downstream and upstream directions respectively for the left and right branches. Note the existence of a saddle point with the value of  $\omega_r$  lying between 2.845 and 2.866. At this point  $D_0 = \partial D_0 / \partial k_r = 0$ , and the group velocity is zero. According to the theories of Briggs<sup>13</sup> and Bers,<sup>14</sup> the appearance of the saddle point signifies that the integration path in the Fourier integral representation cannot be analytically deformed continuously until  $\omega_r = 0$  is reached from above. The disturbance has to grow simultaneously in time and space, according to the theory of Briggs and Bers. Physically, while the atomization starts at some distance downstream of the nozzle in convective instability, the jet breakup starts right from the nozzle in absolute instability. A more precise quantitative physical consequence of absolute instability requires the solution of the initial value problem of nonlinear instability. A comparison of Fig. 1 with Fig. 2 clearly demonstrates the importance of the compressibility effect on the onset of atomization. It brings about a qualitative difference in the mechanism of atomization.

Absolute instability can be eliminated by increasing the compressibility. When the Mach numbers in Fig. 2 are quadrupled while the rest of parameters remain fixed, the saddle point is removed and the solution of Eq. (16) yields the amplification curve of convectively unstable disturbances shown

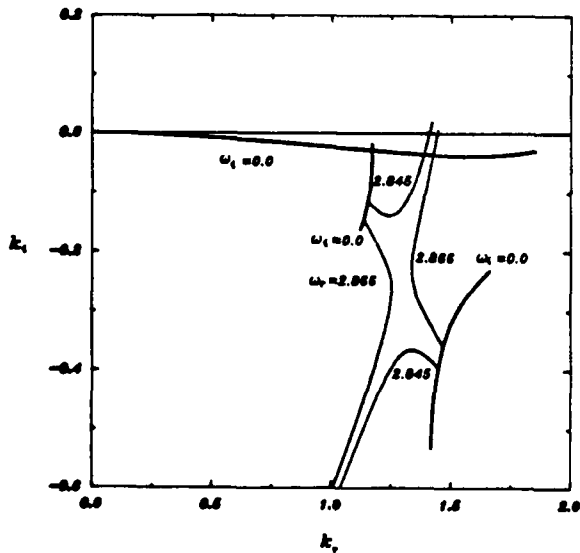


Fig. 2 Absolute instability of subsonic jet  $Q = 0.0013$ ,  $W_r = 0.00001$ ,  $M_1 = 0.135$ ,  $M = 0.59$ .

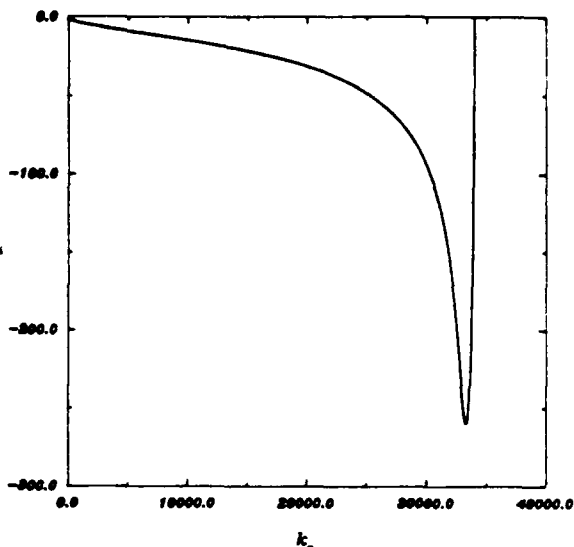


Fig. 3 Convective instability of subsonic jet  $Q = 0.0013$ ,  $W_r = 0.00001$ ,  $M_1 = 0.52$ ,  $M = 2.3$ .

in Fig. 3. Note that  $k_r$  becomes zero beyond the critical wave number  $k_r = 34,000$ . Thus the smallest atomized droplet according to the linear theory will have a radius of approximately 9  $\mu\text{m}$ . This estimate is obtained by using the assumption that a droplet is formed by capillary pinching at two consecutive troughs of the liquid jet. This estimate therefore tends to over predict the diameter since the droplets are actually formed from small ligaments branching out from the jet. The conservation of volume, then requires the following relation between the radius of droplet  $R$  and the wavelength of disturbance  $\lambda$ :

$$\pi a^2 \lambda = 4\pi R^3/3 \quad (19)$$

where  $\lambda$  is related to the wave number  $k_r$  by  $k_r = 2\pi a/\lambda$ . The estimated smallest droplet can be compared with that obtained by neglecting the compressibility effect. Referring back to Fig. 1, we see that the critical wave number above which the value of  $k_r$  becomes zero is approximately 130. By use of the same method, the smallest atomized droplets are estimated to be approximately 60  $\mu\text{m}$ . Thus the smallest droplet predicted by the theory without taking into account the compressibility effect is almost one order of magnitude larger than that when the compressibility effect is duly taken into account. If one reasonably assumes that the population of the droplets of a given diameter in a spray is proportional to the amplification rate  $-k_r$ , then a simple comparison of Figs. 1 and 3 clearly indicates that the size distributions in the sprays of compressible and incompressible fluids are quite different. An incompressible jet tends to produce a smaller range of droplet diameters but with a flatter distribution. It should be pointed out that although a high speed jet with  $M_1 = 0.52$  is seldom encountered in present day practice, it will probably be encountered in the future in high speed atomization for small droplets.

In the remainder of this work, we present the results demonstrating the effect of surface tension, ambient gas density, and jet speed on atomization. The values of flow parameters for each amplification curve are given in the figure caption. When the surface tension of the jet whose disturbance amplification curve is given by Fig. 3 is increased by a factor of 10, the amplification rate is reduced by a factor of approximately ten as shown in Fig. 4. This indicates that surface tension is stabilizing. The critical wave number is also reduced by a factor of approximately 10, and thus the diameter of the smallest size of droplet obtainable is increased by a factor of  $10^{1/3}$  (c.f. Eq. (19)). When the  $Q$  in Fig. 3 is increased by a factor of 10, the amplification rate is increased by a factor of

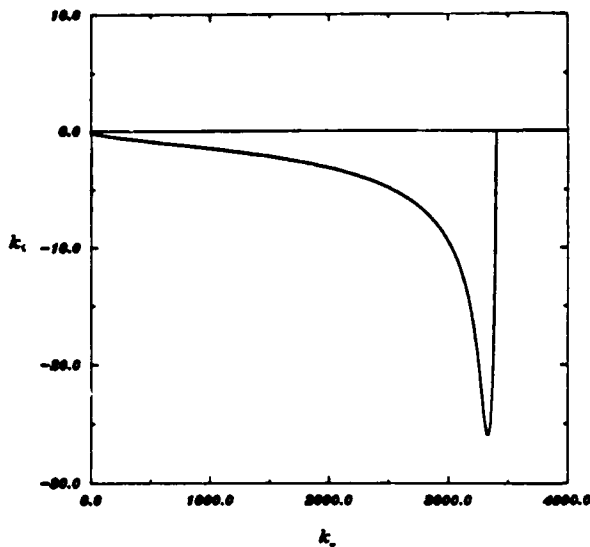


Fig. 4 Surface tension is stabilizing  $Q = 0.0013$ ,  $W_r = 0.0001$ ,  $M_r = 0.52$ ,  $M = 2.3$ .

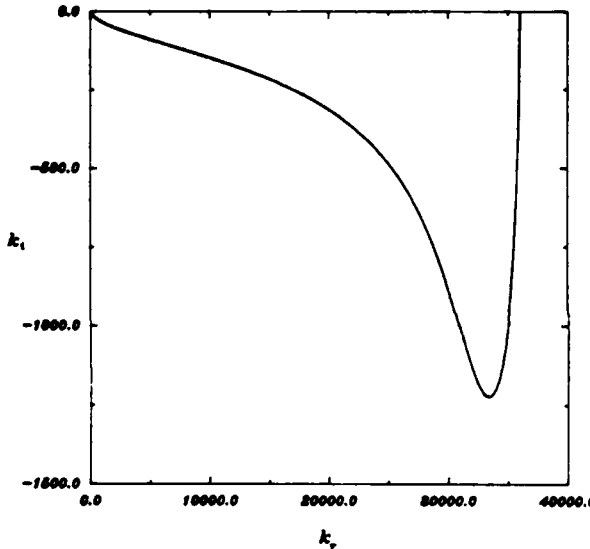


Fig. 5 Ambient gas promotes atomization  $Q = 0.013$ ,  $W_r = 0.00001$ ,  $M_r = 0.52$ ,  $M = 2.3$ .

approximately 4 as shown in Fig. 5. The critical wave number is only slightly increased. However, the amplification curve is considerably flattened. Thus the effect of increasing the ambient gas density, by increasing the gas pressure for example, is to enhance the atomization rate at the expense of getting a broader size distribution. When the Mach number of the jet for Fig. 3 is increased from 0.52 to a supersonic value of 1.25 with  $M$  fixed at 2.3, the amplification rate is slightly reduced and the critical wave number is slightly increased as shown in Fig. 6. For a given gas, this signifies that if the jet speed is kept constant but the speed of sound is reduced by a factor of  $0.51/1.25$ , one will observe a slight reduction in the rate of atomization. Thus, an increase in compressibility of the jet softens the atomization process, and the most populous droplet tends to have a slightly smaller diameter.

### Discussion

The Reynolds number corresponding to the examples given in Figs. 2 and 6 ranges from 20,000 to 75,000 if the jet liquid is water. This justifies the neglect of viscosity in the first approximation. Only the results for the axisymmetric mode are presented here. This is because the axisymmetric mode

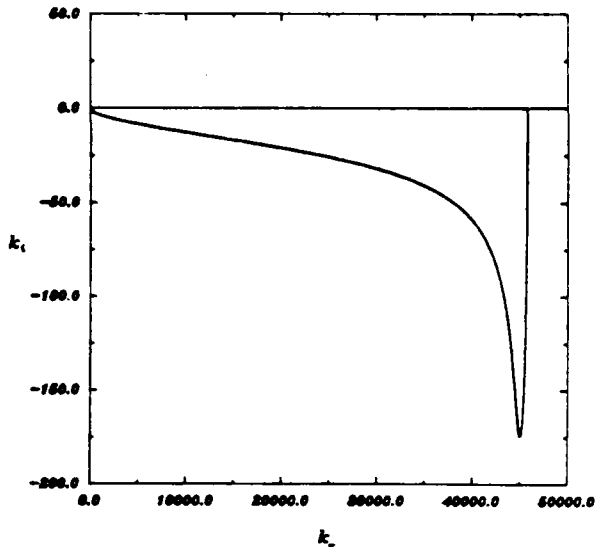


Fig. 6 Compressibility of jet reduces atomization rate  $Q = 0.0013$ ,  $W_r = 0.00001$ ,  $M_r = 1.25$ ,  $M = 2.3$ .

is the most unstable mode. This can be seen from Eq. (16). The first two terms in this equation arise from the pressure fluctuation which is destabilizing. The  $W_r$  term arises from the capillary effect. The first two terms in the parenthesis are positive and represent respectively the effect of stabilization by surface tension associated with the curvatures along the axial and azimuthal directions respectively. The only negative term in the parenthesis arises from the destabilizing capillary pinching perpendicular to the axial direction. Thus the non-axisymmetric modes associated with  $n \neq 0$  are more stable. The thin boundary-layer effect near the liquid-gas interface was discussed by Lin and Lian<sup>7</sup> and Lin and Ibrahim<sup>15</sup> for the case of incompressible fluids. The viscosity was found to be responsible for generating larger drops which scale with shear waves. The wavelength of shear waves is several orders of magnitude larger than the gas-capillary length  $S/\rho_r W_r^2 = W_r a/Q$ . Note that the wave length of the most amplified disturbance in Fig. 1 scales with this capillary length, since the wavelength  $\lambda = 2\pi a/k_r$ . On the other hand, the wavelengths of the most amplified disturbances given in Figs. 2 to 6 for compressible jet scale with the liquid-capillary length  $S/\rho_r W_r^2 = W_r a$ , this can be verified easily from the result given in these figures. However, the length scale of the shear waves mentioned above was obtained with a theory in which the compressibility effect is totally neglected. A theory which takes into account both the effect of viscosity and compressibility is not yet available. A nonlinear initial value problem for the elucidation of absolute instability in an atomizing jet is yet to be formulated.

### Acknowledgments

This work was supported in part by Grant DAAL03-89-K-0179 of ARO, Grant MSM-8817372 of NSF, and a New York State Science Foundation Grant. The computation was carried out with the computer facility at Clarkson University and with the Cornell National Computer facility, which is funded by the NSF, the State of New York, and IBM Corporation.

### References

- Reitz, R. D., and Bracco, F. V. "Mechanism of Atomization of a Liquid Jet." *Physics of Fluids*, Vol. 25, No. 10, 1982, pp. 1730-1742.
- Reitz, R. D., and Bracco, F. V. "Mechanisms of Breakup of Round Liquid Jets." *Encyclopedia of Fluid Mechanics*, Vol. 3, edited by N. P. Cheremisinoff, Gulf P. Houston, TX, 1986, pp. 233-249.

<sup>1</sup>Lefebvre, A. H., *Atomization and Sprays*, Hemisphere, New York, 1989.

<sup>2</sup>Taylor, G. I., "Generation of Ripples by Wind Blowing Over Viscous Fluids," *The Scientific Papers of G. I. Taylor*, Cambridge University Press, Cambridge, England, UK, 1963, Vol. 3, pp. 244-254.

<sup>3</sup>Levich, V. G., *Physicalchemical Hydrodynamics*, Prentice-Hall, Englewood Cliffs, NJ, 1962.

<sup>4</sup>Lin, S. P., and Kang, D. J., "Atomization of a Liquid Jet," *Physics of Fluids*, Vol. 30, July 1987, pp. 2000-2006.

<sup>5</sup>Lin, S. P., and Lian, Z. W., "Mechanism of Breakup of Liquid Jets," *AIAA Journal*, Vol. 28, No. 1, 1990, pp. 120-126.

<sup>6</sup>Lin, S. P., and Creighton, B., "Energy Budget in Atomization," *Aerosol Science and Technology*, Vol. 12, No. 2, 1990, pp. 630-636.

<sup>7</sup>Keller, J. B., Rubinow, S. I., and Tu, Y. O., "Spatial Instability of a Jet," *Physics of Fluids*, Vol. 16, Dec. 1972, pp. 2052-2055.

<sup>8</sup>Leib, S. J., and Goldstein, M. E., "The Generation of Capillary Instabilities on a Liquid Jet," *Journal of Fluid Mechanics*, Vol. 168, July 1986, pp. 479-500.

<sup>9</sup>Tam, C. K. W., and Hu, Q., "On the Three Families of Instability Waves of High Speed Jets," *Journal of Fluid Mechanics*, Vol. 201, April 1989, pp. 447-483.

<sup>10</sup>Lian, Z. W., and Lin, S. P., "Breakup of a Liquid Jet in a Swirling Gas," *Physics of Fluids A*, Vol. 2, No. 12, 1990, pp. 2134-2139.

<sup>11</sup>Briggs, R. J., *Electron Stream Interaction with Plasmas*, MIT Press, Cambridge, MA, 1964.

<sup>12</sup>Bers, A., *Handbook of Plasma Physics*, Vol. 1, North-Holland, Amsterdam, 1983, pp. 452-516.

<sup>13</sup>Lin, S. P., and Ibrahim, E. A., "Instability of a Viscous Liquid Jet Surrounded by a Viscous Gas in a Pipe," *Journal of Fluid Mechanics*, Vol. 218, Sept. 1990, pp. 641-658.

# Absolute and convective instability of a compressible jet (APPENDIX C)

Z. W. Zhou and S. P. Lin

Department of Mechanical and Aeronautical Engineering, Clarkson University, Potsdam, New York 13699

(Received 19 August 1991; accepted 21 October 1991)

The absolute and convective instability of a jet of an inviscid compressible fluid emanating into another inviscid compressible fluid is investigated. It is shown that the compressibility of the ambient fluid, as well as the surface tension, tends to promote absolute instability. The absolute instability can be reduced to the convective one by reducing the surface tension and/or increasing the compressibility of the jet fluid, depending on the flow parameters.

## I. INTRODUCTION

The capillary instability of an infinitely long liquid jet with respect to temporally growing disturbances was analyzed by Rayleigh.<sup>1</sup> Keller *et al.*<sup>2</sup> examined the capillary instability of a semi-infinite liquid jet with respect to spatially growing disturbances. They found that the temporal and spatial disturbances are analytically related if the Weber number is sufficiently small. When the Weber number is sufficiently large, they also found faster growing spatially amplifying disturbances that are unrelated to the Rayleigh mode of disturbances. Leib and Goldstein<sup>3</sup> showed that the new mode found by Keller *et al.* actually cannot be reached by a given initially infinitesimal disturbance in the sense of Briggs<sup>4</sup> and Bers.<sup>5</sup> Using the dispersion equation obtained by Chandrasekhar,<sup>6</sup> Leib and Goldstein<sup>7</sup> obtained the critical Weber number above which an incompressible viscous jet is absolutely unstable and below which it is convectively unstable as a function of the Reynolds number. It should be pointed out that the Weber number defined by Leib and Goldstein is the inverse of that used in this work. Lin and Lian<sup>8</sup> showed that absolute instability is enhanced by the presence of ambient fluid in a sense that it lowers the critical Weber number. They proposed that absolute instability corresponds physically to the dripping mode of instability. However, Tam and Hu<sup>9</sup> did not find absolute instability in a compressible jet emanating at high supersonic speeds into another compressible fluid. They found only convective instability. It appears that the compressibility may have a significant effect on the onset of absolute instability. However, while Tam and Hu considered only the case of a high supersonic jet without surface tension, the previous workers neglected the effect of compressibility. Thus the coupled effects of surface tension and compressibility remain unclear. These effects are very important in many practical applications involving a high-speed liquid jet emanating into a gas media. For example, the fuel jet in certain internal combustion engines may reach transonic and even supersonic speeds. Here, we investigate the effect of compressibility on the instability of a liquid jet emanating at subsonic as well as supersonic speeds into an ambient fluid.

## II. STABILITY ANALYSIS

Consider the onset of instability of a jet of inviscid compressible fluid emanating from a circular cylindrical nozzle

of radius  $a$  into an unbounded inviscid compressible fluid. The conservation equations of momentum, mass, energy, and the equation of state are, respectively,

$$\rho_i(\partial_t + \mathbf{V}_i \cdot \nabla) \mathbf{V}_i = -\nabla P_i, \quad (1)$$

$$\partial_t \rho_i + \nabla \cdot (\rho_i \mathbf{V}_i) = 0, \quad (2)$$

$$(\partial_t + \mathbf{V}_i \cdot \nabla) e_i - P_i(\partial_t + \mathbf{V}_i \cdot \nabla)(\rho_i^{-1}) = 0, \quad (3)$$

and

$$P_i = P_i(\rho_i, T_i) \quad (i = 1, 2),$$

where the subscripts  $i = 1, 2$  denote, respectively, the jet fluid and the ambient fluid,  $\rho$  is density,  $t$  is time,  $\mathbf{V}$  is the velocity vector,  $P$  is the dynamic pressure,  $e$  is the internal energy per unit mass, and  $T$  is temperature. Note that the flow is assumed to be adiabatic. The basic state that satisfies Eqs. (1) and (2) exactly in the absence of gravity is given by

$$\mathbf{V}_1 = (\bar{U}_1, \bar{V}_1, \bar{W}_1) = (0, 0, W_0),$$

$$\bar{\rho}_1 = \text{const}, \quad \bar{P}_1 = \text{const}, \quad (0 < R < a),$$

$$\mathbf{V}_2 = (\bar{U}_2, \bar{V}_2, \bar{W}_2) = (0, 0, 0), \quad \bar{\rho}_2 = \text{const},$$

$$\bar{P}_2 = \bar{P}_1 - S/a \quad (a < R < \infty),$$

where the overbar denotes the basic state quantities.  $U$ ,  $V$ , and  $W$  are, respectively, the radial, azimuthal, and axial components of velocity in the cylindrical coordinate system  $(R, \theta, Z)$ ,  $W_0$  is the constant jet speed, and  $S$  is the surface tension.  $Z$  is positive in the flow direction.

We investigate the stability of this basic state with respect to the disturbance defined by

$$\mathbf{V}_i = \bar{\mathbf{V}}_i + \mathbf{V}'_i, \quad \rho_i = \bar{\rho}_i + \rho'_i, \quad P_i = \bar{P}_i + P'_i, \quad r = a + d. \quad (3)$$

where primes are used to designate the perturbations of the variables. Substituting Eq. (3) into Eqs. (1) and (2), retaining only linear terms, we have

$$(\partial_t + \delta_{11} W_0 \partial_Z) \mathbf{V}'_1 = - (1/\bar{\rho}_1) \nabla P'_1, \quad (4)$$

$$(\partial_t + \delta_{11} W_0 \partial_Z) \rho'_1 = - \bar{\rho}_1 \nabla \cdot \mathbf{V}'_1, \quad (5)$$

where  $\delta_{11}$  is 1 or 0 depending on if  $i = 1$  or  $i \neq 1$ . Taking the divergence of (4) and then using Eq. (5), we have

$$(\partial_t + \delta_{11} W_0 \partial_Z)^2 \rho'_1 = \nabla^2 P'_1. \quad (6)$$

Assuming the change of pressure with respect to density is an isentropic process, expanding  $P_i[\rho, s(\rho_i, T_i)]$  about  $\bar{\rho}_i$ , we have  $P'_i = (\partial P_i / \partial \rho_i) \rho'_i = c_i^2 \rho'_i$ , where  $s$  is the entropy.

Thus Eq. (6) can be written as

$$(\partial_t + \delta_1, W_0 \partial_z)^2 P'_1 = c^2 \nabla^2 P'_1. \quad (7)$$

With respect to the moving fluids, (7) is the wave equation with the speed of propagation of pressure fluctuation  $c_1$ . The speed of sound  $c_1$  depends on the specific form of the equation of state and the fluid properties. It follows from the energy equation that

$$\frac{de_1}{dt} = P_1 \rho_1 - 2 \frac{dp_1}{dt},$$

$$\frac{dh_1}{dt} = \frac{d(e_1 + P_1/\rho_1)}{dt} = \rho_1 - \frac{dP_1}{dt},$$

where  $(d/dt)$  stands for the substantial derivative and  $h_1[T_1, s_1(\rho_1, T_1)]$  is the enthalpy. Hence, for the isentropic process of sound propagation,

$$\left( \frac{\partial P_1}{\partial \rho_1} \right)_s = \frac{P_1}{\rho_1} \cdot \left( \frac{\partial h_1}{\partial T_1} \right)_s.$$

For the ideal gas surrounding the jet  $P_2 = R\rho_2 T_2$ ,  $\partial h_2/\partial T_2 = C_p$ ,  $\partial e_2/\partial T_2 = C_v$ , and thus  $c_2 = (\gamma R T_2)^{1/2}$ , where  $R$  is the ideal gas constant, and  $\gamma = C_p/C_v$  is the ratio of the constant pressure specific heat  $C_p$  to the constant volume specific heat  $C_v$ . For the jet liquid,  $P_1[(\partial h_1/\partial T_1)/(\partial e_1/\partial T_1)] = K$  is the adiabatic bulk modulus of elasticity, and  $c_1 = (K/\rho_1)^{1/2}$ . The corresponding linearized boundary conditions for Eq. (7) at the interface  $r = a + d$  are the dynamic force balance

$$P'_1 - P'_2 = S(a^{-2} - a^{-2} \partial_{rr} - \partial_{zz})d \quad (8)$$

and the kinematic conditions

$$(\partial_t + \delta_1, W_0)^2 d = -\bar{\rho}_1^{-1} \partial_r P'_1. \quad (9)$$

Note that  $P'_1$  in Eqs. (8) and (9) are to be evaluated at  $r = a$ .

The normal mode solution of the differential system equations (7)–(9) will be sought in the form

$$\begin{bmatrix} P'_1 \\ P'_2 \\ d \end{bmatrix} = \begin{bmatrix} \bar{\rho}_1 W_0^2 p_1(r) \\ \bar{\rho}_1 W_0^2 p_2(r) \\ af \end{bmatrix} \cdot \exp[i(kz + n\theta - \omega\tau)], \quad (10)$$

where  $(r, z, f)$  and  $\tau$  are dimensionless variables defined by

$$(r, z, f) = (R, Z, d)a^{-1} \quad \text{and} \quad \tau = t(W_0/a);$$

and  $(k, n)$  and  $\omega$  are the dimensionless wave-number vector and wave frequency, respectively.

Substitution of Eq. (10) into Eqs. (7)–(9) yields the governing equation for the dimensionless perturbation pressure amplitudes

$$\{D^2 + r^{-1}D - [n^2 r^{-2} + k^2 - M_1^2(k - \omega)^2]\}p_1 = 0, \quad (11)$$

$$\{D^2 + r^{-1}D - [n^2 r^{-2} + k^2 - M^2 \omega^2]\}p_2 = 0, \quad (12)$$

and the corresponding boundary conditions at  $r = 1$ ,

$$p_2 - p_1 + W_c(k^2 + n^2 - 1)f = 0, \quad (13)$$

$$(k - \omega)^2 f - p'_1 = 0, \quad (14)$$

$$Q\omega^2 f - p'_2 = 0, \quad (15)$$

where primes denote differentiation with  $r$ , and

$$W_c = \frac{S}{\bar{\rho}_1 W_0^2 a}, \quad Q = \frac{\bar{\rho}_2}{\bar{\rho}_1}, \quad M_1 = \frac{W_0}{c_1}, \quad M = \frac{W_0}{c_2}.$$

Note that  $W_c$  is the Weber number,  $M_1$  is the Mach number of the jet and  $M$  is the Mach number of the ambient fluid with respect to a frame of reference moving with the jet at a speed  $W_0$ . The bounded solution of Eqs. (11) and (12) are

$$p_1 = AI_n(\lambda_1 r), \quad \lambda_1 = [k^2 - M_1^2(k - \omega)^2]^{1/2},$$

$$p_2 = BK_n(\lambda_2 r), \quad \lambda_2 = (k^2 - M^2 \omega^2)^{1/2},$$

where  $A$  and  $B$  are the integration constants and  $I_n$  and  $K_n$  are, respectively, the modified Bessel function of the first and second kinds. Substitution of these solutions into Eqs. (14) and (15) yields

$$A = (k - \omega)^2 f / I'_n(\lambda_1) \lambda_1,$$

$$B = Q\omega^2 f / K'_n(\lambda_2) \lambda_2,$$

where primes now denote the differentiation  $d/d(\lambda, r)$ . It follows from Eq. (13) that

$$\begin{aligned} D \equiv & (k - \omega)^2 I_n(\lambda_1) / \lambda_1 I'_n(\lambda_1) \\ & - Q\omega^2 K_n(\lambda_2) / \lambda_2 K'_n(\lambda_2) \\ & - W_c(k^2 + n^2 - 1) = 0. \end{aligned} \quad (16)$$

For a given set of four flow parameters  $W_c$ ,  $Q$ ,  $M_1$ , and  $M$ , this is the secular equation the solution of which gives the characteristic wave frequency  $\omega$  and the wave number  $k$ .

For the special case of an incompressible jet in a vacuum,  $Q = 0$ ,  $c_1 \rightarrow \infty$ ,  $c_2 \rightarrow 0$ , thus  $\lambda_1 \rightarrow k$ ,  $\lambda_2 \rightarrow \infty$  and Eq. (16) is reduced to, if  $\omega$  remains finite,

$$I_n(k)(k - \omega)^2 / I'_n(k) + k(1 - k^2 - n^2)W_c = 0. \quad (17)$$

This is the characteristic equation used by Keller *et al.*<sup>2</sup> and Leib and Goldstein<sup>3</sup> in their studies of the spatial instability of the Rayleigh jet. For the special case of an incompressible jet emanating into an incompressible fluid,  $c_1 \rightarrow \infty$ ,  $M, M_1 \rightarrow 0$ , thus  $\lambda_1 = \lambda_2 = k$ , and Eq. (16) is reduced to, if  $\omega$  remains finite,

$$\begin{aligned} (k - \omega)^2 I_n(k) / I'_n(k) - Q\omega^2 K_n(k) / K'_n(k) \\ - k(k^2 + n^2 - 1)W_c = 0. \end{aligned} \quad (18)$$

This equation agrees with Eq. (1) of Lin and Lian<sup>4</sup> when the Reynolds number of their equation is allowed to approach infinity and their  $\omega$  and  $k$  are, respectively, replaced by  $-i\omega$  and  $-k$ . This change of variable is necessary because of the different positive directions and the different definitions of the wave frequency that are used in these two papers. When the surface tension is put to zero, Eq. (18) reduces to the characteristic equation corresponding to that of Tam *et al.*<sup>5</sup> except their equation is in terms of the Hankel function and the Bessel function of the first kind. It is known that the axisymmetric disturbance grows the fastest in an incompressible jet in the absence<sup>2</sup> or presence<sup>10</sup> of the ambient fluid. Here, we assume that the same is true for a compressible jet. Hence we treat the case of  $n = 0$  in Eq. (16). Here, both  $\omega = \omega_r + i\omega_i$  and  $k = k_r + ik_i$  are complex. Their imaginary parts  $\omega_i$  and  $k_i$  give, respectively, the temporal and the spatial growth rates. Their real parts are the wave frequency and the wave number, respectively.

### III. RESULTS

The numerical accuracy, as well as the correctness of the computer program that solves Eq. (16), were ascertained by comparing some known results of published works<sup>3,8,10</sup> with our results for the corresponding special cases. These known results will not be reproduced here, however. Figure 1 delineates the solution curves of (16) for the case of an incompressible liquid jet emanating into a gas of a density that is 1.3% of the liquid density. This density ratio corresponds to a water-air system under 1 atm. The Mach number of the gas relative to the reference frame moving with the liquid jet is supersonic. Note the existence of the two saddle points  $C'$  and  $C$ , respectively, associating with the two sets of zero-temporal growth-rate curves ( $A', B'$ ) and ( $A, B$ ). The constant  $\omega$ , curves initiate from the upper or lower  $k_x - k_z$  plane with finite positive values of  $\omega$ . The values of  $\omega$ , decrease toward zero before they reach ( $A', B'$ ) or ( $A, B$ ), the curves set of  $\omega = 0$ . Here,  $A$  and  $A'$  will be called the downstream branches, because  $\omega$ , increases with  $k_x$  near these curves and thus the group velocities of the disturbances are in the downstream direction. Similarly, the disturbances corresponding to the upstream branches  $B$  and  $B'$  have upstream propagating group velocities. Observe that the saddle point  $C$  has the value of  $\omega$ , lying between 0.9603 and 0.9650. The value of  $\omega$ , at  $C'$  must be between 0.7443 and 0.7516. At these saddle points  $D = \partial D / \partial k_x = 0$  and the group velocity is zero. Moreover,  $\omega_x > 0$  at these saddle points. The appearances of the saddle pinch point signifies that the Fourier integral representation of the disturbance has encountered a singularity along its path of integration. Hence the integration path cannot be analytically deformed long before  $\omega_x = 0$  is reached. Consequently, the disturbance will grow both temporally and spatially at the onset of absolute instability

as explained by Briggs<sup>7</sup> and Bers.<sup>8</sup> Note that  $C'$  lies in the region of  $k_x < 1$  but  $C$  lies in the region of  $k_x > 1$ . The absolute instabilities associated with  $C'$  and  $C$  will be termed the first and the second kind, respectively. The physical significance of this will be explained shortly. When  $M$  is reduced to subsonic values such that  $0 < M < 1$ , with the rest of the parameters specified in Fig. 1 fixed, we found that the saddle points  $C'$  and  $C$  move to new positions but remain in the respective regions of  $k_x < 1$  and  $k_x > 1$ . The situation remains the same even when  $M = 0$ . However, Lin and Lian<sup>8</sup> found that, when  $M_1 = M = 0$ , there is only one saddle point belonging to the first kind. The existence of the second saddle point in this work as  $M = 0$  therefore constitutes an apparent inconsistency with the work of Lin and Lian.<sup>8</sup> It turns out that Eq. (18) used by Lin and Lian and Eq. (17) used by Leib and Goldstein are both singular limits of Eq. (16) as  $M_1$  and  $M = 0$ . The solution that gives rise to the second saddle point cannot be recovered from Eqs. (17) and (18), because  $M_1 \omega$  and  $M \omega$  remain finite as  $M_1$  and  $M = 0$  in Eq. (16).

Lin and Lian also showed that the absolute instability can be reduced to convective instability by reducing the Weber number if both the jet and the ambient fluid are incompressible. This is not the case when the ambient fluid is compressible with the flow parameters specified in Fig. 1. The values of flow parameters in Fig. 2 remain the same as those in Fig. 1, except that  $W_e$  is reduced from 1.5 to 0.1. As can be seen from these figures, the saddle point  $C'$  can indeed be eliminated by reducing  $W_e$ , as in the incompressible case, but the new saddle point  $C$  remains. Even when  $W_e = 0$ , the new saddle point still remains. With  $M = 1.74$ ,  $W_e = O(10^{-5})$  for most common liquids, and thus the absolute instability of the second kind should be easily observable. The mechanisms of the two kinds of absolute instabilities are different. A discussion on these two different mechanisms will be presented near the end of this section.

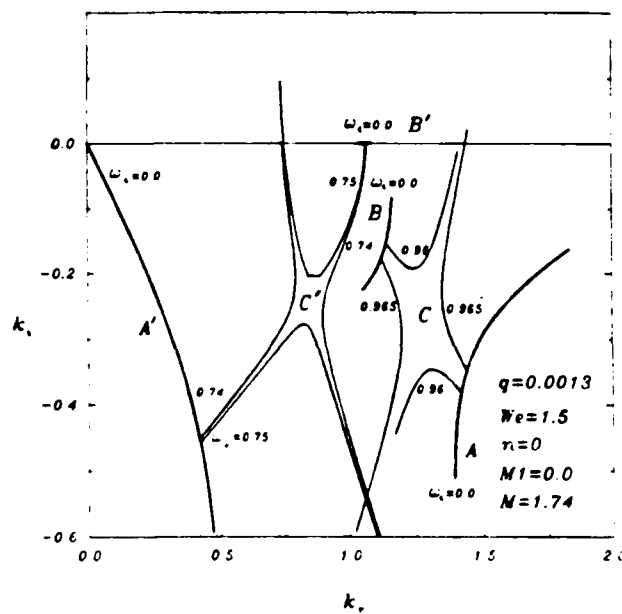


FIG. 1. Absolute instability of incompressible jet with two saddle points

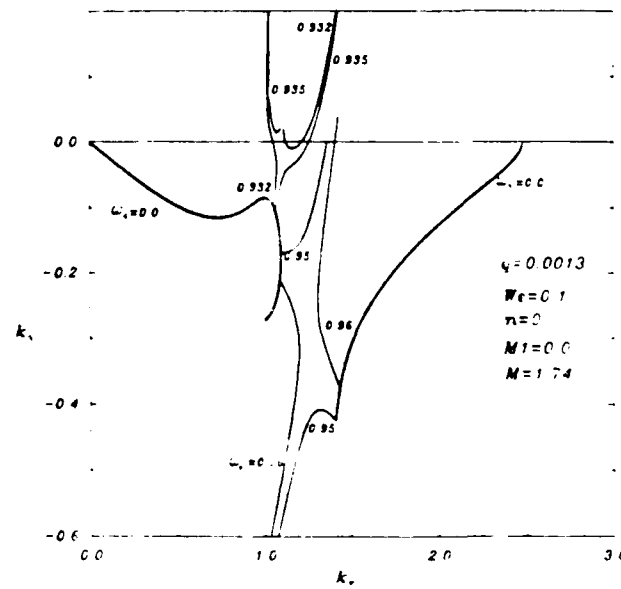


FIG. 2. Suppression of the saddle point of the first kind in an incompressible jet

An extensive computation over a wide range of flow parameters shows that the absolute instability of the second kind can be suppressed by increasing the compressibility of the jet while the rest of the parameters are kept constant. Figures 3 and 4 provide such an example. For the flow parameters specified in Fig. 3, there are both kinds of saddle points. The saddle point of the second kind is eliminated in Fig. 4 by further increasing  $M_1$  to 0.52 from 0.51 in Fig. 3. However, fairly extensive computations show that the elimination of the saddle point of the second kind can be achieved only when  $M > 1$ . Note that the saddle point of the first kind still remains. The saddle point of the first kind persists even if one continues to increase  $M_1$  to a high supersonic value. This is demonstrated in Fig. 5. It should be pointed out that the amplification curve for the convectively unstable second mode appearing in Fig. 4 still remains when the flow parameters are changed to that of Fig. 5. It does not appear in Fig. 5, because it lies outside of the right edge of this figure.

When the surface tension of the jet characterized in Fig. 5 is reduced such that  $W_e$  is decreased from 0.8 to 0.6, the absolute instability is completely eliminated, and the jet becomes convectively unstable as shown in Fig. 6. The  $\omega_r = 0$  curve in Fig. 6 can be approached along constant  $\omega_r$  curves originated with  $\omega_r > 0$  from the upper  $k_r, -k_r$  plane.<sup>4,5</sup> Hence the curve  $\omega_r = 0$  in Fig. 6 gives the spatial amplification rate of the convectively unstable disturbances. Further reduction of  $W_e$  does not reintroduce the absolute instability. This is consistent with the results of Tam and Hu who found no absolute instability at high supersonic speeds of the jet without surface tension.

In order to understand the physical mechanisms of the absolute instability and of convective instability, we obtain the eigenvectors  $(p_1, p_2, f)$  corresponding to the eigenvalues near the two types of saddle points. The pressure exerted by the jet on its interface corresponding to the absolute instabil-

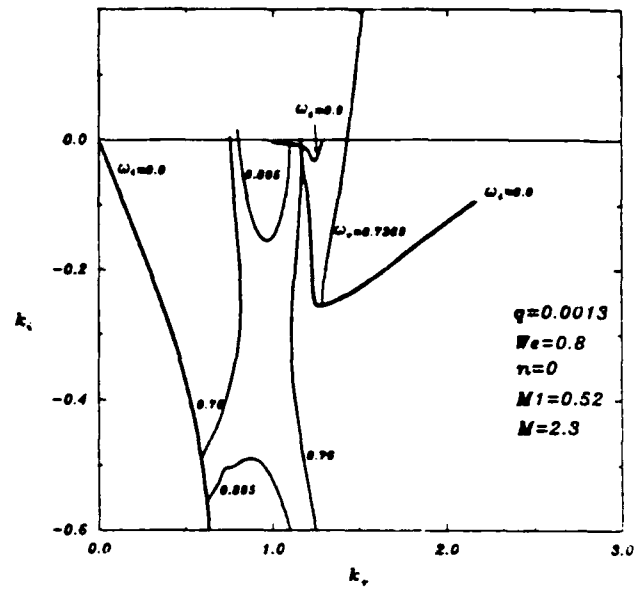


FIG. 4. Suppression of the saddle point of the second kind.

ity of the first kind depicted in Fig. 4 is plotted in Fig. 7, together with  $p_2$  and the spatially growing interfacial displacement  $f$ . The pressure distribution is nearly 180° out of phase with the displacement. Thus  $(p_1 - p_2)$  stabilizes the jet by acting against necking and bulging, respectively, at the wave troughs and wave peaks. On the contrary, the surface tension force tends to facilitate capillary pinching along the radial direction. This can be seen from Eq. (16). Note that the  $-k^2 W_e$  and the  $W_e$  terms in Eq. (16) have opposite signs. It is seen from Eq. (8) that the  $-k^2 W_e$  term arises from the interfacial curvature along the axial direction, and the  $W_e$  term arises from the curvature along the circumferential direction. While the surface tension uses the curvature

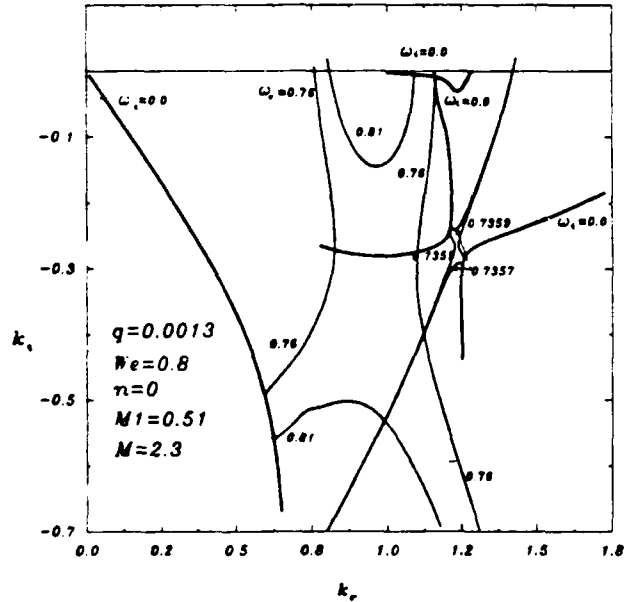


FIG. 3. Absolute instability of a supersonic jet

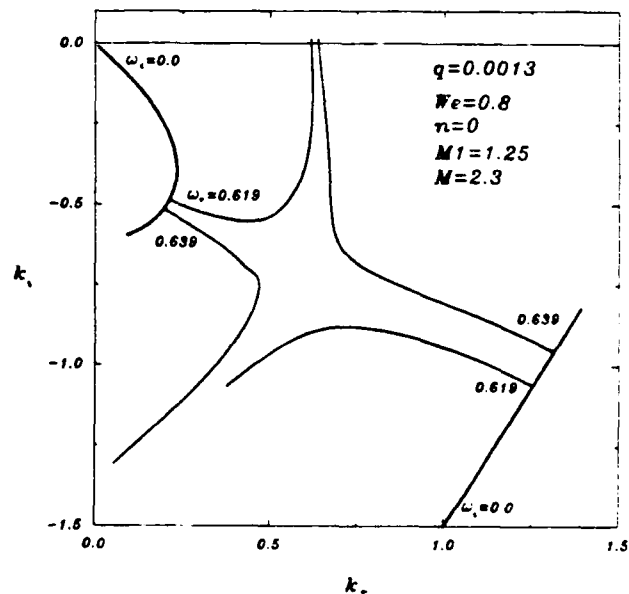


FIG. 5. Absolute instability of supersonic jet

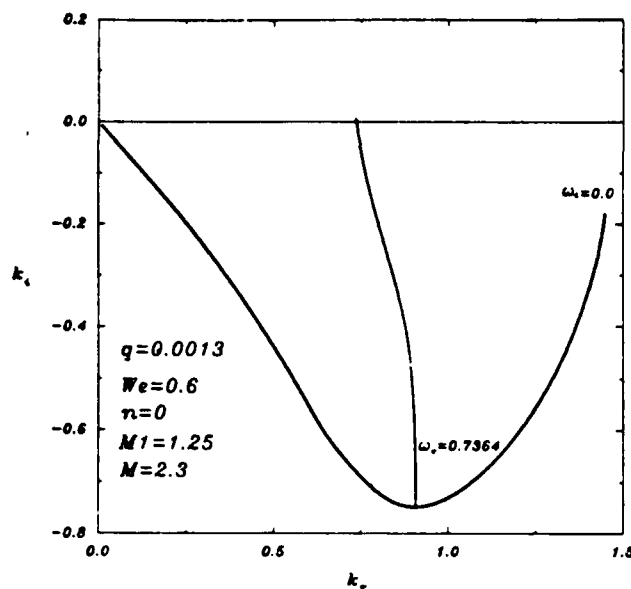


FIG. 6. Convective instability of supersonic jet.

along the axial direction to restore the interface to its unperturbed position, it exploits the curvature along the circumferential direction to pinch the jet. For the absolute instability of the first kind  $k < 1$  near the saddle point, and thus the  $-k^2 W_z$  term is dominated by the  $W_z$  term. Hence the jet becomes unstable due to the capillary pinching. For the absolute instability associated with the saddle point of the second kind,  $k > 1$  and thus surface tension is a stabilizing force. The instability must be caused by the unfavorable pressure distribution. The pressure distribution along the interface corresponding to the absolute instability of the second kind depicted in Fig. 2 is presented in Fig. 8. Note that  $(p_1 - p_2)$  in Fig. 8 tends to steepen the slope of the wave front. Appar-

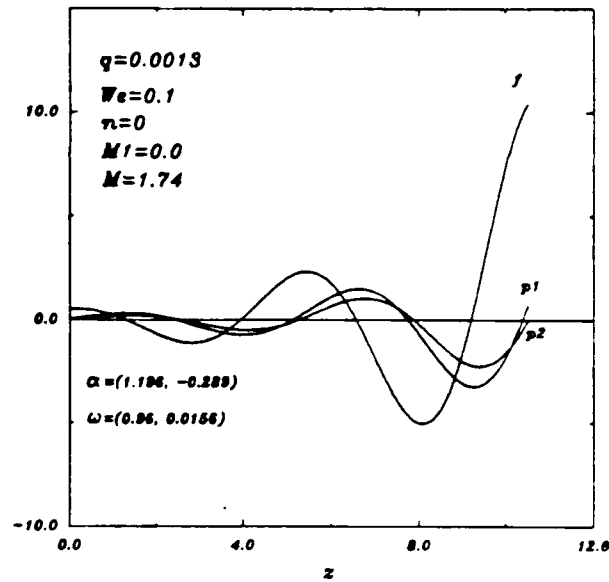


FIG. 8. Absolute instability of the second kind.

ently, the stabilizing surface tension is not sufficiently large to overcome the pressure force.

It is seen from Fig. 7 that the pressure in the jet opposes the first kind of absolute instability. The mean pressure in the jet is inversely proportional to  $Q$ . It follows that a larger value of  $Q$  may promote the absolute instability of the first kind. Figures 6 and 9 demonstrate this point clearly. The convective instability depicted in Fig. 6 changes over to the absolute instability portrayed in Fig. 9 simply because of the increase in  $Q$  from 0.0013 to 0.08. It was also found that the absolute instability of the second kind has the same dependence on  $Q$ .

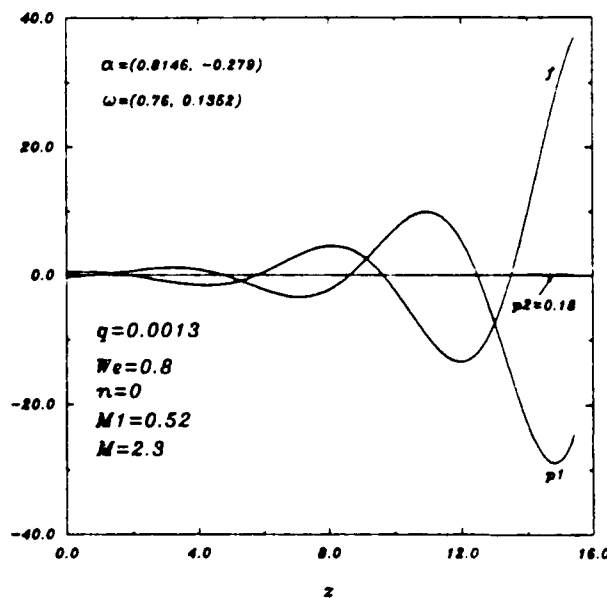


FIG. 7. Absolute instability of the first kind

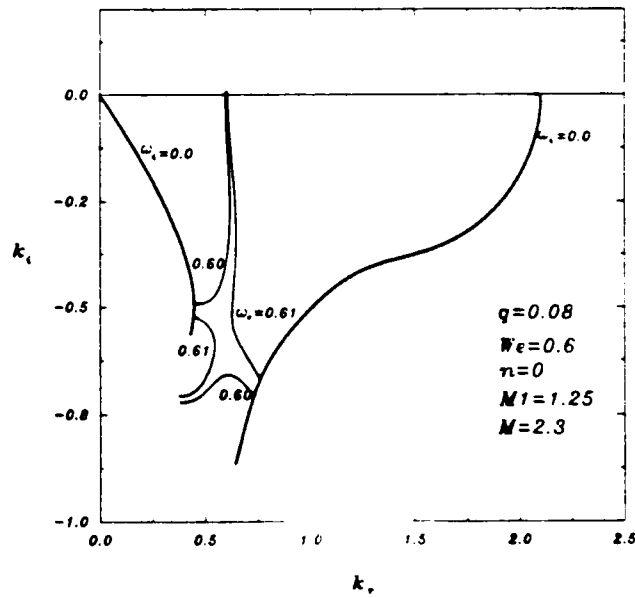


FIG. 9. Absolute instability of the first kind

#### IV. CONCLUSION

In the four-dimensional hyperspace spanned by  $W_c$ ,  $Q$ ,  $M_1$ , and  $M$ , there exists a surface that separates the space into regions of convective and absolute instabilities. A simple delineation of this surface cannot be made without a complete mapping of this parameter space. The stability characteristics of a compressible jet encountered in any specific applications have to be determined from the solutions of Eq. (16) for the specific flow parameters encountered. However, based on the fairly extensive computation carried out by us, we may make the following points. Two kinds of absolute instability were found. The first kind is caused by the capillary pinching, but the second is due to the interfacial pressure fluctuation alone. A reduction of surface tension may eliminate the first kind, but cannot remove the second kind. The compressibility of the jet may be used to elevate the absolute instability of the second kind if  $M > 1$ . The compressibility of the ambient fluid promotes the absolute instability. The absolute instability of both kinds can be removed simultaneously by use of lower surface tension and larger jet compressibility. Whether the instability of a jet is absolute or convective depends on the dispersion property dictated by the particular parameter range encountered by the jet. When the spatially growing disturbance is capable of escaping with a finite group velocity from a point in space the jet is convectively unstable, otherwise it is absolutely unstable. As far as the physical mechanism is concerned, both convective and absolute instabilities are either due to capillary pinching or the pressure fluctuation.

#### ACKNOWLEDGMENTS

This work was supported in part by Grants No. DAAL03-89-K-0179 of ARO, No. MSM-8817372 of NSF, and a New York State Science Foundation Grant. The computation was carried out with the computer facility at Clarkson University and with the Cornell National Computer facility, which is funded by the NSF, the State of New York, and IBM Corporation.

- <sup>1</sup>Lord Rayleigh, "On the instability of jets," *Proc. London Math. Soc.* **10**, 4 (1879).
- <sup>2</sup>J. B. Keller, S. I. Rubinow, and Y. O. Tu, "Spatial instability of a jet," *Phys. Fluids* **16**, 2052 (1973).
- <sup>3</sup>S. J. Leib and M. E. Goldstein, "The generation of capillary instabilities of a liquid jet," *J. Fluid Mech.* **168**, 479 (1986).
- <sup>4</sup>R. J. Briggs, *Electron Stream Interaction with Plasmas* (MIT Press, Cambridge, MA, 1964).
- <sup>5</sup>A. Bers, *Handbook of Plasma Physics* (North-Holland, Amsterdam, 1983), Vol. 1, pp. 452-516.
- <sup>6</sup>S. Chandrasekhar, *Hydrodynamic and Hydromagnetic Stability* (Dover, New York, 1961).
- <sup>7</sup>S. J. Leib and M. E. Goldstein, "Convective and absolute instability of a viscous liquid jet," *Phys. Fluids* **29**, 952 (1986).
- <sup>8</sup>S. P. Lin and Z. W. Lian, "Absolute instability of a liquid jet in a gas," *Phys. Fluids A* **1**, 490 (1989).
- <sup>9</sup>C. K. W. Tam and Q. Hu, "On the three families of instability waves of high speed jets," *J. Fluid Mech.* **201**, 447 (1989).
- <sup>10</sup>Z. W. Lian and S. P. Lin, "Breakup of a liquid jet in a swirling gas," *Phys. Fluids A* **2**, 2134 (1990).

# Absolute and convective instability of a viscous liquid jet surrounded by a viscous gas in a vertical pipe (APPENDIX D)

S. P. Lin and Z. W. Lian

Department of Mechanical and Aeronautical Engineering, Clarkson University,  
Potsdam, New York 13699

(Received 10 August 1992; accepted 21 October 1992)

The absolute and convective instability of a viscous liquid jet emanating into a viscous gas in a vertical pipe is analyzed in a parameter space spanned by the Reynolds number, the Froude number, the Weber number, the viscosity ratio, the density ratio, and the diameter ratio. The numerical results of the analysis are used to demonstrate that reduction in gravity tends to enhance the Rayleigh mode of convective instability which leads to the breakup of a liquid jet into drops of diameters comparable with the jet diameter. On the contrary, the Taylor mode of convective instability that leads to atomization is retarded at reduced gravity. The Rayleigh mode becomes absolutely unstable when the Reynolds number exceeds a critical value for a given set of the rest of the relevant parameters. The domain of absolute instability is significantly enlarged when the effect of gas viscosity is not neglected.

The stability of core-annular flows has been investigated extensively in the context of lubricated pipelining<sup>1</sup> as well as in the context of liquid jet atomization.<sup>2</sup> Temporally growing disturbances were considered in the published works. In the present work, we investigate the stability of core-annular flow with respect to spatially growing disturbances. Spatially growing disturbances are especially relevant to the atomization process that utilizes the amplification of disturbances as they are convected downstream to generate small droplets. The atomization process must be carried out outside of the Rayleigh regime<sup>3</sup> of jet breakup by capillary pinching. It must also avoid absolute instability.<sup>4,5</sup> The critical Weber number above which the flow is absolutely unstable is obtained as a function of the Reynolds number for given sets of the rest of relevant flow parameters. Outside of the region of absolute instability in the parameter space, it is shown that there are two physically distinct modes of convective instability.

Consider the stability of a cylindrical liquid jet of density  $\rho_1$  flowing vertically downward in the direction of gravitational acceleration  $g$ . The jet is surrounded by a gas of density  $\rho_2$  occupying the annular space between the jet and the inner wall of a vertical pipe of radius  $R_2$ . The liquid and gas flows have the same pressure gradient in the jet flow direction. Hence the pressure drop across the liquid-gas interface at any cross section is constant along the axial direction. This pressure difference is balanced exactly by the surface tension force per unit surface area of the liquid cylinder of constant radius  $R_1$ , which is also the radius of curvature. The velocity distribution of the basic flow that satisfies exactly the Navier-Stokes equations is given by Eq. (1) of Lin and Ibrahim.<sup>2</sup> The linear stability analysis of this basic flow with respect to the normal mode disturbance yields the characteristic equation given by Eq. (21) of Lin and Ibrahim.<sup>2</sup> The normal mode disturbances involve an exponential factor  $\exp(ikz + \omega t)$ , where  $t$  is time and  $z$  is the axial distance measured in the opposite direc-

tion of the liquid flow. The wave number  $k$  was treated as real in the previous analysis<sup>2</sup> of temporally growing disturbances. In this work, both  $k$  and  $\omega$  are complex, i.e.,  $k = k_r + ik_i$  and  $\omega = \omega_r + i\omega_i$ . Hence  $k_r > 0$  gives the spatial growth rate of disturbances convected as a group in the downstream direction. Here,  $\omega_r > 0$  gives the temporal growth rate of unstable disturbances,  $k_r$  is the real wave number that is inversely proportional to the wavelength, and  $\omega_i$  is the natural frequency of oscillation of the normal mode disturbance. The group velocity of the disturbance is given by  $-\partial\omega_r/\partial k_r$ .

To determine the spatial amplification rate of convectively unstable disturbances for a given set of parameters, we put  $\omega_i = 0$  and assign different values to  $\omega_r$  in the characteristic equation. Then,  $k_r$  and  $k_i$  are solved from the real and imaginary parts of the characteristic equation by use of a modified Powell's hybrid method with the subroutines CGEDI and DNSQ in the SLATEC library. The set of points  $(k_r, k_i)$  for various values of  $\omega_r$  determine the spatial amplification curve  $\omega_r = 0$ . The number of terms retained in the series solutions are varied and the resulting characteristic equations are solved for the eigenvalues. The characteristic values corresponding to different orders of the characteristic determinant are compared to ascertain the desired numerical accuracy. It is found that it is sufficient to retain only three and five terms, respectively, in the liquid and gas phases for four decimal point accuracy for the given parameters.

The numerical accuracy, as well as the correctness of the computer program that solves the characteristic equation, were ascertained by comparing some known results of published works<sup>4,5</sup> with our results for the corresponding special cases. These known results will not be reproduced here, however. The relevant parameters are the Weber, Reynolds, and Froude numbers, the density, viscosity and radius ratios defined, respectively, by  $We = S/\rho_1 W_0^2 R_1$ ,  $Re = \rho_1 W_0 R_1 / \mu_1$ ,  $Fr = W_0^2 / g R_1$ ,  $\rho_2 / \rho_1$ ,  $\mu_2 / \mu_1$ ,  $R_2 / R_1$ , where  $W_0$

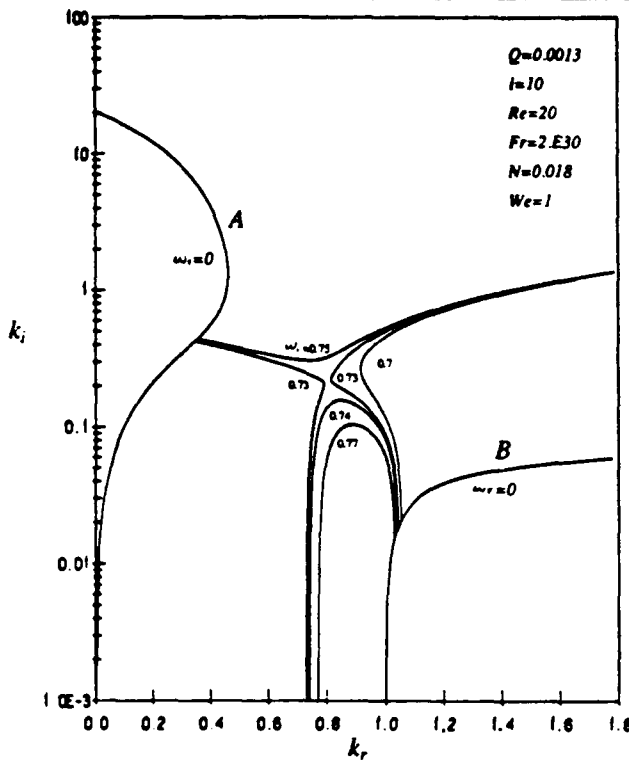


FIG. 1. The existence of the absolute instability.

is the maximum velocity in the liquid jet,  $\mu_1$  and  $\mu_2$  are, respectively, the dynamic viscosities of the jet liquid and the surrounding gas.

The results on absolute instability that were not found in the temporal analyses will be reported first. For a sufficiently high Weber number, given the rest of relevant parameters, we obtain two branches of spatial amplification curves  $\omega_r=0$ . An example is shown in Fig. 1, where the two branches are designated with A and B. The values of  $\omega_r$  increase along A and decrease along B. Thus the group velocities of disturbances associated with branches A and B propagate, respectively, in the downstream and upstream directions. Notice the appearance of a saddle point in this figure. The constant  $\omega_r$  curves initiated from the upper or lower  $k_r$ - $k_i$  plane with finite positive values of  $\omega_r$ , delineated the manner with which the saddle point is formed. Observe that the saddle point has the value of  $\omega_r$  lying between 0.73 and 0.74. At the saddle point  $D=\partial D/\partial k_r=0$ , where  $D$  stands for the characteristic determinant, i.e., the left side of the characteristic equation. At the saddle point, the group velocity is zero, and  $\omega_r>0$ . The appearance of the saddle point signifies that the Fourier integral representation of the disturbance has encountered a pinch point singularity along its path of integration. Hence the integration path cannot be analytically deformed long before  $\omega_r=0$  is reached. Consequently, the disturbances will grow both temporally and spatially at the onset of absolute instability as explained by Briggs and Bers.<sup>6</sup> When the value of  $We$  is gradually decreased with the rest of the parameters in Fig. 1 kept constant, the saddle point moves gradually toward the downstream branch and eventually disappears. Thus

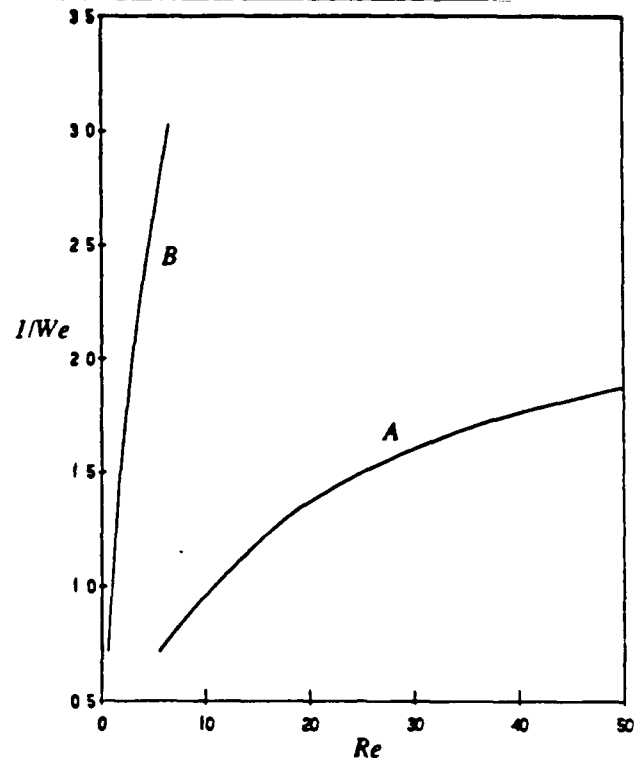


FIG. 2. Critical Weber number of absolute instability.

there exists a critical Weber number above which the flow is absolutely unstable, and below which it is convectively unstable for a given set of parameters. The critical Weber number is found to be only weakly dependent on  $Fr$ ,  $N$ , and  $l$ . The critical Reynolds number as a function of  $We$  for  $Q=0.0013$ ,  $N=0.018$ ,  $Fr=1000$ , and  $l=10$  is depicted as curve B in Fig. 2. Curve A in this figure is the corresponding curve for the case of inviscid surrounding gas of infinite extent,<sup>5</sup> i.e., for the case of  $N=0$ ,  $l=\infty$ , and  $Q=0.0013$ . It is observed that the domain of absolute instability is significantly enlarged.

Figure 3 delineates the dependence of the spatial amplification curves,  $\omega_r=0$ , on the Weber number for the given set of parameters specified in the figure. This set of parameters falls inside the region of convective instability. All of the amplification curves can be reached along constant  $\omega_r$  curves initiating from the lower  $k_r$ - $k_i$  plane with finite positive values of  $\omega_r$ . Moreover, the group velocity of the disturbance,  $-\partial\omega_r/\partial k_r$ , is negative along each of the amplification curves. Hence these curves give the spatial amplification rate of the disturbances as they are swept downstream as a group. It is seen that the amplification rate increases with  $We$ , indicating that surface tension is a source of the convective instability. It is also seen that the wavelength corresponding to the most amplified disturbance is of the same order of magnitude as the jet radius, as is encountered in the Rayleigh jet. These results are qualitatively the same as those found in the temporal theory.<sup>2</sup> Note that the values of  $N$  and  $Q$  used in Fig. 3 correspond to a water jet in air at room temperature under one atmospheric pressure. The effects of the rest of the parameters

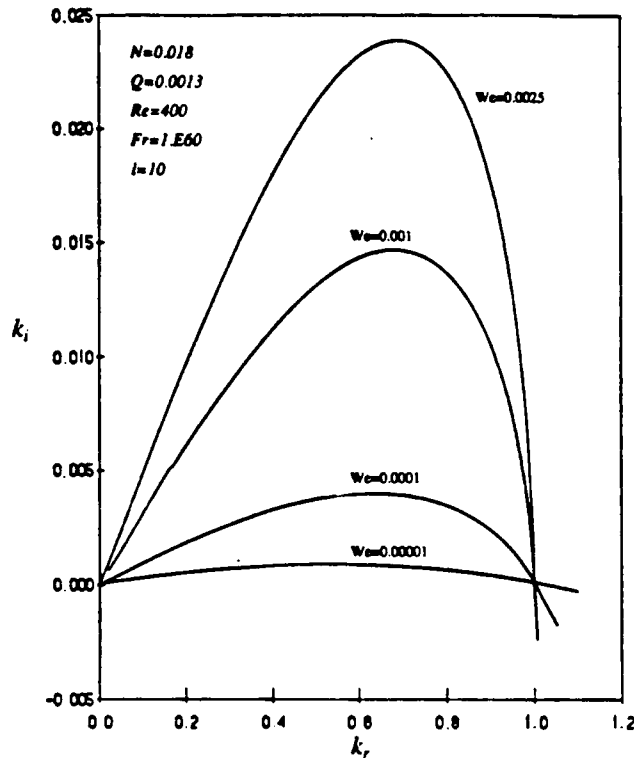


FIG. 3. The Rayleigh mode convective instability.

on the convectively unstable disturbances remain qualitatively the same as those for the case of temporally growing disturbances. Therefore they will not be explained here. However, the effect of the Weber number of Taylor mode instability at microgravity will be mentioned here, since it was not pointed out previously. When the parameters in Fig. 3 are kept the same except the Froude number is reduced to 2000, the jet becomes unstable with respect to the Taylor mode. Contrary to the situation in Fig. 3, the amplification rate decreases with  $We$ , indicating that surface tension force is not the source of instability. The other noticeable feature is that the wavelength corresponding to the most amplified disturbance for this set of parameters is one order of magnitude smaller than the jet diameter, as is frequently observed in atomization processes. The physical mechanism of atomization was shown<sup>3</sup> to be the interfacial pressure fluctuation for the case of a viscous jet in an inviscid gas. Here, with the gas viscosity included, the interfacial pressure fluctuation is supplemented by the viscous stress fluctuation to enhance the instability. This enhancement can be expected to be significant when the change of

velocity gradient across the interface becomes large. The change of the velocity gradient increases with the decrease in the value of  $Fr$  as can be seen from the expressions of the basic state velocity distribution. This is a physical explanation of why the Rayleigh mode<sup>3</sup> of instability depicted in Fig. 3 changes to Taylor's<sup>3</sup> mode of atomization instability at reduced gravity.

The liquid core-gas annular flow of two viscous fluids is shown to be capable of exhibiting either absolute or convective instability depending on the specific values of flow parameters involved. The critical Weber number below which the flow is convectively unstable and above which the flow is absolutely unstable, is obtained as a function of the Reynolds number for the given remaining parameters. The gravity is found to have little effect on the absolute/convective nature of instability. There are two modes of convective instability: the Rayleigh mode of convective instability caused by capillary pinching and the Taylor mode of atomization caused by interfacial stress fluctuation. The Taylor mode instability is shown to change over to the Rayleigh mode when the Froude number is increased beyond a certain value with the rest of flow parameters fixed. The practical implication of this is that the atomization processes widely used on earth in a given parameter range may fail to produce droplets smaller than the jet thickness at microgravity. In order to recover the atomization process at microgravity, one may reduce the width of the annular gas layer to increase the interfacial stress.

#### ACKNOWLEDGMENTS

This work was supported in part by Grants No. DAAL 03-89-K-0179 of ARO, No. MSM-8817372 of NSF, and No. NAG3-1402 of NASA. The computation was carried out with the computer facility at Clarkson University and with the Cornell National Computer facility, which is funded by NSF, the State of New York, and the IBM Corporation.

<sup>1</sup>K. Chen and D. D. Joseph, "Lubricated pipelining Stability of core-annular flow. Part 4. Ginzburg-Landau equations," *J. Fluid Mech.* **227**, 587 (1991).

<sup>2</sup>S. P. Lin and E. A. Ibrahim, "Instability of a viscous liquid jet surrounded by a viscous gas in a vertical pipe," *J. Fluid Mech.* **218**, 641 (1991).

<sup>3</sup>S. P. Lin and B. Creighton, "Energy budget in atomization," *J. Aerosol Sci. Technol.* **12**, 630 (1990).

<sup>4</sup>S. J. Leib and M. E. Goldstein, "Convective and absolute instability of a viscous liquid jet," *Phys. Fluids* **29**, 952 (1986).

<sup>5</sup>S. P. Lin and Z. W. Lian, "Absolute instability of a liquid jet in a gas," *Phys. Fluids A* **1**, 490 (1989).

<sup>6</sup>A. Bers, *Handbook of Plasma Physics* (North-Holland, Amsterdam, 1983), Vol. 1, pp. 452-516.

CLARKSON UNIVERSITY

200334  
THESIS  
C'112  
C.2

(APPENDIX E )

# EXPERIMENTAL STUDY OF AN INTERMITTENT SPRAY USING SEVERAL NOZZLE PRESSURE WAVEFORMS

A Thesis  
by

## Vincent F. Cook

Department of Mechanical and Aeronautical Engineering

Submitted in partial fulfillment of the requirements for the degree of

**Master of Science**

(Mechanical Engineering)

January 18, 1993

Accepted by the Graduate School  
Dean R. M. Cook  
Date 1/29/93

POTSDAM, NEW YORK

The undersigned have examined the thesis entitled

**EXPERIMENTAL STUDY OF AN  
INTERMITTENT SPRAY USING SEVERAL  
NOZZLE PRESSURE WAVEFORMS**

presented by Vincent Cook, a candidate for the degree of Master of Science, and hereby certify that it is  
worthy of acceptance.

27 January, 1993  
Date

S. P. Lin

Advisor, Professor S. P. Lin

Daniel T. Valentine  
Professor Daniel T. Valentine

Mark Glauser  
Professor Mark Glauser

# Table of Contents

<b>Chapter 1 Introduction</b>	<b>1</b>
<b>Chapter 2 Experimental Setup and Procedure</b>	<b>5</b>
<b>2.1 EXPERIMENTAL SETUP</b>	<b>5</b>
<b>2.2 PHYSICAL PROPERTIES OF THE TEST FLUID</b>	<b>9</b>
<b>2.3 EXPERIMENTAL PROCEDURE</b>	<b>9</b>
<b>2.4 SAMPLE LOCATIONS</b>	<b>13</b>
<b>2.5 STUDY OF THE NOZZLE PRESSURE WAVEFORMS USED</b>	<b>13</b>
<b>Chapter 3 Results</b>	<b>17</b>
<b>3.0 GENERAL</b>	<b>17</b>
<b>3.1 TIME INTEGRATED DISTRIBUTION OF DROP SIZE AND VELOCITY</b>	<b>17</b>
<b>3.2 TEMPORALLY AND SPATIALLY INTEGRATED DROP SIZE DISTRIBUTION</b>	<b>22</b>
<b>3.3 TIME EVOLUTION OF DROP SIZE AND VELOCITY DISTRIBUTIONS</b>	<b>23</b>
<b>3.4 CONTINUOUS JETS</b>	<b>24</b>
<b>Chapter 4 Discussion</b>	<b>35</b>
<b>4.1 OBSERVED TRENDS</b>	<b>35</b>
<b>4.2 CORRELATION TO CONTINUOUS SPRAY</b>	<b>41</b>
<b>4.3 SPECIAL OBSERVATION</b>	<b>41</b>
<b>Chapter 5 Conclusion</b>	<b>43</b>
<b>References</b>	<b>46</b>
<b>Appendix A Computer Programs</b>	<b>48</b>
<b>A.1 ANALYSIS OF DATA FOR LOCAL PRESSURE PEAKS</b>	<b>48</b>
<b>A.2 TABULATING DROP SIZE AND VELOCITY DATA</b>	<b>50</b>
<b>A.3 ANALYSIS OF PRESSURE WAVEFORMS</b>	<b>53</b>
<b>A.4 CALCULATION OF CORRECTION FACTORS</b>	<b>54</b>

## Abstract

Current fuel injection design relies upon empirical studies to optimize injector technology. The fundamental understanding of the relationship between the fuel pressure input to an injector nozzle and the resulting spray has remained vague. An experimental study was undertaken to measure the spray characteristics of a diesel spray resulting from various dynamic pressure inputs to a nozzle.

An intermittent liquid spray was created by applying successive cycles of a pressure waveform to a plain hole nozzle. Drop sizes and their temporal relationship to the pressure waveform were recorded at various locations downstream from the nozzle. The results are presented for several nozzle pressure waveforms.

# List of Figures

<b>Figure 1.1</b>	Engine performance trade-offs in tailoring fuel injection rate within the time of a single pulse [7].	2
<b>Figure 2.1</b>	Pictoral schematic of experimental setup.	7
<b>Figure 2.2</b>	Details of the nozzle design.	7
<b>Figure 2.3</b>	Typical Gaussian laser beam intensity profile. Larger drops scatter more light than small drops. Thus, small drops passing through the periphery of the beam are not sufficiently illuminated to be detected by the limited sensitivity of the receiver.	12
<b>Figure 2.4</b>	Spray sampling locations downstream of the nozzle.	14
<b>Figure 2.5</b>	Nozzle pressure waveforms used for data runs at particular locations. Pressure represents the average pressure of all the spray pulses used in a data run.	16
<b>Figure 3.1.1</b>	Time-integrated drop size distributions for different pressure waveforms and sampling locations.	19
<b>Figure 3.1.2</b>	Time-integrated drop velocity distributions for different pressure waveforms and sampling locations.	21
<b>Figure 3.2</b>	Total drop size distribution for the 16ms nozzle pressure waveform integrated over locations A-A, C-A,	
<b>Figure 3.3.1</b>	Evolution of drop size distribution for 16ms symmetric pulse at location B-A.	26
<b>Figure 3.3.2</b>	Evolution of drop velocity distribution for 16ms symmetric pulse at location B-A.	28
<b>Figure 3.3.3</b>	Time evolution of the Sauter mean diameter for different pressure waveforms and	31
<b>Figure 3.3.4</b>	Time evolution of the average drops/pulse recorded for different pressure waveforms and different sampling locations.	32
<b>Figure 3.3.5</b>	Time evolution of the velocity recorded for different pressure waveforms and different sampling locations.	33
<b>Figure 3.4.1</b>	Continuous 789, 888, and 986 psi nozzle pressure spray drop size (a) and drop velocity (b) distributions.	34

# Chapter 1

## Introduction

In order to understand fuel spray formation in fuel injection systems, this work has investigated the basic spray formation of a simple, intermittent fuel spray. Several different nozzle pressure waveforms were applied to a single, cylindrical orifice. The resulting spray was then analyzed using Aerometric's Phase/Doppler Particle Analyzer.

The rise and fall of the driving pressure in the nozzle subjects the fluid to different rates of acceleration as it leaves the nozzle. Thus, if different pressure pulses are applied to the nozzle, there should be some consistent pattern of drop size and velocity distributions since the spray formation is a dynamic process which is sensitive to the dynamic pressure input. Comparison of different pressure waveforms in the nozzle and their respective spray distributions can then be used to optimize intermittent spray technology.

There are several studies of intermittent sprays which measure the time-resolved drop size and velocity distributions [1-5]. These studies have all relied upon conventional fuel injection pumps and injectors that are difficult to use for a systematic evaluation of a dynamic pressure input's influence on spray evolution. These systems were typically designed for specific commercial applications.

For example, Sangeorzan et al [3] give time-resolved spray distributions produced by a conventional diesel injection system. There is no systematic investigation of the influence of a dynamic pressure input to the injector, but they point out that there are cycle to cycle variations in the spray produced. They indicate that these cycle to cycle variations are probably due to line pressure variations. However, the basic influence of a dynamic pressure input on spray formation has still been left vague. The line pressure variations were a defect in their system, not the object of their study.

Nonconventional injection systems have also been used for injection studies. For example, Sinnamon et al [11] used a solenoid-operated injector which creates nearly square nozzle pressure waveforms of various durations during their study of spray trajectories in an engine. Ruiz and Chigier [12] used the same type of solenoid-operated injector to study the spray angle. Although they do not measure the influence of a dynamic pressure input on the drop size and velocity distributions directly, they do study its indirect influence through observed spray angles and trajectories.

Although the influence of a dynamic pressure input has not been studied directly, its importance has been suggested. It is clear from Glikin [6] and Dolenc [7] that the dynamic pressure input to the nozzle is very important to engine efficiency. In their discussion of optimizing fuel injection systems, they point out how injection flow rate is responsible for such qualities of engine performance as specific fuel consumption, noise, nitrous oxide emissions, and smoke emissions. General design criteria show the trade-offs of having different injection rates at different times in the injection process

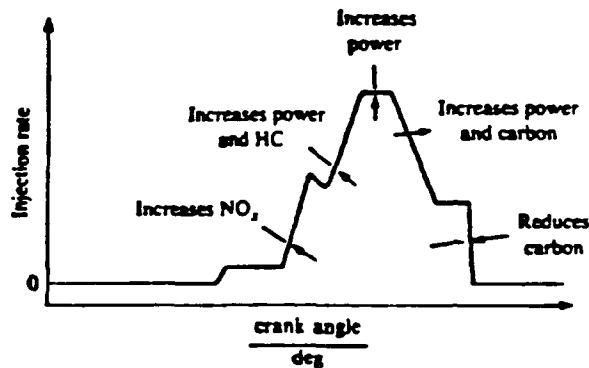


Figure 1.1 Engine performance trade-offs in tailoring fuel injection rate within the time of a single pulse [7].

(see figure 1.1). Since the pressure differential across the nozzle orifice dictates the injection rate, we can conclude the importance of a dynamic pressure input to engine efficiency.

There has also been the practical application of injection rate tailoring to conventional fuel injection pump, pipe, and nozzle systems. Computer programs [6,8] have been written which can predict time-resolved injection rates for specific systems. Engineers use these programs to optimize hardware components according to the performance trade-offs like those in figure 1.1. Two-stage injectors [9,10] have also been developed to provide low injection rates at the start of injection and high injection rates during the remainder of the injection. The result of two-stage injection is lower noise and emissions for engines using them.

However, by focusing on injection rate alone and not spray formation as a result of a particular injection rate schedule, a fundamental basis for engine efficiency is not established. The fundamental change taking place with varying injection rates is a change in spray characteristics that effect the combustion process. Further investigation should be directed toward the connection between injection rate and spray characteristics, as well as the impact of different sprays on combustion. This is the rationale for the present study.

Further complicating the issue of atomization in fuel injection is the problem posed by the small injection chambers found in reciprocating internal combustion engines. Studies of spray angles and trajectories are important because they are concerned with optimizing the spray within the confines of small chambers. Likewise, it is important to study the dense core of intermittent sprays which tends to splash off the chamber walls. Previous experimental studies [13,14] of the core have tried to measure the size of the core. Koo and Martin [5] have shown that Aerometric's PDPA system can measure drop size distributions in dense regions near the core with some success.

Characterization of the core in relation to different pressure inputs is the key to minimizing the core size.

Optimization of the injection spray in general, has been done empirically. Successfull injection systems are adjusted to give the best practical performance without regard to the atomization process. The next step is to consider the physical process of atomization in the optimization of injection. Numerical models will someday be able to predict optimal design criteria.

The influence of a dynamic pressure input upon spray formation is being analytically investigated by Lin, Woods, and Zhou. They are developing a numerical model from first principles to compute the motion of a liquid through a plain orifice, into the core region, and on to the outer atomized regions. Validation of their work through experimental results like those presented here will tie together all of the factors involved in atomizing a liquid jet through a cylindrical orifice.

# Chapter 2

## Experimental Setup and Procedure

### 2.1 EXPERIMENTAL SETUP

The experimental apparatus was designed to produce regular pulses of high pressure liquid at the nozzle; record the time-resolved pressure waveforms of the high pressure pulses; capture drop size and velocity information about the resulting spray; and contain the spray in a safe, non-obtrusive manner. It was of particular importance that the apparatus be able to generate regular pulses with a user selectable pressure waveform in order to automate the process.

Conventional fuel injection equipment was not used mainly for its inflexibility in producing user selectable nozzle pressure waveforms. In addition, the nozzle pressure waveforms produced by previous studies [1-5] of time-resolved spray analysis were not smooth. Typically, there are high frequency pressure fluctuations superimposed upon a square pressure waveform. Although these fluctuations are of practical importance, it is more difficult to investigate them analytically. Smooth, low frequency nozzle pressure waveforms are more suitable for the longer time steps in numerical models that may use this data.

Thus, a custom system was built around an electrohydraulic valve that controlled

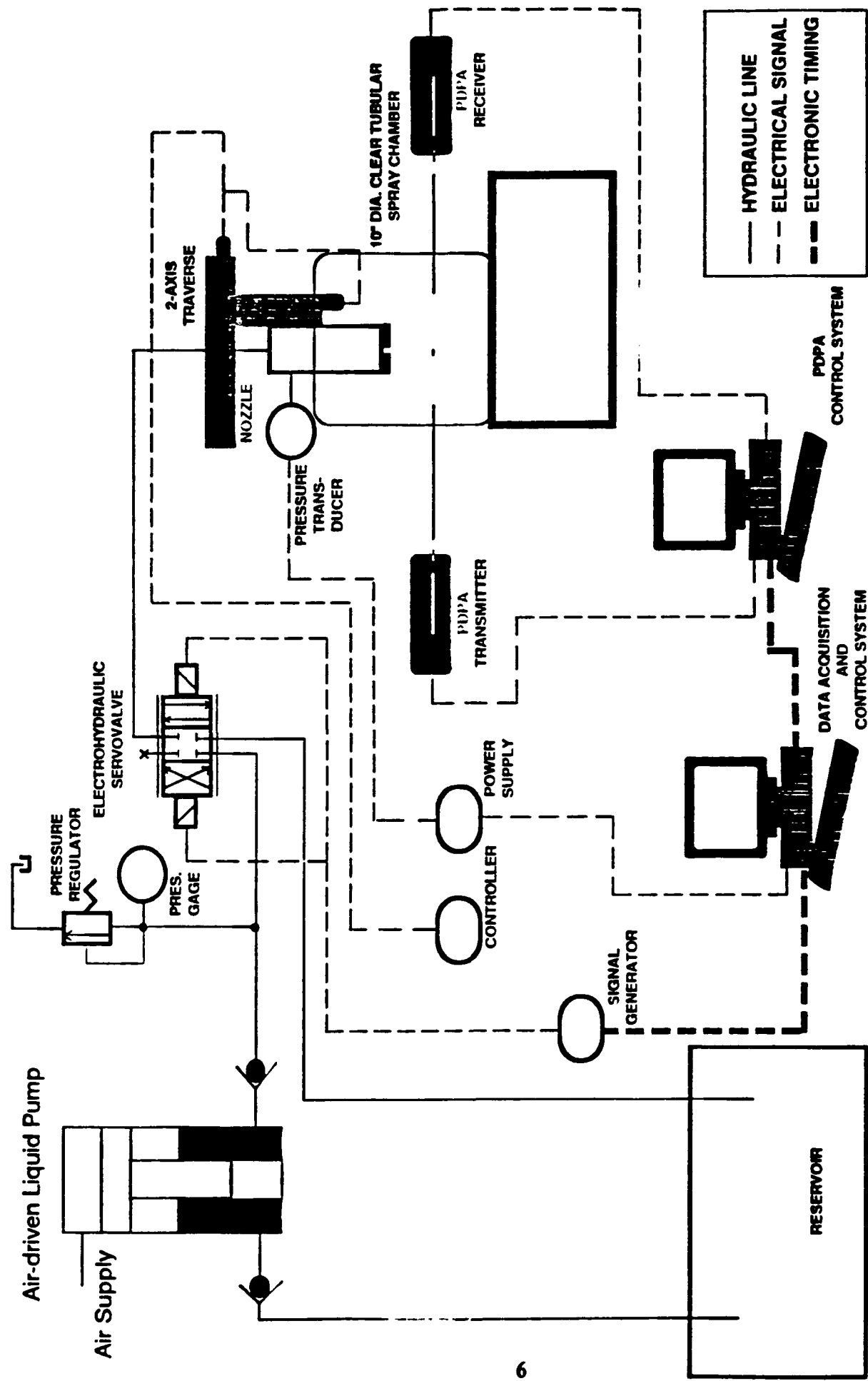


Figure 2.1 Pictorial schematic of experimental setup

fuel flow proportionally to an electric signal in order to meet the need for a smooth pressure waveform. The system consistently produced smooth, low frequency nozzle pressure waveforms as desired.

The basic system involves a high pressure pump that supplies diesel at nearly constant pressure to the electro-hydraulic valve. A signal generator modulates the flow through the valve to the nozzle. The nozzle pressure is measured by a transducer located in a port behind the cylindrical nozzle orifice (see figure 2.2). A two-axis traverse moves the nozzle relative to the fixed probe volume, changing the spatial sampling location in the spray. The following paragraphs describe the components in further detail.

A high pressure, air-driven liquid pump (Haskel Model AW-35) was used to provide a source of high pressure fuel to the electrohydraulic valve. This pump utilizes a reciprocating piston to move and compress the fluid. The reciprocating action produces an unwanted fluctuation in the supply pressure. A hydraulic accumulator just downstream of the pump is an effective approach to reducing these unwanted fluctuations which are common to all piston pumps. In this case, the expense of an accumulator was avoided, since the pump provided a long period of constant pressure compared to the period of unsteadiness. Those injections associated with the supply pressure unsteadiness could be rejected by later processing because their maximum pressure amplitude is outside a selected range. That is, injections were generated without regard to the pump pressure fluctuations. The data associated with the periods of supply pressure unsteadiness are characterized by pressure pulses of low maximum pressure amplitude.

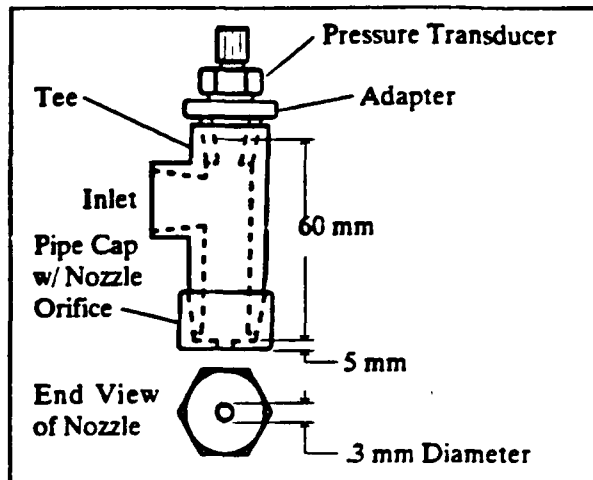


Figure 2.2 Details of the nozzle design.

Processing of the data involved selecting data for which the maximum pressure amplitude falls within the 936psi to 1036psi range. Only those pulses selected were used for the statistical studies.

Originally, the reciprocating action of this pump was meant to be the direct source of intermittent pulses; however, the pump's low frequency and the limited control achievable over the pressure waveform proved inadequate. Instead, the intermittent pulse was generated by an electrical signal to a proportional hydraulic valve. This valve would open and close proportionally to an electrical signal within its limited frequency response and modulate the flow of liquid to the nozzle.

A signal generator (Hewlett-Packard Model 3312A) was used directly to control the electrohydraulic valve. Both the frequency and the waveform of the electrical signal could be controlled with this generator, thereby permitting control of the intermittent spray pulsation frequency and nozzle pressure waveform.

The nozzle pressure was recorded with a digital data acquisition system (Keithley Model S-500) using a piezoelectric pressure transducer (PCB Piezotronics Model 111A22 with zero clamping power supply) located in the nozzle chamber behind the nozzle orifice (see figure 2.2). The time resolution of the recorded pressure was 1ms and the pressure resolution was better than 5 psi.

Drop size measurements were recorded unobtrusively using a single axis Aerometric Phase/Doppler Particle Analyzer (Transmitter Model XMT-1100-4S, Receiver Model RCV-2100, Motor Controller Model MCB-7100-1, Signal Processor Model PDP-3100, and Data Management System Model DMS-4000-5). This equipment analyzes the spatial and Doppler frequency of an interference pattern generated by two intersecting laser beams as drops pass through the intersection point in order to determine the size and velocity of those drops (a detailed description of this system can be found in David Woods' thesis [15]). The system was setup in forward scatter mode

with the receiver oriented 30° off the transmitter axis. Drop size information was recorded continuously over many intermittent pulses. That is, each data run involves numerous injections with the same pressure waveform. Initiation of drop size information gathering was achieved through an external trigger generated by the pressure waveform data acquisition system in order to synchronize the two data collection processes.

The external trigger signals the start of timing clocks in both the Keithley and Aerometric systems. These are the clocks which mark the arrival of data with respect to the start of data run. Each clock starts at time zero on the trigger signal, i.e. the time of drop detection and pressure sampling are relative to the initial trigger signal.

Velocities are measured parallel to the axis of the spray and are considered positive travelling away from the nozzle. Acceleration due to gravity is also parallel to the axis of the spray and positive travelling away from the nozzle.

## **2.2 PHYSICAL PROPERTIES OF THE TEST FLUID**

Since most studies have been diesel and the primary application of this work is diesel injection, locally obtained No. 2 diesel fuel was used for these experiments. There is no problems associated with using diesel fuel with the hydraulic equipment; however, it is requires adequate ventilation.

The density of the fuel was found to be 0.830 g/cm<sup>3</sup>. Viscosity was measured to be 4.464 centistokes ( $4.464 \times 10^{-2}$  kg·m<sup>-1</sup>·s<sup>-1</sup>) using a Cannon Viscometer model OC-B223 (capillary tube efflux method). Surface tension was measured to be 31.15 dynes/cm using a DuNouy Tensiometer model 70535 (ring method). All tests were conducted at the room temperature of 21°C.

## **2.3 EXPERIMENTAL PROCEDURE**

The spray resulting from a given nozzle pressure waveform varies from pulse to

pulse due to the randomness of the atomization process. Averaging of the spray characteristics over a number of spray events provides a more general representation of what might be expected from any given spray event. Thus, the connection between the dynamic pressure input and the resulting spray is presented as the average of approximately seventy spray events. Each spray event is defined here to be the period starting 10ms before the nozzle pressure peak and ending 30ms after the pressure peak. The local zero reference time from one injection event to another was picked to be the time of the pressure peak occurrence for each injection. Thus, the time-resolved characteristics could be averaged by aligning each injection by its peak. This assumes that each waveform is nearly the same for injections with peak pressures in the 936 - 1036psi range. The variation in the pressure waveform is studied in section 2.5.

A particular nozzle pressure waveform and its spray were analyzed at a particular location by simultaneously recording pressure and spray characteristics over a period of 20 seconds and many injections. Data for individual pulses was then taken out of the continuous data stream with off-line processing.

The first priority was to establish a continuously pulsating spray with the desired nozzle pressure waveform. After the system was pressurized by the supply pump, a sinusoidal signal was applied to the control valve. The system was allowed to run until a regular pulsating spray was established which takes a few minutes. It seemed that the valve needs to get warmed up before it responds well to the relatively high frequency applied to it. Once a regular pulsating spray was established, adjustment to the function generator was made while observing the resulting nozzle pressure waveforms. This procedure was repeated for every data run. Since there was a separate data run for every new position, there was the potential that a single nozzle pressure waveform could not be faithfully repeated from one data run to the next. Graphs presented in section 2.5 show that an acceptable repeatability was maintained from one location to

another using the same pressure waveform. Stopping the spray between data runs was done to insure that the build up of drops on the chamber windows did not obstruct the PDPA system. The chamber windows were cleaned between data runs.

After establishing a pulsating spray for analysis, approximately one thousand drops were test recorded with the PDPA system to check its operating parameters. Typically, the photomultiplier tube (PMT) power needed to be adjusted in order to maintain sensitivity to the smallest drops without incurring saturation rejections [17]. The size and velocity range of measurement was another important consideration from one data run to another. However, one size and velocity range was found to be adequate for all of the data runs.

Actual data runs are initiated quickly after adjusting the PDPA system to avoid excessive wetting of the chamber windows. Starting the data collection routine on the Keithley data acquisition system triggers simultaneous recording of the nozzle pressure by the Keithley data acquisition system and drop information by the PDPA system. Each system records its data independently, but each individual data item in both systems has a time stamp relative to the start of acquisition. Thus, each data run has a pair of data sets. One set contains the nozzle pressure recorded every millisecond and the other contains drop size and velocity information recorded as the drops were detected.

Once the raw pressure and drop information was collected, off-line analysis was then done to remove data associated with undesired nozzle pressure waveforms (due to the supply pressure variation) and to perform the desired statistical functions. The off-line analysis references the local pressure peak of each injection. Thus, to perform the analysis, the local pressure peaks must be found in the continuous stream of data in a data run. The number of injections in a data run dictates that the process be automated. Local peaks are found by using a second order polynomial to interpolate a more accurate pressure peak from each local peak in the stream of pressure data. All

pressure pulses with interpolated peaks in the 936 to 1036psi range were kept and the others rejected (see Appendix A.1). The time offset between the interpolated peak and the recorded peak pressure was also recorded in order to accurately compute average pressure statistics for a given data run (see section 2.5, and Appendix A.2).

Handling of the PDPA data required exporting the data sets from Aerometric's binary format to standard ASCII format for use with custom Fortran programs. The Aerometric's software is capable of handling a regular pulsating jet; however, the fluctuations in pump supply pressure required editing of the data. For that reason, the Aerometric's software could not be used. In addition, the use of Fortran programming (see Appendix A.3) allowed more flexibility in automating the preparation and presentation of spray data in conjunction with the nozzle pressure data.

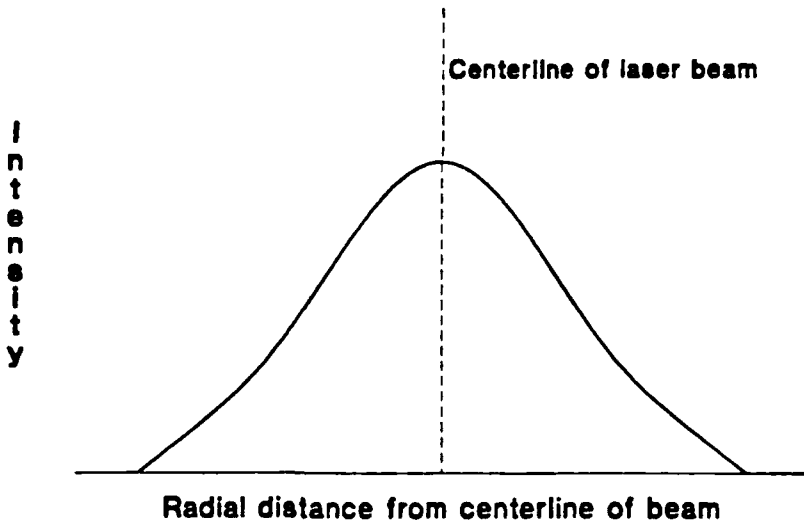


Figure 2.3.1 Typical Gaussian laser beam intensity profile. Larger drops scatter more light than small drops. Thus, small drops passing through the periphery of the beam are not sufficiently illuminated to be detected by the limited sensitivity of the receiver.

There was one problem associated with not using the Aerometric's software for analysis. An error in the detection of small particles occurs when small particles tran-

sit the edges of the probe volume. Since the laser produces a beam with a Gaussian intensity as shown in figure 2.3.1, small particles will scatter less light than larger particles when they transit the periphery of the probe volume. Thus, the smallest size of particles detected increases as the transit path of the particle moves away from the center of the probe volume. The PDPA software calculates the Gaussian intensity of the probe volume in order to determine an actual probe volume for the small drop sizes. It then corrects the distribution statistics by adding a number of drops to the small drop sizes in order to compensate for the different actual probe volumes.

The raw data exported from the PDPA software does not contain corrections for the different actual probe volumes, but rather only gives the data on the actual drops detected. In order to correct my 'custom' distributions, the correction factors were computed from each size range in the PDPA generated distributions (see Appendix A.4). These correction factors were then used to correct the custom distributions for variation in actual probe volumes by adding a proportional number of drops throughout the range of my 'custom' distributions.

## 2.4 SAMPLE LOCATIONS

Figure 2.4.1 shows the six fixed drop size and velocity sampling locations used. Sampling in these locations is achieved by moving the nozzle relative to the probe volume. Since the spray chamber does not move with the nozzle, there is the potential that the change from one sampling location to another will influence the spray dynamics. Observation of the spray in each location showed no visible deflection of the spray caused by the chamber floor or walls.

## 2.5 STUDY OF THE NOZZLE PRESSURE WAVEFORMS USED

The acceleration of the liquid in the atomizing jet is related to the nozzle pressure rate of change. Several smooth pressure waveforms were used to create pulsating jets. This allowed the observation of the change in spray characteristics of the liq-

uid jet undergoing different acceleration patterns. Both symmetric and asymmetric pressure waveforms were created. Variation of the period of the symmetric waveforms produced approximately equal changes in the leading and trailing edges of the time-resolved pressure waveform. The system was also able to significantly vary the trailing edge of the waveform yielding asymmetric pressure pulses. However, the system did not accommodate changing the leading edge of the pressure waveform except in the symmetric case.

Since the spray data presented is based upon the average of many pulses, it is appropriate to consider the variation from one pulse to another. Recall that the pressure peak was determined by second order polynomial interpolation and that there is a time offset of the interpolated peak from the measured peak. For averaging, each pulse is time-aligned by its interpolated peak. Then pressure values are linearly interpolated at the peak offset every millisecond from 10ms before the peak to 30ms after the peak.

The average nozzle pressure waveforms for each data run are presented in sets. Comparison of the same pressure waveform reflects the need to verify the pressure waveform for each data run after shutting down the pulsating spray system between

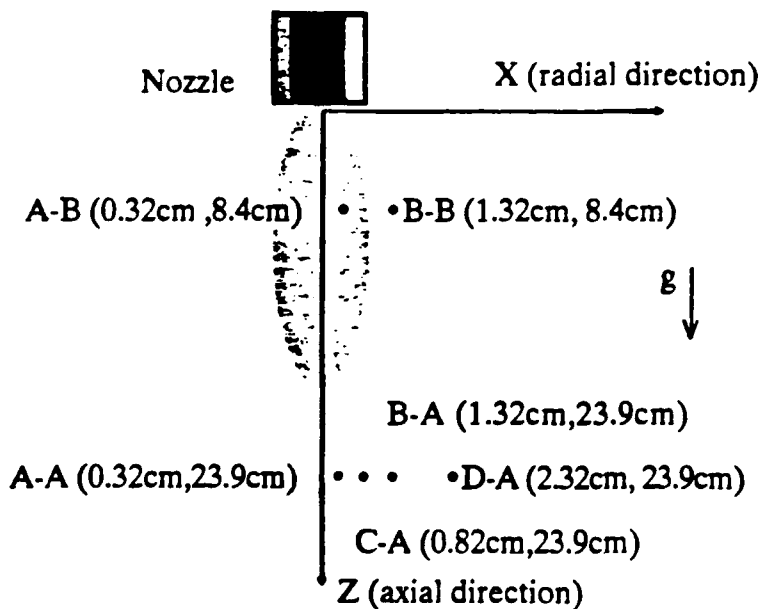


Figure 2.4.1 Spray sampling locations downstream of the nozzle.

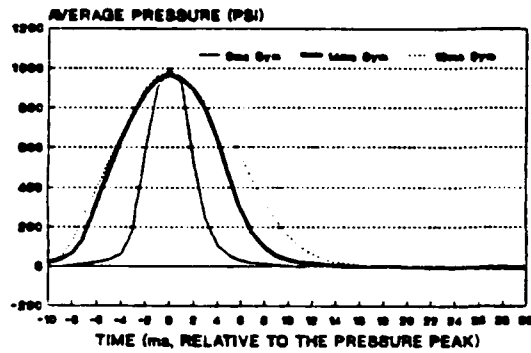
runs. Table 5.3.1 gives the results of calculating the standard deviation for three typical data runs.

Results of the spray analysis will refer to particular pressure waveforms as they are presented here in the following graphs, figure 2.5.1. There are three symmetric pressure waveforms denoted by their approximate duration of 6, 14, and 16ms. In addition, there are two asymmetric pressure waveforms denoted gentle trailing edge (Gentle TE) and steep trailing edge (Steep TE).

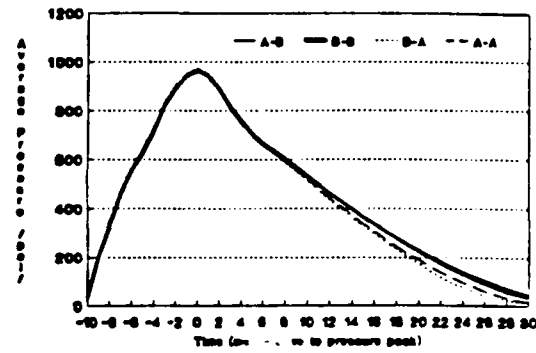
Pulse Waveform	Average Standard Deviation*	Maximum Standard Deviation	Standard Deviation of Pressure Peak
16ms Symmetric at B-A	$\pm 18.6\text{psi}$	$\pm 49.1\text{psi}$	$\pm 16.2\text{psi}$
Gentle TE at B-A	$\pm 24.4\text{psi}$	$\pm 65.8\text{psi}$	$\pm 9.1\text{psi}$
Steep TE at B-A	$\pm 21.6\text{psi}$	$\pm 89.7\text{psi}$	$\pm 16.4\text{psi}$

Table 2.5.1 Typical nozzle pressure waveform statistics.

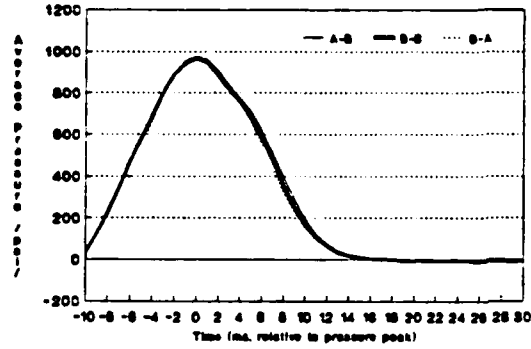
\* The average standard deviation is the average of standard deviations computed on the pressure values at each millisecond.



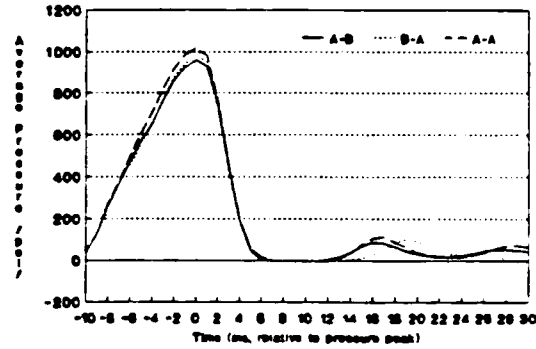
6,14, and 16ms symmetric pulses at location A-B



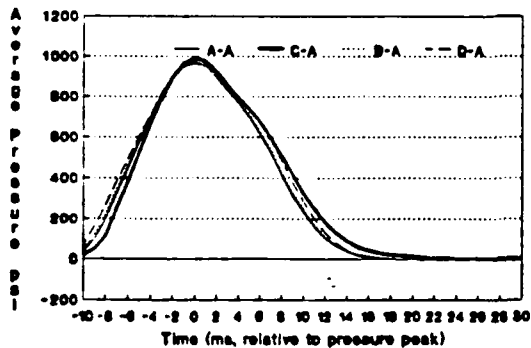
Gentle TE pulses at locations A-B, B-B, B-A, and A-A



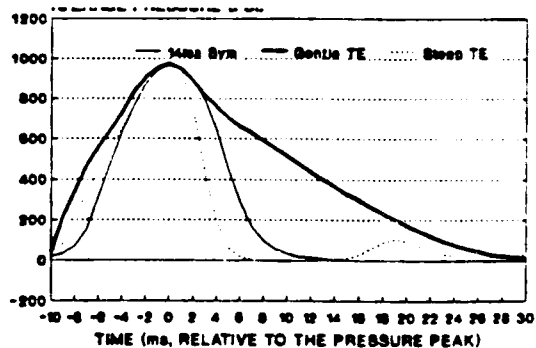
16ms symmetric pulses at locations A-B, B-B, B-A, and A-A



Steep TE pulses at locations A-B, B-B, B-A, and A-A



16ms symmetric pulses at locations A-A, C-A, B-A, and D-A



Comparison of 16ms symmetric, gentle TE, and steep TE pulses at location B-A

Figure 2.5.1 Nozzle pressure waveforms used for data runs at particular locations. Pressure represents the average pressure of all the spray pulses used in a data run.

# Chapter 3

## Results

### 3.0 GENERAL

Drop size and velocity information is presented as the average of measurements taken over approximately 70 spray events. In similar work, Koo and Martin [5] found consistent results from data run to data run using 50 to 100 spray events. Thus, where data is presented over the course of a spray event, it is actually the average of data recorded for a number of spray events. The exact number of spray events used depends upon the number of pulses accepted (see section 2.3 for details of the acceptance criteria) in a given data run.

Comparison of results from one pressure waveform to another, such as the 6ms symmetric to the 16ms symmetric, requires discretion. There is a difference in the duration of the spray event from one waveform to another. This will influence the overall number of drops per pulse because of the change in injected quantity. However, the change in efficiency of atomization is more important to observe, and this change can be seen in the change of distribution profiles.

### 3.1 TIME INTEGRATED DISTRIBUTION OF DROP SIZE AND VELOCITY

Characteristics of the spray produced by various pressure waveforms in the nozzle

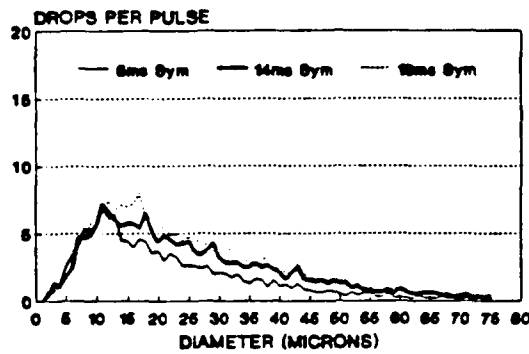
were integrated over the duration of the spray event. The spatial location of the sampling is fixed during the course of the integrations. This data is the average total drop distribution falling in a specific location relative to the nozzle.

Drop sizes of all of the drops recorded in the sample volume during each spray event are tabulated and grouped (by size) into one micron groups from 1 to 75 microns. The totals are then divided by the number of selected spray events, yielding the drops per pulse for comparison, and the results are graphed in figure 3.1.1.

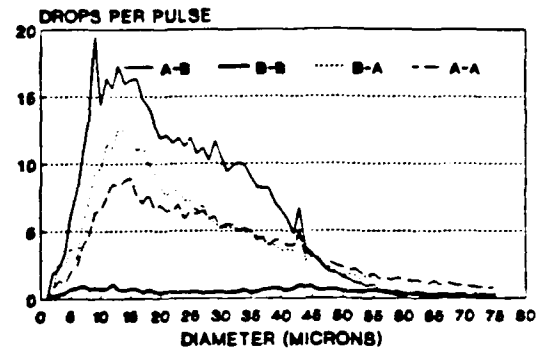
None of the sprays have a monodispersed drop size distribution. Regardless of pressure waveform and sampling location, each total size distribution has its peak drops per pulse occurring in the 10-20 micron size range. The number of drops per pulse falls off sharply in the 0-10 micron range and gradually from 20 to 75 microns.

Comparing the three symmetric waveforms at location B-A, we see an approximately equal rise in drops per pulse from 0 to 10 microns. However, from 10 to 20 microns there is some irregular separation in the distributions, and from 20 to 75 microns each distribution declines at approximately the same rate though separate. The pressure waveform with the longest duration (16ms) has the consistently highest drops per pulse while the shortest (6ms) has the lowest drops per pulse.

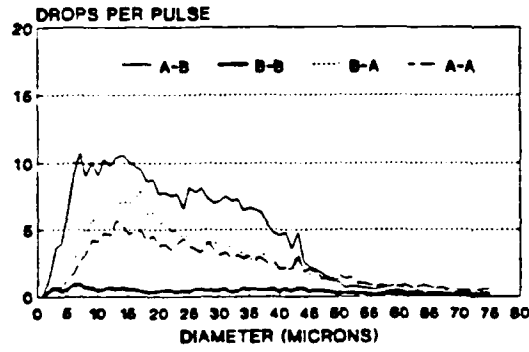
One symmetric waveform (16ms) was also studied in five spatial locations (A-B, B-B, A-A, C-A, and D-A) in addition to B-A. Two upstream locations, A-B and B-B, are compared with two parallel downstream locations, A-A and B-A. We can see that the spray is much more dense at the near axial location A-B by its broad, high drops per pulse distribution. Location B-B shows a low level throughout the range, which is probably due to the spray cone not reaching out that far. The downstream locations have a generally lower level of drops than location A-B throughout the size range due to the spread in the spray cone. In addition, the rise in drops per pulse from 1 to 10 microns is less sharp downstream than at the location A-B, upstream.



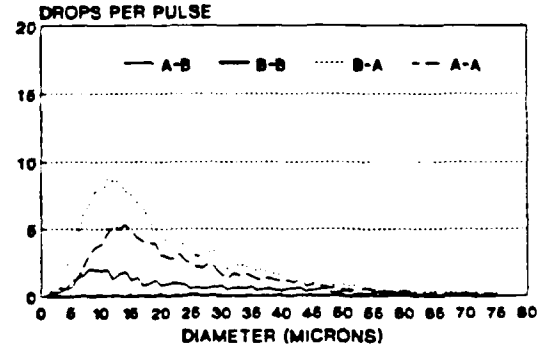
6, 14, and 16ms symmetric pulses at location B-A



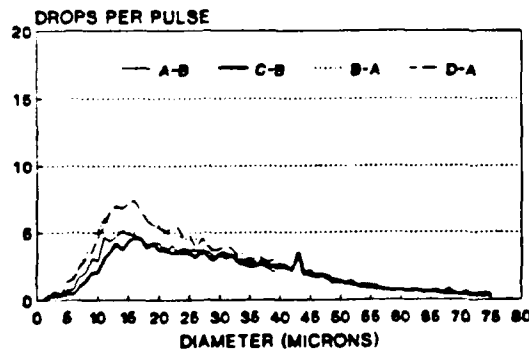
Gentle TE pulses at locations A-B, B-B, B-A, and A-A



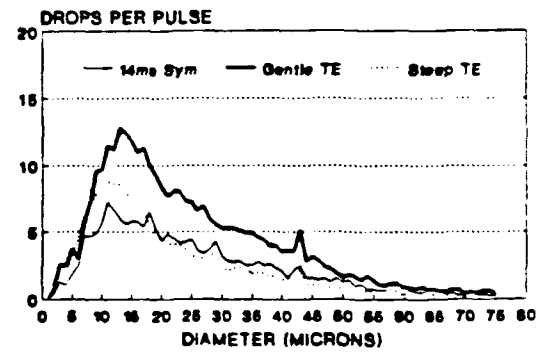
16ms symmetric pulses at locations A-B, B-B, B-A, and A-A



Steep TE pulses at locations A-B, B-B, B-A, and A-A



16ms symmetric pulses at locations A-A, C-A, B-A, and D-A



Comparison of 14ms symmetric, gentle TE, and steep TE pulses at location B-A

Figure 3.1.1 Time-integrated drop size distributions for different pressure waveforms and sampling locations.

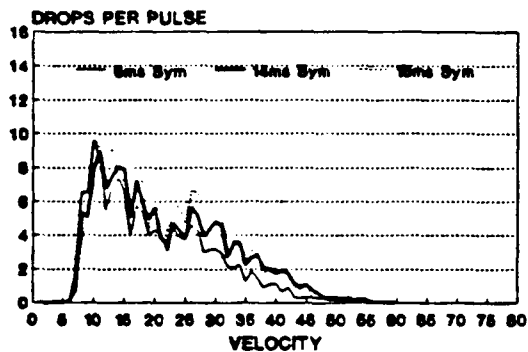
The 16ms Symmetric pressure pulse was also compared in the four radial downstream locations, A-A, C-A, B-A, and D-A. Outer locations B-A and D-A show that there are more small drops per pulse transiting these locations than the inner locations.

The Gentle TE pressure waveform was compared at the four spatial locations A-B, B-B, B-A, and A-A. Again, the highest drops per pulse throughout the size range were found at location A-B although the distribution has a more dramatic peak in the 10-20 micron range than the 16ms Symmetric pulse. Downstream locations have a less steep rise in drops per pulse from 1 to 10 microns than A-B. They are also at higher levels than the 16ms Symmetric pulses at the same locations. The outer location B-A has more drops per pulse in the 10-20 micron range than the near axial location A-A as we see with the 16ms Symmetric pulse.

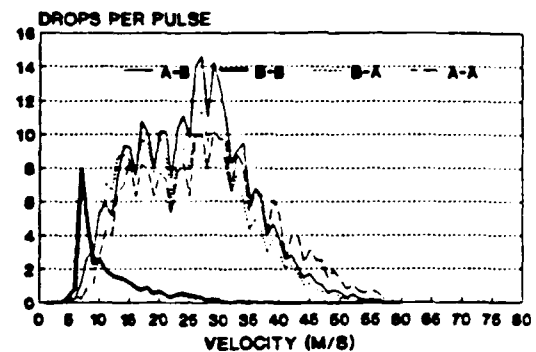
The Steep TE pressure waveform was compared at the four spatial locations A-B, B-B, B-A, and A-A. We see that the upstream location A-B has a relatively low drops per pulse throughout the size range in contrast with the 16ms Symmetric and Gentle TE pulses. The downstream outer location B-A has broad peak from 5 to 20 microns and has a higher drops per pulse throughout the whole size range than the near radial location A-A.

Note the consistent spike in the number of drops per pulse at 43 microns, which is typically 25% greater than adjacent drops per pulse levels. Other spikes or fluctuations occur, but they do not appear consistently and are probably due to statistical considerations. The repeated occurrence of this spike at 43 microns, without regard to pressure waveform and sampling location, indicates that it is probably a physical phenomena and not an error. Testing of other sprays showed no increased sensitivity of the Aerometric's system to this size drop.

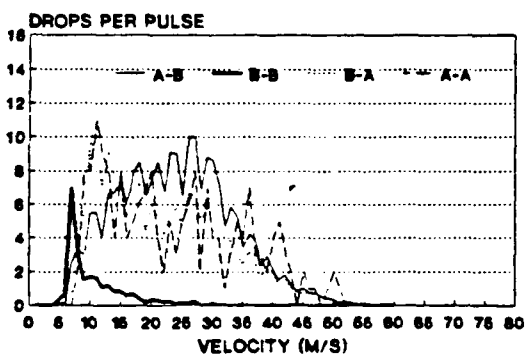
Velocities of all of the drops recorded in the sample volume during each spray event are also tabulated and grouped into 1m/s groups from 1 to 75m/s. The resulting



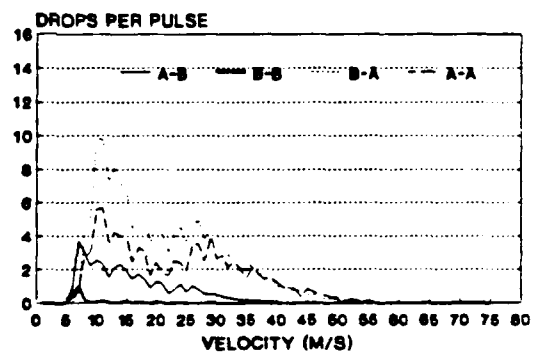
6, 14, and 16ms symmetric pulses at location B-A



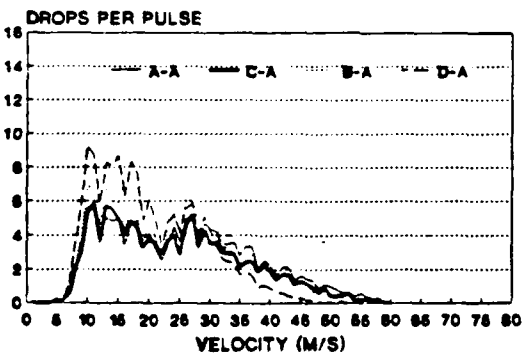
Gentle TE pulses at locations A-B, B-B, B-A, and A-A



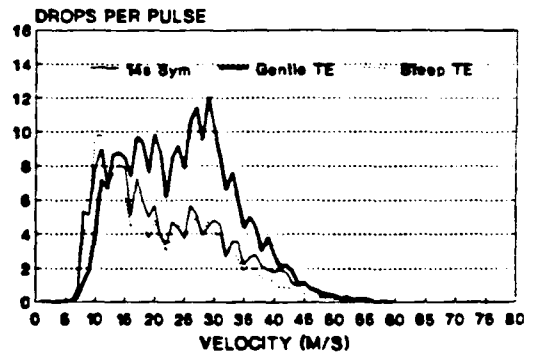
16ms symmetric pulses at locations A-B, B-B, B-A, A-A



Steep TE pulses at locations A-B, B-B, B-A, and A-A



16ms symmetric pulses at locations A-A, C-A, B-A, and D-A



Comparison of 14ms symmetric, gentle TE, and steep TE pulses at location B-A

Figure 3.1.2 Time-integrated drop velocity distributions for different pressure waveforms and sampling locations.

totals are then divided by the number of spray events, yielding the drops per pulse in figure 3.1.2 for comparison. There is quite a bit more fluctuation in the individual time-integrated velocity profiles.

The velocity profiles are bimodal at all downstream locations for every pressure waveform. Peak drops per pulse occur at approximately 10-15 m/s and 25-30 m/s. The 10-15 m/s peak surpasses the 25-30 m/s peak for all the symmetric pressure waveforms and the Steep TE waveform, but the opposite is true for the Gentle TE waveform.

Upstream, the velocity profiles for the 16ms Symmetric and Gentle TE pressures are broad near the axis at A-B and sharp away from the axis at B-B. The peak drops per pulse are in the same magnitude range as the downstream locations except for the Steep TE pressure waveform which has much lower peaks in contrast.

### 3.2 TEMPORALLY AND SPATIALLY INTEGRATED DROP SIZE DISTRIBUTION

Drop size information was integrated over the course of the spray event at radial locations A-A, C-A, B-A, and D-A for the 16ms Symmetric pressure waveform. The total drops are divided by the number of spray events.

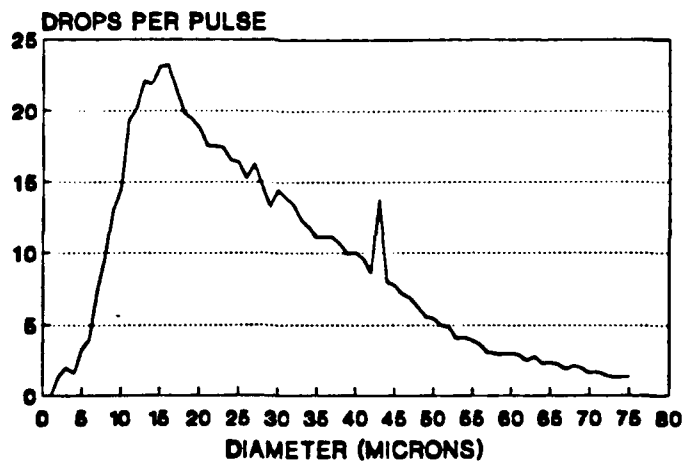


Figure 3.2.1 Total drop size distribution for the 16ms nozzle pressure waveform integrated over locations A-A, C-A, B-A, and D-A.

Here we get a more refined view of the total downstream drop distribution than looking at one location only. Common characteristics of the respective individual profiles in figure 3.1.1 can be found in the total combination of the graphs. For instance, there is the steep rise in the drops per pulse from 0 to 10 microns. The peak drops per pulse occurs in the 10-20 micron range, and the drops per pulse falls off gently from 20 to 75 microns. The spike at 43 microns is also very clear.

### 3.3 TIME EVOLUTION OF DROP SIZE AND VELOCITY DISTRIBUTIONS

The size of all of the drops recorded in the sample volume during each 2ms period in the spray event are tabulated in one micron groups from 0-75 microns; while the velocity of all the drops recorded are tabulated in 1m/s groups from 0-75 m/s. The resulting totals are then divided by the number of spray events in order to get an average number of drops per pulse for comparison. Each set of totals produces an "instantaneous" distribution histogram for every other millisecond of the spray event.

There are a total of fifty-eight drop size and velocity histograms to cover a spray event with 2ms resolution. Therefore, only the distribution histograms for the 16ms symmetric pressure pulse at location B-A are presented here (see figures 3.3.1,2).

Both the size and velocity histograms show that the spray does not arrive at the downstream location B-A until the 2ms period after the pressure pulse reaches its peak. Drops continue passing this location 46ms after the pressure peak.

The size histograms start out broad when the spray reaches the sampling location, but the small drops in the 10-20 micron range dominate quickly until about 40ms after the pressure peak. There is a small bimodal indication which is most pronounced 12-14ms after the pressure peak. The bimodal peaks are at roughly 16 and 40 microns. Although it is impossible to determine the exact correspondance of the nozzle pressure with the drops found downstream of the nozzle, the bimodal indication occurs during the time when the peak number of drops is being recorded.

Axial velocity of the drops also starts out broad, but becomes quite narrow in range. The velocity distributions from 4 to 12ms after the pressure peak have nearly symmetric distributions around 30m/s. After 12ms the velocity distributions tend towards a narrow band at 10m/s.

Average data is extracted from distribution histograms for each waveform at each location to yield graphs of Sauter mean diameter, drops per pulse, and mean velocity (see figures 3.3.3-5). These graphs summarize the instantaneous distributions histograms. The time resolution of these summary graphs is 1ms compared to the two millisecond resolution presented in figs. 3.3.1 and 3.3.2. Original histogram data has 1ms resolution, but histograms were combined to reduce the number of histograms presented in half.

### 3.4 CONTINUOUS JETS

Drop size and velocity data were recorded for continuous jets of 789, 888, and 986 psi at location B-A. Since these are continuous jets, the convenient measure of drops per pulse cannot be used. Rather, the number of drop totals are presented. Comparison can be made to the distributions for pulses by qualitative evaluation of the distribution profiles. The size and velocity mean data (see table 3.4.1) can be directly compared to those means presented for pulsating sprays.

Pressure (psi)	Sauter Mean Diameter	Mean Velocity (m/s)
986	45.9	31.3
888	45.7	31.0
789	86.2	26.3

Table 3.4.1 Statistics for continuous sprays at 789, 888, and 986psi nozzle pressures.

In figure 3.4.1 we see at 888 and 986 psi that the drop size distribution rises steeply from 0 to 10 microns, peaks in the 10-20 micron range, and declines gently from 20 to 75 microns. All three pressure ranges have a spike at 43 microns. Other significant spikes occur at 7 and 23 microns for the 888psi profile and 12 microns for the 986 psi profile. The 789 psi drop size distibution is broad with a gentle peak in the 30-45 micron range except for a spike at 43 microns.

The velocity profiles are somewhat symmetric. We can see that the profiles for 888 and 986 psi are quite close with peaks in the 27-33 m/s range. The 789 psi velocity profile peak is in the 22-30 m/s range.

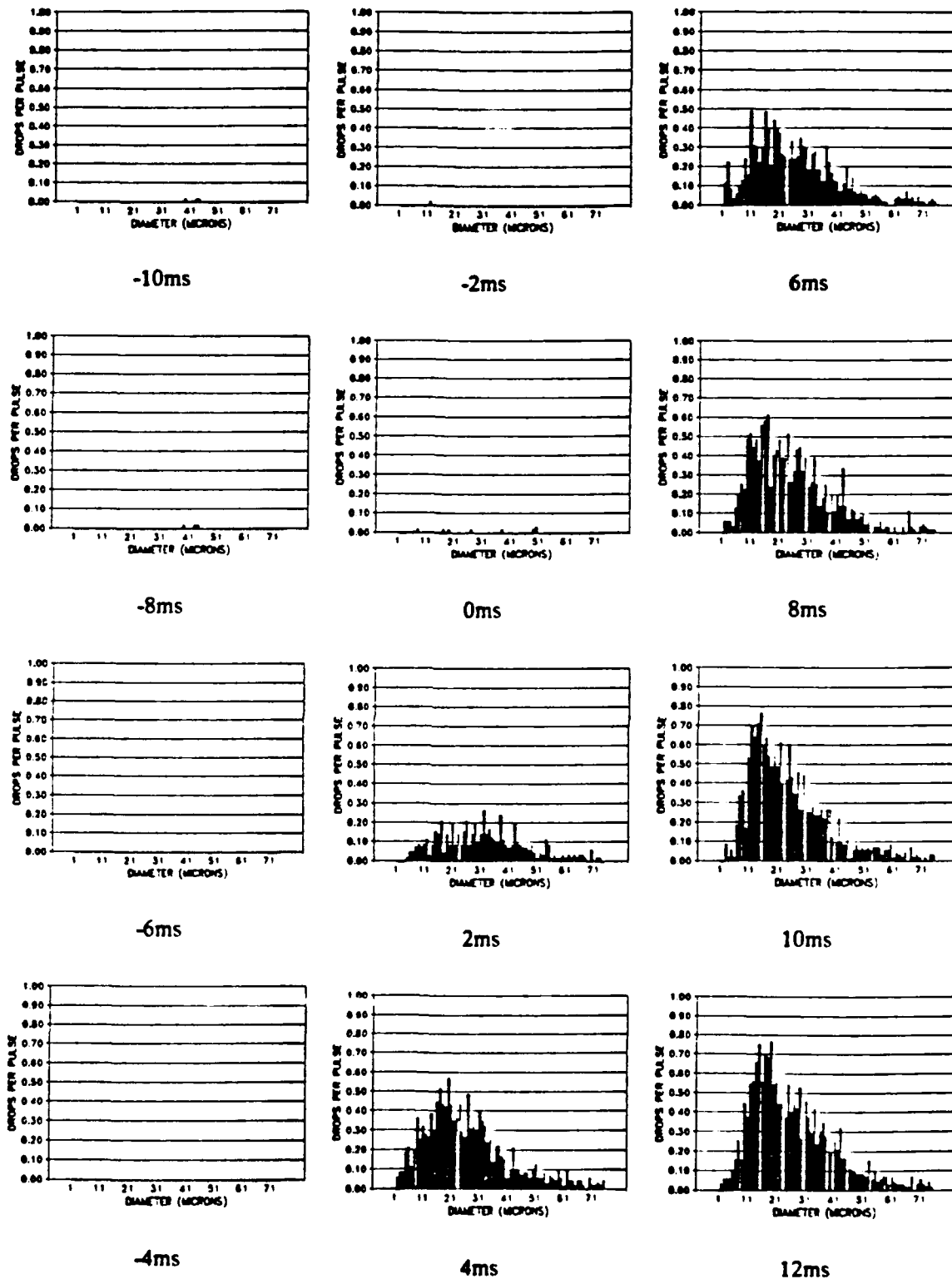
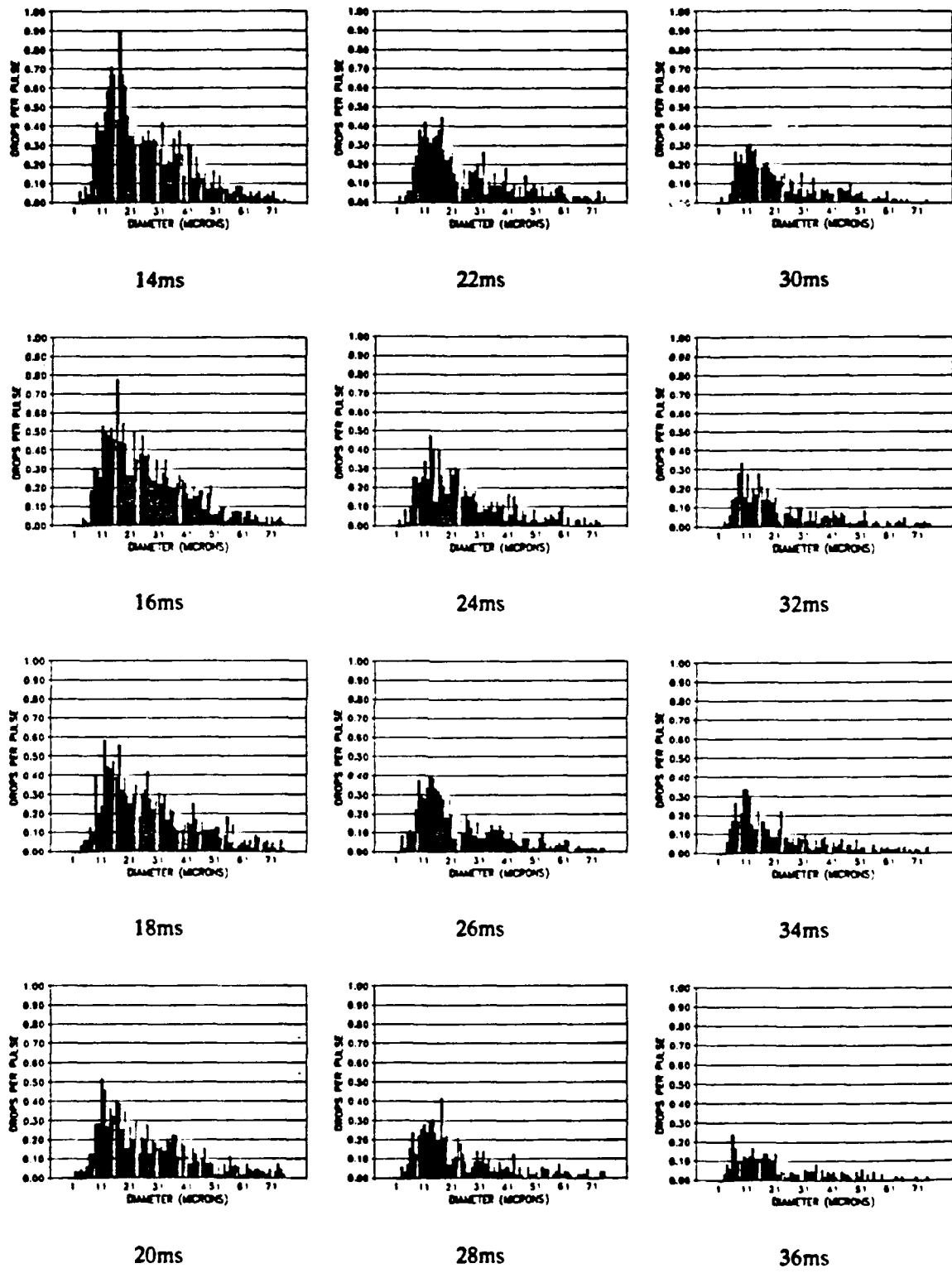


Figure 3.3.1 Evolution of drop size distribution for 16ms symmetric pulse at location B-A.



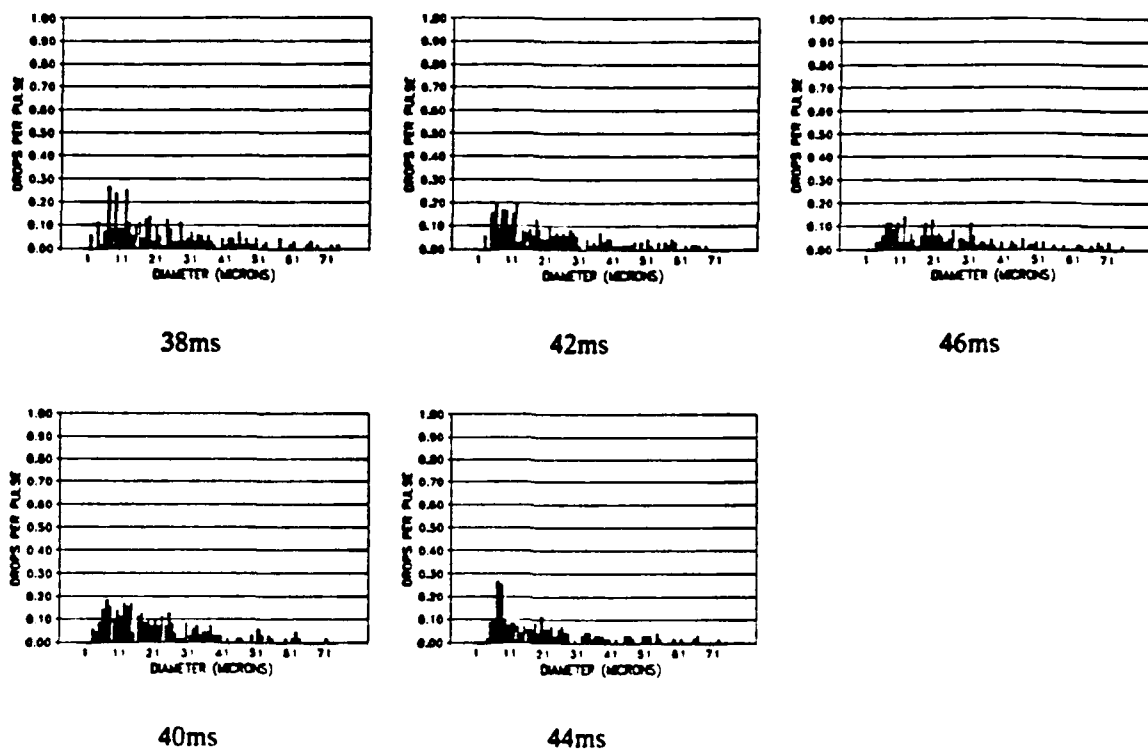


Figure 3.3.1 cont'd. Evolution of drop size distribution for 16ms symmetric pulse at location B-A.

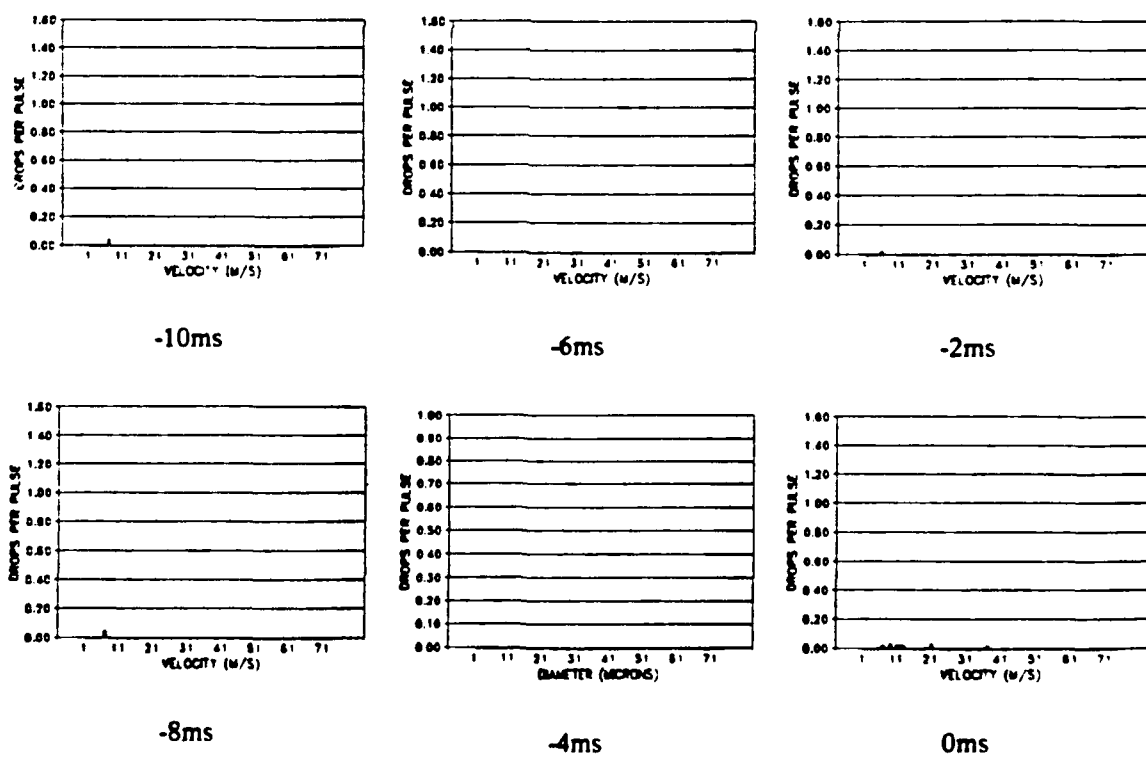
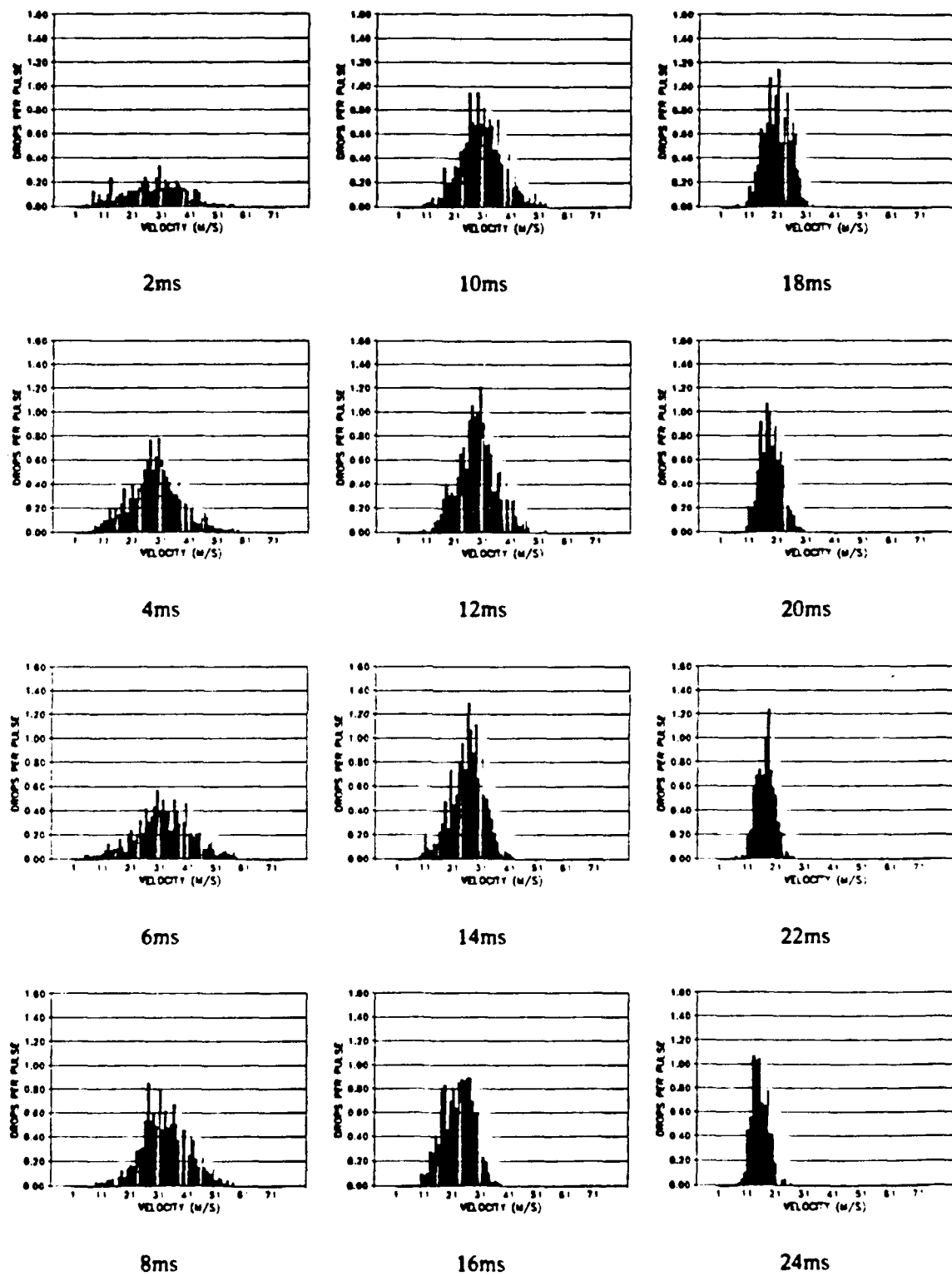
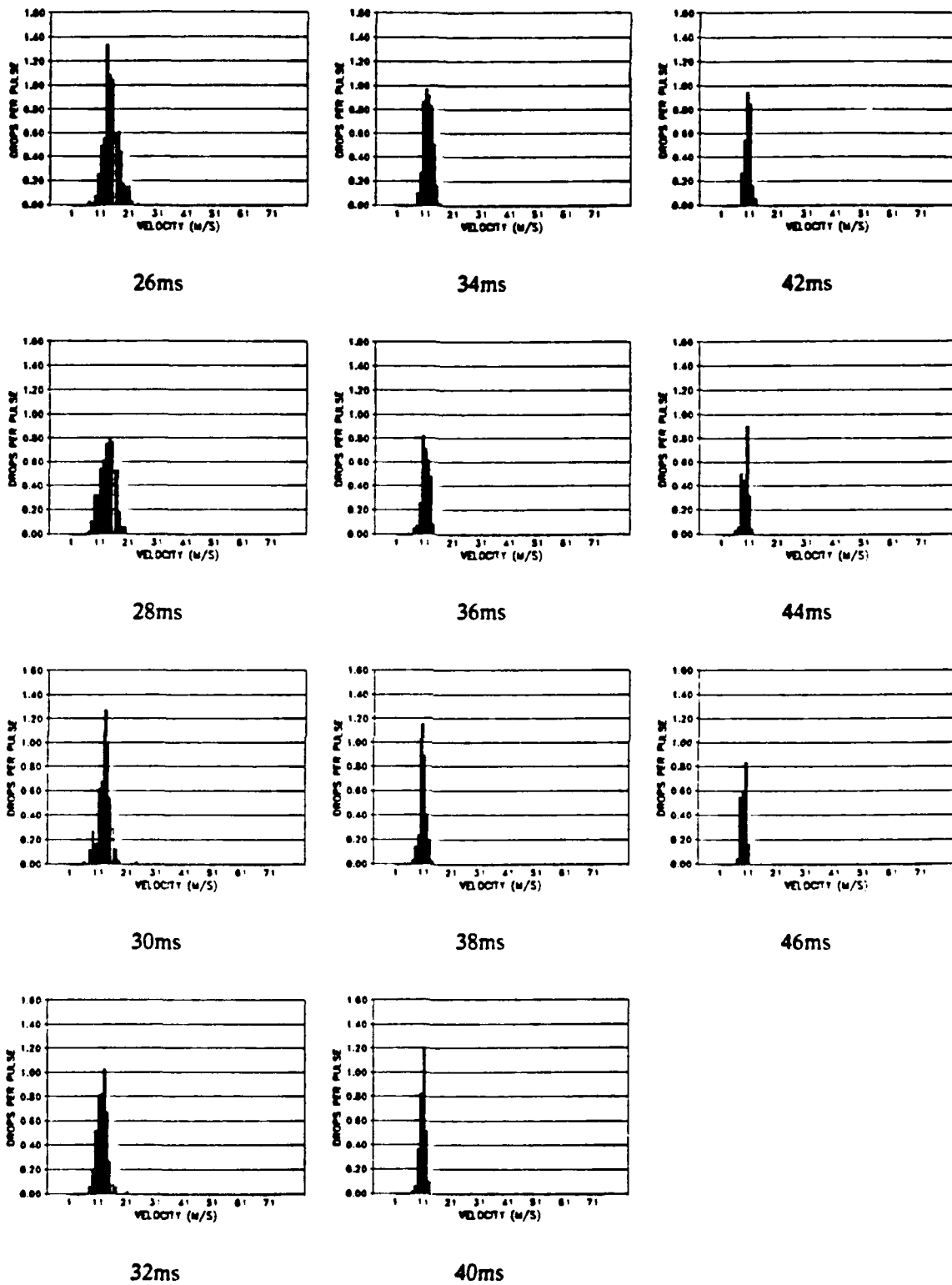
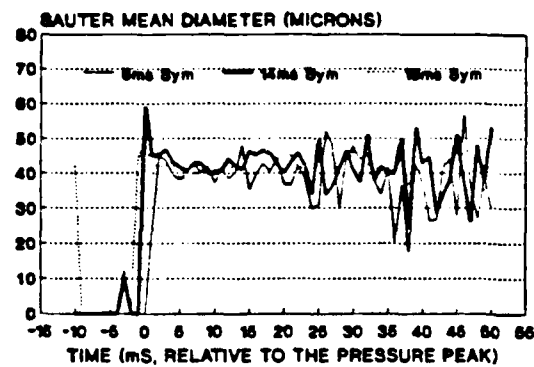


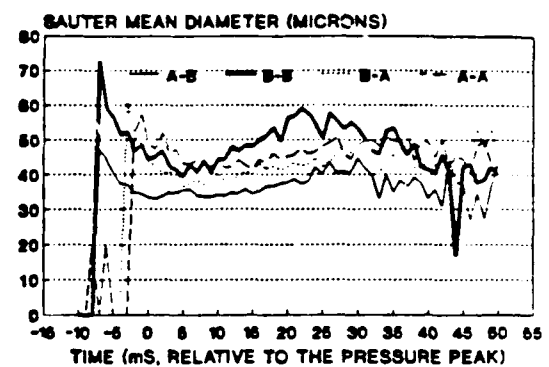
Figure 3.3.2 Evolution of drop velocity distribution for 16ms symmetric pulse at location B-A.



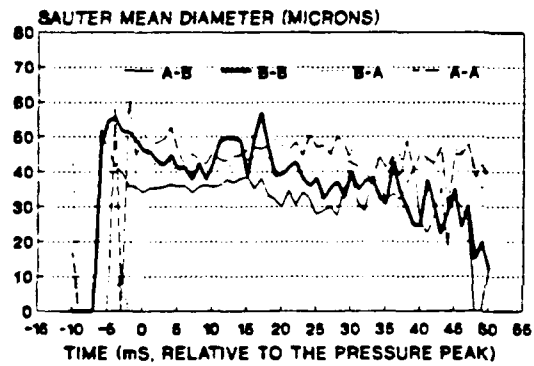




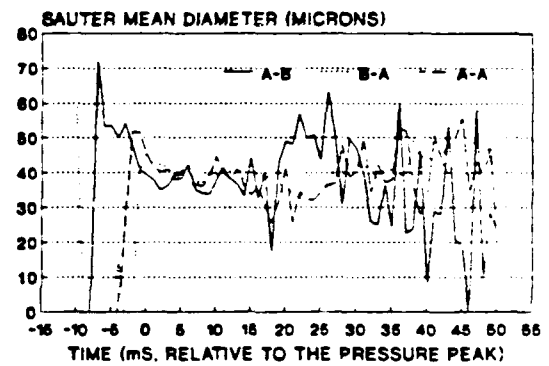
6, 14, and 16ms symmetric pulses at location B-A



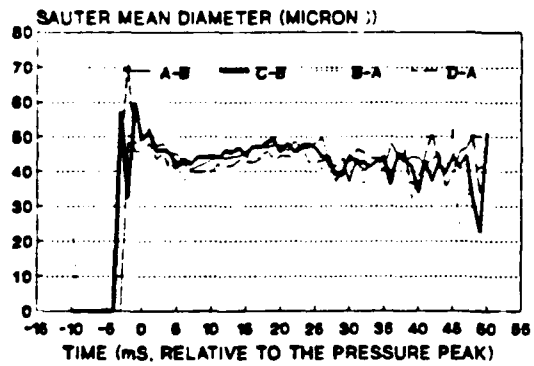
Gentle TE pulses at locations A-B, B-B, B-A, and A-A



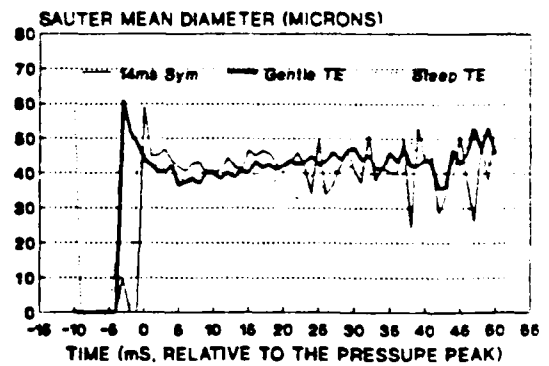
16ms symmetric pulses at locations A-B, B-B, B-A, and A-A



Steep TE pulses at A-B, B-A, and A-A

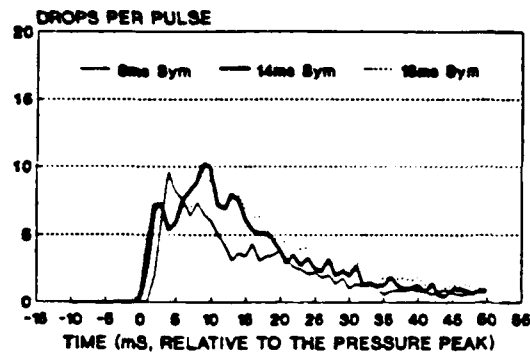


16ms symmetric pulses at locations A-A, C-A, B-A, and D-A

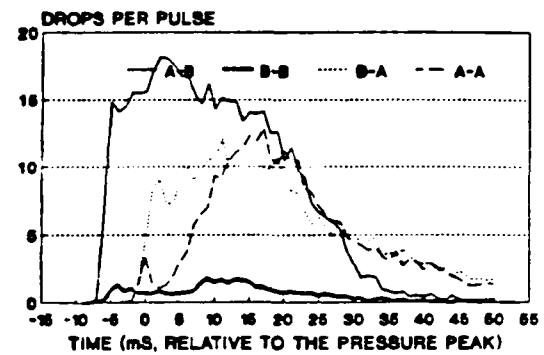


Comparison of 14ms symmetric, gentle TE, and steep TE pulses at location B-A

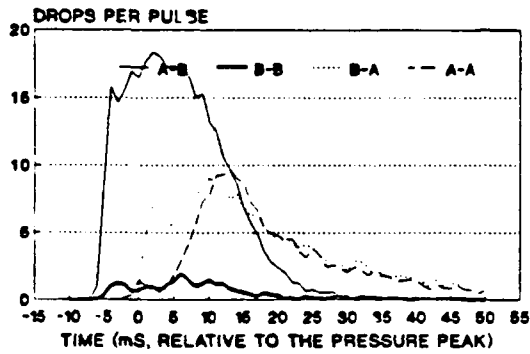
Figure 3.3.3 Time evolution of the Sauter mean diameter for different pressure waveforms and



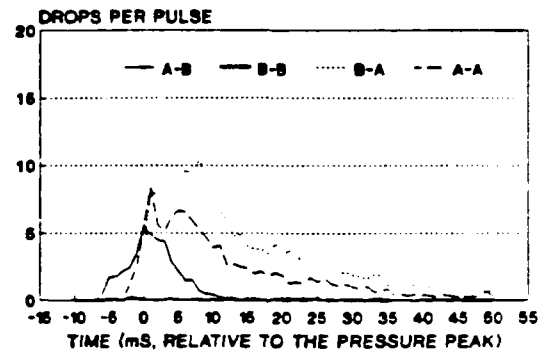
6, 14, and 16ms symmetric pulses at location B-A



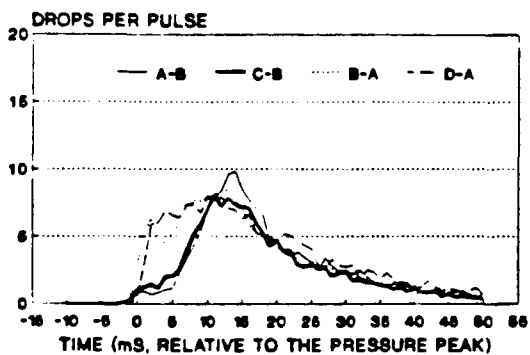
Gentle TE pulses at locations A-B, B-B, B-A, and A-A



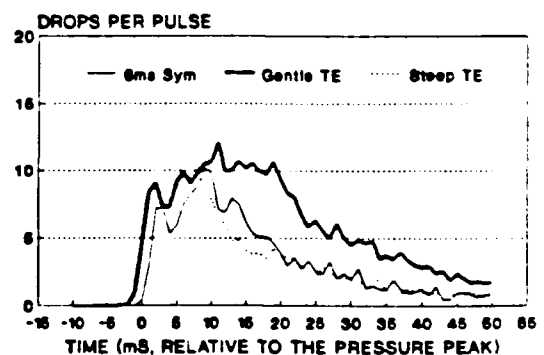
16ms symmetric pulses at locations A-B, B-B, B-A, and A-A



Steep TE pulses at A-B, B-B, B-A, and A-A

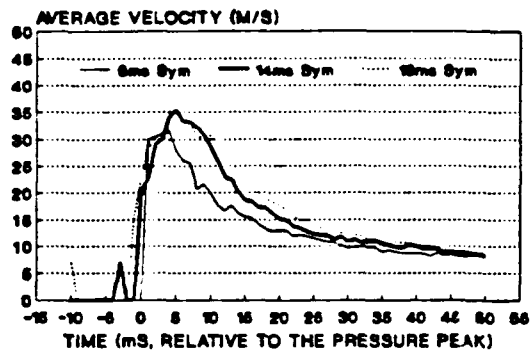


16ms symmetric pulses at locations A-A, C-A, B-A, and D-A

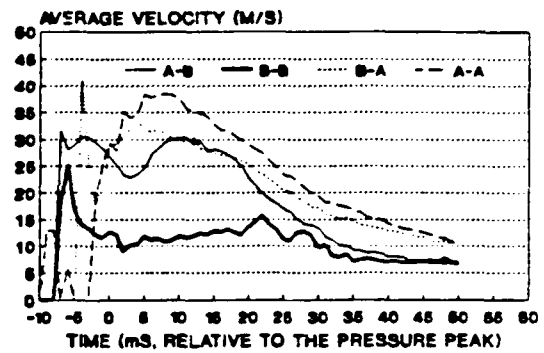


Comparison of 14ms symmetric, gentle TE, and steep TE pulses at location B-A

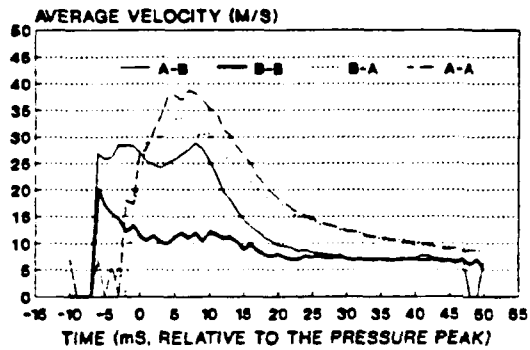
Figure 3.3.4 Time evolution of the average drops/pulse recorded for different pressure waveforms and different sampling locations.



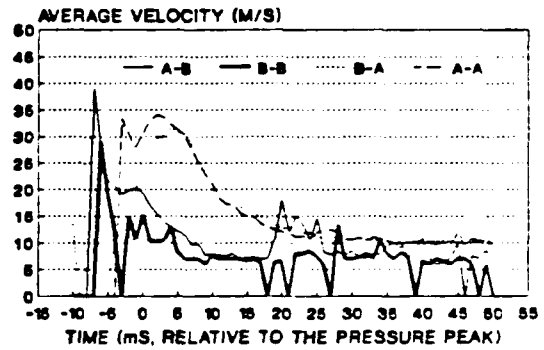
6, 14, and 16ms symmetric pulses at location B-A



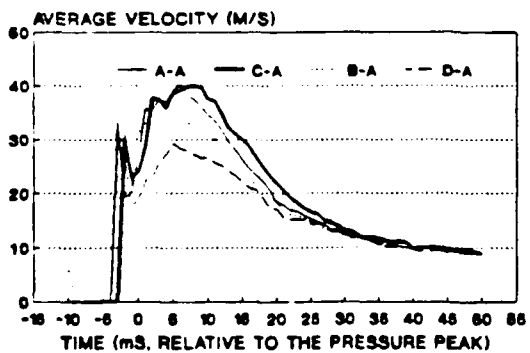
Gentle TE pulses at locations A-B, B-B, B-A, and A-A



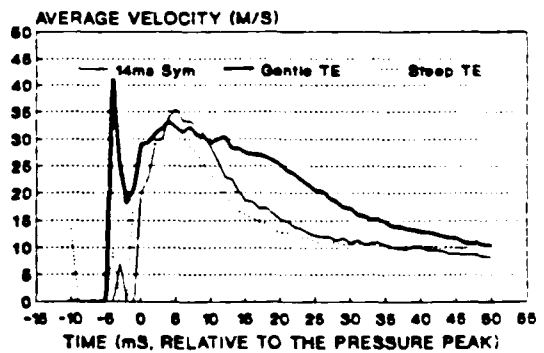
16ms symmetric pulses at locations A-B, B-B, B-A, and A-A



Steep TE pulses at A-B, B-B, B-A, and A-A

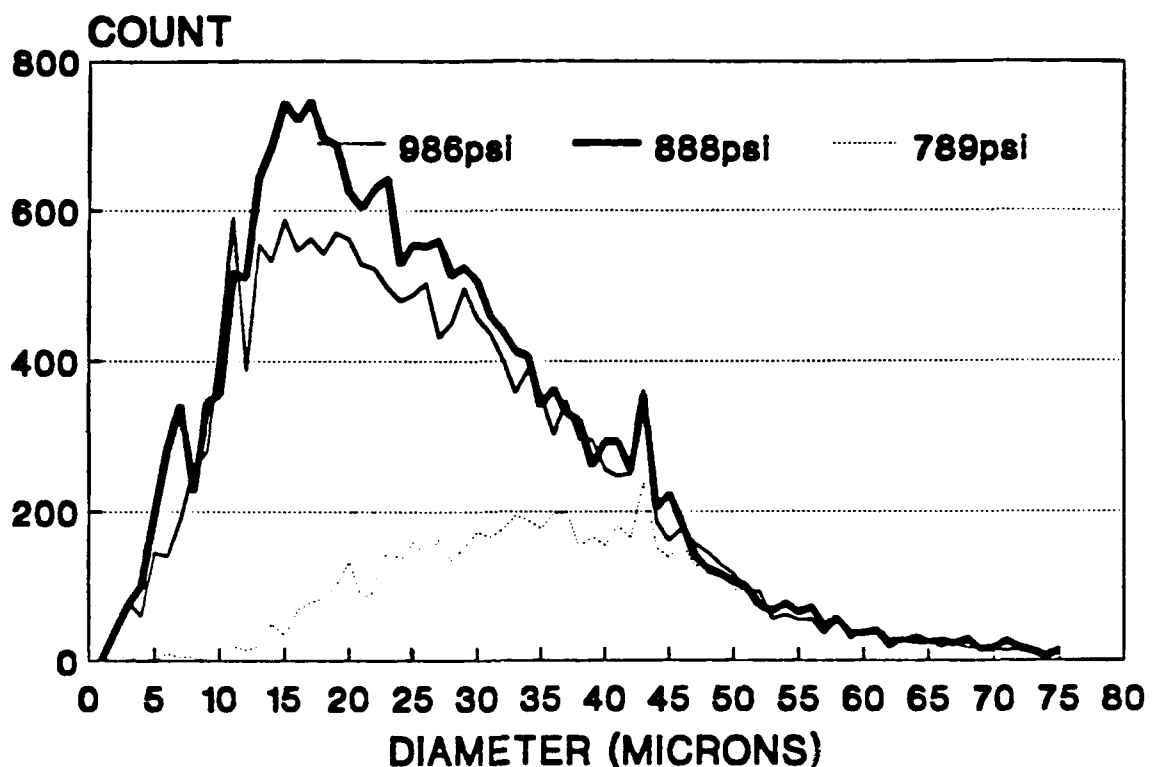


16ms symmetric pulses at locations A-A, C-A, B-A, and D-A

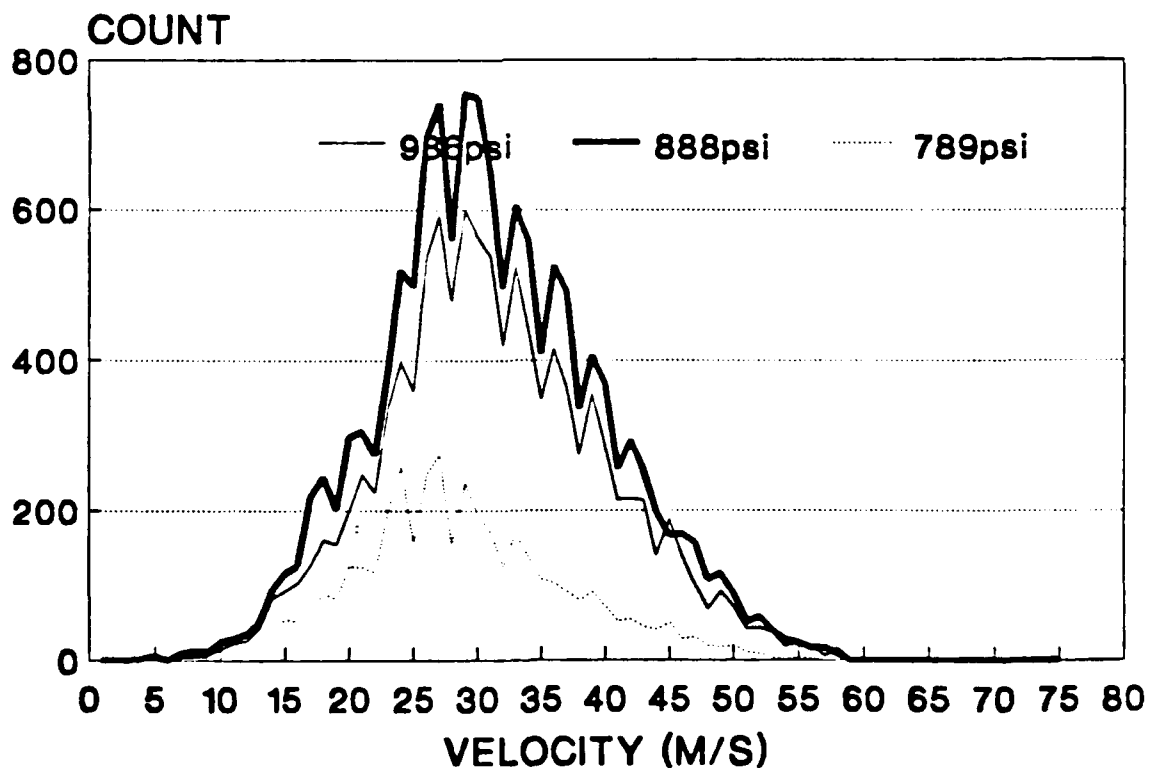


Comparison of 14ms symmetric, gentle TE, and steep TE pulses at location B-A

Figure 3.3.5 Time evolution of the velocity recorded for different pressure waveforms and different sampling locations.



(a)



(b)

Figure 3.4.1 Continuous 789, 888, and 986 psi nozzle pressure spray drop size (a) and drop velocity (b) distribution.

# Chapter 4

## Discussion

### 4.1 OBSERVED TRENDS

Many trends in the spray characteristics produced by different nozzle pressure waveforms are identified from the results presented in Chapter 3. These trends show the influence of a dynamic pressure input upon the drop size and velocity distributions, as well as the propagation of the drops from the nozzle.

Comparing the time-integrated drop size distributions at location B-A (see figure 3.1.1), three drop size ranges are considered. The production of 0 to 10 micron drops is not dependent upon the pressure waveform since all of the distributions are nearly the same in this range. From 10 to 20 microns, where each distribution peaks, drop production is quite dependent upon the pressure waveform. In the largest size drops, from 20 to 75 microns, the differential in drop production between the different pressure waveforms is consistent with injection duration. That is, the longer the duration of the pulse the more large size drops are produced.

Location B-A was used to make comparisons between the various nozzle pressure waveforms. All of the time-integrated size distributions at this location show that drops in the 10 to 20 micron diameter range were produced the most. The common feature

of each pressure waveform was a peak pressure of approximately 986 psi. Thus, it is generalized that this particular nozzle will produce mainly drops in the 10 to 20 micron diameter range when the peak pressure reaches approximately 986 psi (maintaining identical fluid and temperature) for any pressure waveform.

Among symmetric pulses, the connection between peak pressure and production of drops in the 10 to 20 micron size range is reinforced. Since the symmetric pulses were nearly sinusoidal, the period of time the pressure remains near peak is determined by the period of the pulse. Longer symmetric pulses have a longer period near peak pressure; thus, these pulses should produce more drops in the 10 to 20 micron range. In fact, the symmetric waveform with the longest duration, the 16 ms pulse, produced the most drops within this range. Likewise, the opposite is also observed. The shortest pulse (6 ms) produced the least drops in this range.

Comparing the symmetric pulse with the two asymmetric pulses also supports the link between peak pressure and production of drops in the 10 to 20 micron size range. The Gentle TE pulse clearly has the longest period near peak pressure (see figure 2.5.1), and it has the highest production of drops in this range. The distribution for the Steep TE pulse shows more drops in this size range than the 14 ms Symmetric pulse, but neither has an observable difference in pulse shape near peak pressure.

A link is made between the production of larger drops and the trailing pressure function in the nozzle. The sharp decline in nozzle pressure after the peak reduces the number large drops found at downstream location B-A. Comparing the 14 ms Symmetric with the two asymmetric pulses, the Steep TE pulse has the fewest drops in the largest size range. The sharp pressure decline in the Steep TE pulse reduces the period of injection where larger drop production is established.

It may also be true that a sharp rise in pressure to the peak also reduces the number of large drops found at downstream location B-A. Comparing the symmetric pulses,

the 6 ms pulse has the fewest drops in the larger sizes, but this does not necessarily prove that a sharp decline in trailing nozzle pressure produces less large drops as stated in the previous paragraph. The leading pressure function matches the trailing pressure function with symmetric pulses. Thus, a sharp rise in pressure may also mean less large drops are produced. A sharp rise in pressure certainly would reduce the period where production of large drops could take place at the onset of injection, and may inhibit the production.

A one and two-dimensional spatial comparison is made from the time-integrated drop size distributions. The four primary locations A-A, A-B, B-B, B-A are intended to give a global indication of spray activity. The two additional locations C-A and D-A for the 16 ms Symmetric pulse in combination with A-A and B-A give more detailed insight into spray activity along a radial line from the axis of the spray.

Location A-B is closest to the nozzle exit. The time-integrated size distributions vary with the input pressure waveform. Both the 16 ms Symmetric and Gentle TE pulses, which have relatively long durations, produce their largest distributions at this location. There are two size ranges present in these distributions, 0-22 microns and 22-45 microns. The smaller range is the peak range; while the larger range is a broad plateau.

The Steep TE pulse produced a relatively low distribution at A-B compared with its distributions downstream. The sharp cutoff in pressure of the Steep TE waveform does not allow the liquid jet to breakup as effectively until further downstream.

Very few drops are found at location B-B for any pressure waveform. This location is radial to A-B, and the lack of drops indicates that the spray angle is less than 9°. However, a few drops of all sizes are found there, probably due to recirculation or sputtering from the nozzle face.

Downstream, at locations A-A and B-A, the distribution profiles are similar for all pressure waveforms. However, more drops are found in the outer location B-A. A comparison of radial locations is made for the 16 ms Symmetric pulse, which helps clarify this observation.

We see from the radial comparison of sampling locations a step-like difference between the time-integrated size distribution at C-A and the one at B-A. A higher number of drops in the peak range for the outer locations is the difference. That is, there are more small drops in the outer locations than in the inner two locations. It is difficult to conclude why we see this trend. Since figure 3.4.4 shows that the bulk of the drops arriving at outer location B-A before the inner location A-A, more of the drops at B-A must be from the increasing nozzle pressure. The spray cone must be expanding to the point where more drops are found in the periphery than along the axis by the time the spray reaches the downstream distance of locations A-A and B-A.

These radial locations are also used to give an idea of the total drop size distribution of the spray. Figure 3.2.1 totals the drops from locations A-A, C-A, B-A, and D-A for a coarse representation of the distribution which might be expected from a complete cross-sectional sampling. The distribution closely resembles the distribution for the constant 888 psi spray (see figure 3.4.1).

The time-integrated size distributions are supplemented by time-integrated velocity distributions (see figure 3.1.2). As reported in the results section, these velocity distributions were bimodal at all downstream locations, broad at location A-B, and sharply peaked at location B-B.

The bimodal velocity distributions taken alone are hard to decipher. However, they point out that something is taking place between upstream location A-B and the downstream locations, since the distribution is not bimodal at A-B. One possible explanation is that a denser sheet of drops moves out radially downstream. It then col-

lapses as the pressure declines. The sheet passes the sampling locations downstream twice with different average velocities each time.

Another explanation of the bimodal velocity distributions downstream is that coalescence produces a peak. Smaller drops pass through the sampling region with a high average velocity producing one peak. However, significant coalescence may also produce a sub-group of drops with a lower average velocity resulting in another peak.

The time-integrated velocity distribution at B-B is not bimodal for any pressure waveform. There is one sharp peak at approximately 8 m/s. Thus, these drops are probably recirculating or freefall as previously mentioned.

In contrast to the time-integrated distributions, the time-resolved distributions give an evolutionary picture of the injection event. Since there is some distance from the nozzle pressure sampling location and the drop sampling locations, there is no direct link between instantaneous pressure and instantaneous drop distribution characteristics. However, we can make some observations of the instantaneous drop distribution characteristics, and draw some conclusions.

There is a pattern consistent through all of the Sauter mean diameter (d<sub>32</sub>) graphs (see figure 3.3.3). The d<sub>32</sub> generally stays within a range of 0 to 50 microns. Dramatic fluctuations of d<sub>32</sub> occur during periods where there are few drops. These fluctuations probably represent both the inconsistent drop size production and statistical inadequacies of low drop numbers. Comparison of the d<sub>32</sub> graphs with their respective drops per pulse graph shows that the d<sub>32</sub> is most stable during the period of high drop per pulse rates.

A distinct minimum d<sub>32</sub> occurs during the stable period. Since there is a time lag between the pressure waveform and the events downstream in the spray, it is difficult to link the two observations. However, this minimum d<sub>32</sub> occurs with the peak aver-

age velocity. Since the average velocity follows the input pressure, we conclude that the  $d_{32}$  has an inverse relationship with pressure.

The Sauter mean diameter at location B-A downstream stays within 35-45 microns during the stable period for each of the tested pressure waveforms. Upstream, near the spray axis (A-B),  $d_{32}$  was smaller than either of the sample locations downstream. Radial sample locations downstream showed no significant variation in the  $d_{32}$  pattern. Smaller drops at upstream location A-B rather than downstream at A-A and B-A indicates that coalescence is taking place axially.

The time-evolution of the drops per pulse is an indicator of spray activity and/or density in the sample region. In general the drops per pulse level rises very fast, levels out, then falls quickly for a short time, and finally falls slowly towards zero. The longer the pulse, the longer the period where the drops per pulse remain at a high level.

Significant numbers of drops arrive downstream in the near axial sampling location A-A later than in the outer location B-A. Then 20 ms after the pressure peak the number of drops occurring in radial positions A-A, C-A, B-A, and D-A appears equal. Note that drop sizes are at their lowest at this time and velocity has leveled off to 9 m/s. Thus, these are probably free-fall drops that are recirculating, since they are smaller than Rayleigh mode drops.

Earlier we discussed the bimodal time-integrated velocity distributions at locations A-A and B-A. When we look at the time-resolved evolution of average drop velocity in figure 3.3.5, we see bimodal characteristics at the upstream location A-B and downstream location A-A. This supports the previous idea that the propagation of the spray is in the form of a dense sheet moving outward radially and then collapsing.

## 4.2 CORRELATION TO CONTINUOUS SPRAY

Using the previous assumption that the minimum in the evolution of the Sauter mean diameter for intermittent sprays results from the maximum nozzle pressure, we see that Sauter mean diameter of the continuous spray at 888 and 986 psi (see figures 3.4.1) match Sauter mean diameters in the intermittent sprays (see figure 3.3.3) at similar pressures. Moreover, the corresponding average drop velocities also match.

Note that the Sauter mean diameter dramatically increases and the mean velocity decreases in the nozzle pressure drop from 888 to 789 psi in the continuous jets. Yet, there is no appreciable change in the spray characteristics between the 888 and 986 psi.

Looking at the intermittent sprays for a similar change as the pressure increases or decreases from approximately 900 to 800 psi is difficult because no direct time phase relationship is established between pressure sampling and drop sampling. However, in general we do not see the dramatic change in size during the evolution of the intermittent sprays. There does seem to be a characteristic steep decline in average velocity following the peak plateau in the evolution of average velocities for intermittent sprays.

## 4.3 SPECIAL OBSERVATION

There is a characteristic peak of drops produced at 43 microns which shows up in the time-integrated drop size distributions of the intermittent sprays (see figures 3.1.1 and 3.2.1). This peak is very narrow in size range and is typically 25% greater than adjacent size ranges. It is clear that the nozzle produces this drop size with greater efficiency than others. Since the spike occurs with every pressure waveform there must be a common condition that occurs with each waveform, or the spike is not waveform dependent. Since see the spike in the continuous pressure size distributions (see fig. 3.4.1), we can conclude that the spike is not a function of a dynamic pressure input.

Interestingly, this spike is very close the Sauter Mean Diameter of the 888 and 986

psi continuous sprays. It seems that the nozzle has an optimum efficiency at 45 microns for continuous sprays. The dynamic pressure inputs, although reaching a peak pressures similar to the continuous sprays, shift the efficiency to the smaller 10-20 micron range.

Going back to theory [16], the growth of many disturbances of different frequencies is responsible for atomization with one frequency dominating. In the identification of the spike at 43 microns, it was also mentioned that there were other spikes present. The dynamic pressure inputs must enhance a competing frequency in order to overwhelm the geometrically advantaged frequency producing 43 micron drops, since it produces 10-20 micron drops primarily.

# Chapter 5

## Conclusion

In the field of intermittent liquid jets, there is a definite influence on the drop sizes and velocities by a dynamic pressure input to the nozzle. This study shows that by changing the ascent and decline of the nozzle pressure, while maintaining the same peak pressure, different results are achieved. Moreover, these results vary from just a simple change in injection volume. There are changes in the spray drop size and velocity distributions.

In addition, evidence has been presented which indicates the nozzle used can produce one drop size with greater efficiency than other sizes at high injection pressures. In particular, the appearance of the 43 micron drop size spike warrants investigation. Further work may validate theories predicting a disturbance of a given frequency that will dominate atomization under the conditions used. To do continue on this line of study requires the measurement of instantaneous flow rate which was unavailable for this work. Instantaneous flow rate would give instantaneous average velocity across the nozzle exit; thus, a Reynold's number could be computed.

The broad nature of this work lends itself very well to more detailed studies. There are two directions in which to explore. The first direction is to study the influ-

ence of the nozzle pressure waveform with more variation. The second is to explore the spray produced with a given waveform with more resolution. Exploring both simultaneously is not recommended since the amount of data would prohibitive.

The nozzle pressure waveform should be varied both in form and maximum amplitude. It is not clear what influence the rise in pressure has upon the spray characteristics. This study could only vary the rise while varying the fall, the symmetric case. Furthermore, different declining pressure profiles are now required to quantify and define their influence. Changing the maximum pressure amplitude may change the whole issue. The maximum pressure used in this study is between low pressure gasoline injection and high pressure diesel injection. Therefore, these limits must be explored for practical application.

Resolving a particular spray in higher detail is important to the validation of future theories and models regarding intermittent injections. The time-resolution of the Aerometric's PDPA system is more than adequate for resolving all of the drops passing the sample location at a given time. However, the time-resolution of pressure should be improved along, and instantaneous injection rate should be monitored. In addition, more sampling locations are needed to completely map the spray and its propagation, verify its symmetry, and give better global estimates of the distributions for the injection both time-integrated and time-resolved.

## References

- [1] Kuniyoshi, H., Tanabe, H., Sato, G., and Fujimoto, H. "Investigation on the Characteristics of Diesel Fuel Spray." SAE Paper No. 800968.
- [2] Takeuchi, K., Senda, J., and Shikuya, M. "Transient Characteristics of Fuel Atomization and Droplet Size Distribution in Diesel Fuel Spray." SAE Paper No. 830449.
- [3] Sangeorzan, B., Uyehara, O., and Myers, P. "Time-Resolved Drop Size Measurements in an Intermittent High Pressure Fuel Spray." SAE Paper No. 841361.
- [4] Shaoxi, S., Yunyi, G., and Hulmin, S. "Experimental Study of the Atomization and Evaporation Processes of Diesel Fuel Sprays." SAE Paper No. 881253.
- [5] Koo, J. and Martin, J. "Droplet Sizes and Velocities in a Transient Diesel Fuel Spray." SAE Paper No. 900397.
- [6] Glikin, P. "Fuel Injection in Diesel Engines." Proceedings of the Institute of Mechanical Engineers, Vol. 199 No. D3, 1985, pp161-174.
- [7] Dolenc, A. "The Injection Equipment of Future High-Speed DI Diesel Engines with Respect to Power and Pollution Requirements." Proceedings of the Institute of Mechanical Engineers, Vol. 199 No. D3, 1990, pp49-58.
- [8] Ficarella, A., Laforgia, D., and Cipolla, G. "Investigation and Computer Simulation of Diesel Injection System with Rotative Pump." Journal of Engineering for Gas Turbines and Power, Vol. 112, July 1990, pp317-323.
- [9] Yamaguchi, J. "Two-Stage Injector Reduces DI Diesel Noise." Automotive Engineering, Sept. 1988, pp82-84.
- [10] Freudenschub, O., Herdin, G., Schreiner, E., and Schmidt, H. "Fuel Injection Nozzle for Combustion Engines." US Pat. No. 4,715,541, Dec. 29, 1987.
- [11] Sinnamon, J., Lancaster, D., and Steiner, J. "An Experimental and Analytical Study of Engine Fuel Spray Trajectories." SAE Paper No. 800135.

- [12] Ruiz, F. and Chigier, N. "The Effects of Design and Operating Conditions of Fuel Injectors on Flow and Atomization." SAE Paper No. 870100.
- [13] Arai, M., Tabata, M., Hiroyasu, H., and Shimizu, M. "Disintegrating Process and Spray Characterization of Fuel Jet Injected by a Diesel Nozzle." SAE Paper No. 840275.
- [14] Chehroudi, B., Chen, S., Bracco, F., and Onuma, Y. "On the Intact Core of Full-Cone Sprays." SAE Paper No. 850126.
- [15] Woods, D. "Production of Sub-Micron Monodispersed Droplets from a Liquid Jet." Clarkson University, MAE Department, Masters Thesis, April 27, 1990.
- [16] Lin, S. P., and Lian, Z. W., "Mechanism of the Breakup of Liquid Jets." AIAA Journal. 1988, 28: 120-126.

## Appendix A

# Computer Programs

### A.1 ANALYSIS OF DATA FOR LOCAL PRESSURE PEAKS

This program reads through the pressure data (in volts) and finds local pressure peaks. Each local pressure peak represents one injection.

Since the time resolution of the data is 1 ms, it is probable that the actual pressure peak occurs between samples. An interpolated value is computed from the recorded peak and its two neighboring samples. This interpolated peak is used to estimate the actual peak. A second order polynomial is used.

The time of the recorded peak, the estimated peak, and their time offset from the recorded peak are then saved for each peak.

The conversion from volts to psi is done by the graphing software (Harvard Graphics), not in this program. The conversion is a simple, linear multiplier (1 mv = 986 psi).

**PROGRAM T1**

```
REAL RED1(2,20001),PPEAK,PEAKIN(3,500)
LOGICAL GOOD,GO,FOUND,STOP

OPEN (UNIT=1,FILE='C:\DATA4\RAWP4.CON')
OPEN (UNIT=3,FILE='C:\DATA4\RED4\PEAK.DAT')
```

```

STOP=.TRUE.
I=1
BSUM=0.0
ISUM=0
WHILE (STOP) DO
    READ (1,* ,IOSTAT=IOS)RED1(1,I),RED1(2,I)
    IF (IOS .EQ. 0) THEN
        IF (RED1(2,I) .GE. 2) THEN
            PRINT *, 'LOOK', I,RED1(2,I)
            STOP
        END IF
        IF (RED1(2,I).LE. - . .) THEN
            BSUM=BSUM+RED1(2,I)
            ISUM=ISUM+1
        END IF
    ELSE
        STOP=.FALSE.
    END IF
    I=I+1
END WHILE
JMAX=I-2

THRESH=.1

* INTERPOLATE PEAKS
NUMPTS=0
NUMPKS=1
VPEAK=RED1(2,1)
IPEAK=RED1(1,1)
IND=1
GOOD=.FALSE.
DO 5 J=2,JMAX
    IF (RED1(2,J) .GE. THRESH) THEN
        GOOD=.TRUE.
        IF (RED1(2,J) .GT. VPEAK) THEN
            VPEAK=RED1(2,J)
            IPEAK=RED1(1,J)
            IND=J
        END IF
        NUMPTS=NUMPTS+1
    ELSE
        IF (VPEAK .EQ. RED1(2,J-1)) GOOD=.FALSE.
        IF (VPEAK .EQ. RED1(2,J-NUMPTS)) GOOD=.FALSE.
        IF ((GOOD) .AND. (NUMPTS .GE. 5)) THEN
            F0=RED1(2,IND-1)
            C1=RED1(2,IND)-F0
            F1T1=F0+2*C1
            C2=(RED1(2,IND+1)-F1T1)*.5
            TPEAK=-(1+C1/C2)*.5
            PPEAK=F0+C1*(TPEAK+1)+C2*TPEAK*(TPEAK+1)
    * RECORDED PEAK INDEX IN RED1.DAT
        PEAKIN(1,NUMPKS)=RED1(1,IND)
    * OFFSET BETWEEN RECORDED PEAK TIME AND INTERPOLATED
    * (-) MEANS INTERPOLATED PEAK COMES FIRST

```

```

        PEAKIN(2,NUMPKS)=TPEAK
*     INTERPOLATED PEAK
        PEAKIN(3,NUMPKS)=PPEAK
        NUMPKS=NUMPKS+1
        GOOD=.FALSE.
        END IF
        VPEAK=RED1(2,J)
        TPEAK=RED1(1,J)
        IND=J
        NUMPTS=0
        END IF
5     CONTINUE
        WRITE (3,*)NUMPKS-1

        DO 6 I=1,NUMPKS-1
            WRITE (3,*)PEAKIN(1,I),PEAKIN(2,I),PEAKIN(3,I)
6     CONTINUE

        STOP
        END

```

## A.2 TABULATING DROP SIZE AND VELOCITY DATA

This program reads through the list of local pressure peaks created by program T1 (see Appendix A.1) and tabulates drop size and velocity information in a predefined time window (injection event) around the pressure peak.

The correction factors for Gausian Errors are applied to the final distributions in this program. A list of correction factors is computed using program T7 (see Appendix A.4).

### PROGRAM T2

```

REAL CORFAC(76)
INTEGER ISTORE(120,101),ISTOR3(120,101),
+      IDROPS(120),ITOT(76),IDROPV(120)
LOGICAL GOOD,STOP1,STOP2

OPEN (UNIT=1,FILE='C:\DATA4\RED4\PEAK.DAT')
OPEN (UNIT=2,FILE='C:\DATA4\RED4\DISTR1.DAT')
OPEN (UNIT=3,FILE='C:\PDPA\PDPPDATA\6292\1\RUN04\PDPPARAW.TXT')
OPEN (UNIT=10,FILE='C:\DATA4\RED4\VELDISTR.DAT')
OPEN (UNIT=4,FILE='C:\DATA4\RED4\CORFACT.DAT')

DO 4 I=1,120
    DO 3 J=1,101
        IF (I .LE. 120) ISTORE(I,J)=0
        IF (I .LE. 120) ISTOR3(I,J)=0

```

```

3      CONTINUE
      IF (I .LE. 75) ITOT(I)=0
      IDROPV(I)=0
4      CONTINUE

      DO 5 I=1,75
          READ (4,*)IDUM1,CORFAC(I)
5      CONTINUE

      READ (3,*)
      READ (1,*)NUMPKS,DUMMY
      NUMPKS=NUMPKS-1
      STOP1=.TRUE.
      IDROP=1
      ICOUNT=1
      WHILE (STOP1) DO
          READ (1,*)RTIME,DUMMY,VOLT
          ITIME=RTIME
          IF (ICOUNT .EQ. NUMPKS) STOP1=.FALSE.
          IF ((VOLT .GE. .95) .AND. (VOLT .LT. 1.05)) THEN
              ISTART=ITIME-10
              ISTOP=ITIME+50
              STOP2=.TRUE.
              WHILE (STOP2) DO
2              READ (3,*,IOSTAT=IOS)R1,R2,R3,R4,R5
              IT=INT(R5*1000)
              IF ((IT .LT. ISTART) .AND. (IOS .EQ. 0)) GOTO 2
              IF ((IT .GE. ISTART) .AND. (IT .LE. ISTOP)) THEN
                  ISIZE=INT(R1)
                  IVEL=INT(R2)
                  ITR=IT-ISTART+1
                  ISTORE(ITR,ISIZE)=ISTORE(ITR,ISIZE)+1
                  IF ((IVEL .LT. 76) .AND. (IVEL .GT. 0))
+                      ISTOR3(ITR,IVEL)=ISTOR3(ITR,IVEL)+1
                  ISTORE(100,ITR)=ISTORE(100,ITR)+1
                  ISTORE(100,62)=ISTORE(100,62)+1
              END IF
              IF ((IT .GT. ISTOP) .OR. (IOS .NE. 0)) STOP2=.FALSE.
              IF (IOS .NE. 0) STOP1=.FALSE.
          END WHILE
          IDROP=IDROP+1
      END IF
      ICOUNT=ICOUNT+1
  END WHILE

  DO 15 I=1,61
  DO 14 J=1,75
      ISTORE(I,J)=ISTORE(I,J)*CORFAC(J)
14  CONTINUE
15  CONTINUE

  SUMI=C
  DO 7 I=1,61
      IDROPS(I)=0

```

```

      DO 6 J=1,75
          ITOT(J)=ITOT(J)+ISTORE(I,J)
          DNORM=ISTORE(I,J)/(IDROP-1.0)
      *
          WRITE (2,*) J, DNORM
          IDROPS(I)=IDROPS(I)+ISTORE(I,J)
      6    CONTINUE
      *
          WRITE (2,*) 
          SUMI=SUMI+IDROPS(I)
      7    CONTINUE

      DO 11 I=1,61
          DO 10 J=1,75
              VNORM=ISTOR3(I,J)/(IDROP-1.0)
              IDROPV(J)=IDROPV(J)+ISTOR3(I,J)
      *
              WRITE (10,*) J, VNORM
      10   CONTINUE
      11   CONTINUE

      ARNUM=0
      ARDEN=0
      SANUM=0
      SADEN=0
      VENUM=0
      VEDEN=0

      DO 13 I=1,61
          DO 12 J=1,75
              ARNUM=ARNUM+ISTORE(I,J)*J
              ARDEN=ARDEN+ISTORE(I,J)
              SANUM=SANUM+ISTORE(I,J)*J**3
              SADEN=SADEN+ISTORE(I,J)*J**2
              VENUM=VENUM+ISTOR3(I,J)*J
              VEDEN=VEDEN+ISTOR3(I,J)
      12    CONTINUE
      ARMEAN=0
      SAMEAN=0
      VEMEAN=0
      IF (ARDEN .NE. 0.0) ARMEAN=ARNUM/ARDEN
      IF (SADEN .NE. 0.0) SAMEAN=SANUM/SADEN
      IF (VEDEN .NE. 0.0) VEMEAN=VENUM/VEDEN
      ARNUM=0
      ARDEN=0
      SANUM=0
      SADEN=0
      VENUM=0
      VEDEN=0
      DNORM=IDROPS(I)/(IDROP-1.0)
      WRITE (2,*) ARMEAN, SAMEAN, DNORM
      WRITE (10,*) I, VEMEAN
      13 CONTINUE
      WRITE (2,*) SUMI

      DO 20 J=1,75
          DNORM=ITOT(J)/(IDROP-1.0)

```

```

        VNORM=IDROPV(J)/(IDROP-1.)
        WRITE (2,*)J,DNORM
        WRITE (10,*)J,VNORM
*      20  CONTINUE

        STOP
        END

```

### A.3 ANALYSIS OF PRESSURE WAVEFORMS

This program calculates average pressure waveforms for each of the pressure waveforms used. In addition, a standard deviation is computed for each time point in a given pressure waveform. The standard deviation measures how well any individual pressure curve might compare to the average at a given time point.

```

PROGRAM T6
*
REAL STORE(120),STORE1(120)
LOGICAL GOOD,STOP1,STOP2

OPEN (UNIT=1,FILE='C:\DATA4\RED10\PEAK.DAT')
OPEN (UNIT=3,FILE='C:\DATA4\RAWP10.CON')
OPEN (UNIT=2,FILE='C:\DATA4\RED10\PRESS.DAT')
OPEN (UNIT=4,FILE='C:\DATA4\RED10\PRSTAT.DAT')

READ (2,*)
DO 4 I=1,41
    READ (2,*)DUM,STORE(I)
    STORE1(I)=0.0
4   CONTINUE

READ (3,*)
READ (1,*)NUMPKS
READ (1,*)RTIME,ADJ,VOLT
NUMPKS=NUMPKS-1
STOP1=.TRUE.
IDROP=1
ICOUNT=1
WHILE (STOP1) DO
    READ (1,*)RTIME,ADJ,VOLT
    ITIME=RTIME
    IF (ICOUNT .EQ. NUMPKS) STOP1=.FALSE.
    IF ((VOLT .GE. .95) .AND. (VOLT .LT. 1.05)) THEN
        WRITE (4,*)RTIME,VOLT
        ISTART=ITIME-10
        ISTOP=ITIME+30
        STOP2=.TRUE.
        READ (3,*)VOL
        IF (ADJ .LE. 0.) THEN

```

```

        VVOLTP=0.
        WHILE (STOP2) DO
2          READ (3,*,IOSTAT=IOS)TIME,VVOLT
          IT=TIME
          IF ((IT .LT. ISTART) .AND. (IOS .EQ. 0)) GOTO 2
          IF ((IT .GE. ISTART) .AND. (IT .LE. ISTOP)) THEN
            ITR=IT-ISTART+1
            ADVOLT=(VVOLT-VVOLTP)*(1.-ADJ)+VVOLTP
            IF (IT .EQ. ISTART+10) ADVOLT=VOLT
            STORE1(IIR)=STORE1(IIR)+(ADVOLT-STORE(IIR))**2
          END IF
          IF ((IT .GT. ISTOP) .OR. (IOS .NE. 0)) STOP2=.FALSE.
          IF (IOS .NE. 0) STOP1=.FALSE.
          VVOLTP=VVOLT
        END WHILE
      ELSE
        READ (3,*)TIME,VVOLT
        WHILE (STOP2) DO
6          READ (3,*,IOSTAT=IOS)TIMEA,VVOLTA
          IT=TIME
          IF ((IT .LT. ISTART) .AND. (IOS .EQ. 0)) THEN
            TIME=TIMEA
            GOTO 6
          END IF
          IF ((IT .GE. ISTART) .AND. (IT .LE. ISTOP)) THEN
            ITR=IT-ISTART+1
            ADVOLT=(VVOLTA-VVOLT)*(ADJ)+VVOLT
            IF (IT .EQ. ISTART+10) ADVOLT=VOLT
            STORE1(ITR)=STORE1(ITR)+(ADVOLT-STORE(ITR))**2
          END IF
          IF ((IT .GT. ISTOP) .OR. (IOS .NE. 0)) STOP2=.FALSE.
          IF (IOS .NE. 0) STOP1=.FALSE.
          VVOLT=VVOLTA
          TIME=TIMEA
        END WHILE
      END IF
      IDROP=IDROP+1
    END IF
    ICOUNT=ICOUNT+1
  END WHILE

  WRITE (4,*)IDROP-1
  DO 7 I=1,41
    DNORM=SQRT(STORE1(I)/(IDROP-1.0))
    WRITE (4,*)I, DNORM
7  CONTINUE

  STOP
END

```

#### A.4 CALCULATION OF CORRECTION FACTORS

This program reads the corrected and uncorrected distributions created by the

PDPA software and calculates the correction factors used. The correction factors are then used to create the list of correction factors for the different size groups in the custom distributions.

```
PROGRAM CORREC
*   CALCULATION OF CORRECTION FACTORS TO BE USED WITH CUSTOM
*   DISTRIBUTIONS.

REAL STORE(3,76)
INTEGER CORVAL

OPEN (UNIT=2,FILE='C:\PDPA\PDPPDATA\6292\1\RUN23\PDPPDATA.TXT')
OPEN (UNIT=1,FILE='C:\DATA4\RED23\CORFACT.DAT')

DO 4 I=1,3
DO 3 J=1,75
    STORE(I,J)=0
3  CONTINUE
4  CONTINUE

DO 5 I=1,72
    READ (2,*)
5  CONTINUE

DO 6 I=1,50
    READ (2,*)IDUM1,STORE(1,I),STORE(2,I)
6  CONTINUE

READ (2,*)
READ (2,*)

DO 7 I=1,50
    READ (2,*)IDUM1,DUM2,CORVAL
    IF (STORE(2,I) .NE. 0.) STORE(2,I)=CORVAL/STORE(2,I)
7  CONTINUE

J=1
STORE(3,1)=STORE(2,J)
WRITE (1,*)J,STORE(3,J)
DO 8 I=2,75
    AVBETW=(STORE(1,J)+STORE(1,J+1))/2.
    IF (I .LE. AVBETW) J=J
    IF (I .GT. AVBETW) J=J+1
    STORE(3,I)=STORE(2,J)
    WRITE (1,*)I,STORE(3,I)
8  CONTINUE

STOP
END
```

**"Mechanism of Intermittent Atomization"**

This research project seeks a complete knowledge of the physical mechanism of the formation of intermittent fuel sprays. The objective is to exploit this knowledge to enhance the efficiency of internal combustion engines, and to reduce the air pollution caused by inefficient combustion. The theoretical results (S.P. Lin 10th ARO Engine/Fuel Workshop, Proceedings pp. 120-131, Madison, Wisconsin, June 2-3, 1992) show that the droplet formation from the leading edge of the liquid fuel jet is caused by the Taylor-Lamb instability during the deceleration phase of the intermittent spray. The mechanism of droplet formation from the rest of the liquid-gas interface remains the same as that for the case of stationary atomization (S.P. Lin and Z.W. Lian, pp. 771-773, Physics of Fluids A, 1993). Since the leading edge interfacial area occupies only a small part of the total interfacial area, the atomization of intermittent sprays is still caused by the pressure fluctuation at the interface. However, this does not imply that the size distributions for stationary and intermittent sprays are the same. In fact the deceleration of the liquid jet tends to reduce the droplet diameter at the same pressure. To compare with the theory, the size and velocity distributions at various locations in a spray, as indicated in Fig. 2.41, are measured with an Aerometric Phase Doppler Particle Analyzer. The figure numbers refer to the figure numbers of the M.S. thesis of V. Cook (V.F. Cook, M.S. Thesis, Clarkson University, 1993). Fig. 3.3.3 gives the Sauter mean diameters at the location B-A as function of time for 3 different sprays with different forms of pressure pulse at the nozzle inlet. All 3 sprays have the same peak pressure. One spray has a symmetric pressure pulse of period 14 ms. The second spray designated with steep TE has a sudden pressure reduction after the pressure peak. The third spray designated with gentle TE has a gentle pressure reduction after the pressure peak. It can be seen that the Sauter mean diameter is the smallest on the average for the case of steep TE. This has profound practical implications. The corresponding size distributions are given in Fig. 3.1.1. Comparing the number of drops from the gentle-TE-spray and the steep-TE-spray in this figure, it is seen that the former spray produces more droplets than the latter one. Moreover the former produces relatively more smaller droplets than the latter. This indicates that the mechanisms of intermittent and stationary spray formation remain essentially the same. This is because the gentle TE spray has a larger velocity over the entire period of deceleration, and it is known (Z.W. Zhou and S.P. Lin, J. of Propulsion and Power, 8, pp. 736-740, 1992) that smaller droplets can be produced with larger jet velocities in stationary jets. To support this argument, the size distributions of an intermittent sprays at different times during the period of pulsation were measured and compared with the stationary spray data for different steady nozzle pressures. The latter data are given in Fig. 3.4.1a. The data for the intermittent spray are not given here, because of the lack of space. The comparison reveals that the shape of size distributions curve of an intermittent spray changes according to the change in pressure in the same manner as that for the stationary sprays. It can be shown theoretically that intermittent sprays, as far as the mechanism of droplet formation is concerned, remain quasi-steady unless the period of pulsation is less than 100-th of a ms for diesel fuel. However, finer sprays can be produced with a more sudden reduction in the nozzle inlet pressure after its peak during the injection period.

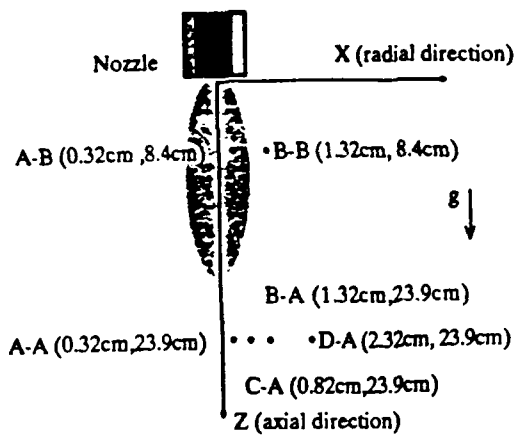
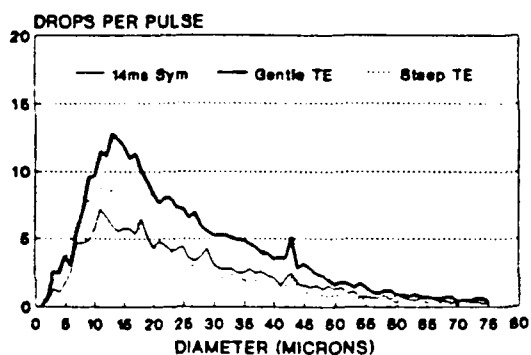
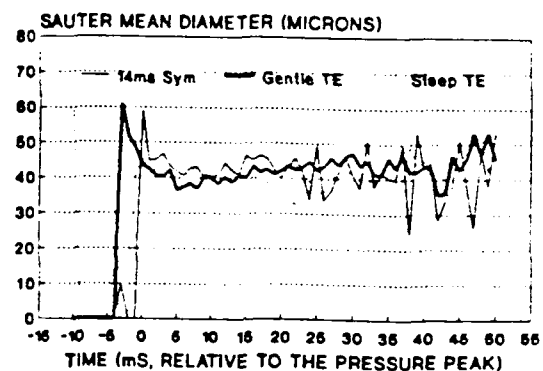


Figure 2.4.1 Spray sampling locations downstream of the nozzle.



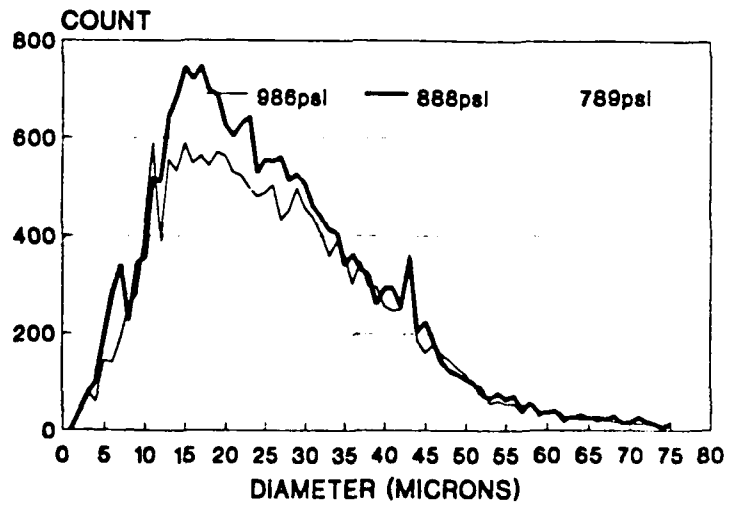
Comparison of 14ms symmetric, gentle TE, and steep TE pulses at location B-A

Figure 3.1.1 Time-integrated drop size distributions



Comparison of 14ms symmetric, gentle TE, and steep TE pulses at location B-A

Figure 3.3.3 Time evolution of the Sauter mean diameter



(a)

Figure 3.4.1 Continuous 789, 888, and 986 psi nozzle pressure spray drop size (a) and drop velocity (b) distributions.

The absolute and convective instability of a viscous liquid jet emanating into a viscous gas in a vertical pipe is analyzed in a parameter space spanned by the Reynolds number, the Froude number, the Weber number, the viscosity ratio, the density ratio, and the diameter ratio. The numerical results of the analysis are used to demonstrate that reduction in gravity tends to enhance the Rayleigh mode of convective instability which leads to the breakup of a liquid jet into drops of diameters comparable with the jet diameter. On the contrary, the Taylor mode of convective instability which leads to atomization is retarded at reduced gravity. The Rayleigh mode becomes absolutely unstable when the Reynolds number exceeds a critical value for a given set of the rest of the relevant parameters. The domain of absolute instability is significantly enlarged when the effect of gas viscosity is not neglected.

A new theory is developed for an intermittently atomizing jet emanating from a nozzle into a combustion chamber of finite dimension. The velocity and pressure fields in the nozzle, jet, and the chamber are described by Eulerian description. The description is translated into Lagrangian particle description at the liquid-gas interface. Thus, the computation domain is gridless but is rapidly increasing and decreasing with time. So far as the writer is aware, this is the first theory which is capable of revealing the atomization process in response to the pressure input. There are two major phases in intermittent atomization: acceleration and deceleration phases. During the acceleration phase, atomization initiates from the size of a jet. During the deceleration phase more droplets are formed from the penetrating front of the jet. The droplets formed during the former phase is smaller than those formed in the latter phase. This is demonstrated in the attached figure. The time evolution of interfacial positions of 2 dense sprays for 2 different pressure pulses introduced at the nozzle inlet are delineated in this figure.

I visited Dr. W. Bryzik of TACOM on 21 September 1992. The visit made me aware of a fundamental problem in atomization which is even more basic than the intermittency of sprays.

